UNIVERSITY OF OTTAWA

Investigations of Partial Gas Saturation on Diffusion in Low-permeability Sedimentary Rocks

By

Jacob Nunn

A THESIS SUBMITTED TO THE FACULTY OF GRADUATE STUDIES IN PARTIAL FULFILLMENT OF THE REQUIREMENTS FOR THE DEGREE OF MASTER OF SCIENCE

DEPARTMENT OF EARTH AND ENVIRONMENTAL SCIENCES

OTTAWA, ONTARIO

August 2018

Abstract

The effect of partially saturated conditions on aqueous diffusion was investigated on the Upper Ordovician Queenston Formation shale from the Michigan Basin of southwest Ontario, Canada. Effective diffusion coefficients (D_e) were determined for iodide tracer on duplicate cm-scale samples from a core segment. Partially saturated conditions were created with a new gas-ingrowth method that takes advantage of the variability of N_2 solubility with pressure. The method is designed to create partially saturated pores, quantify the level of partial gas/brine saturation within the tracer-accessible pore space, and measure D_e under fully porewater-saturated and partially gas-saturated conditions for the same sample. X-ray radiography is used with an iodide tracer for quantifying the degree of partial saturation and measuring D_e. The saturated D_e values range from 2.8×10^{-12} to 3.1×10^{-12} m^2/s. Following generation of a gas phase in the pores (average gas saturations of 4 to 6.7 %), D_e values decrease by 20 to 22 % relative to the porewater-saturated condition, indicating that the tortuosity factor (ratio of constrictivity to tortuosity) is sensitive to saturation. Suggesting that a small volume of the pore fraction is responsible for majority of the transport. The gas-ingrowth method was successful for generating partial gas saturation, but the distribution of the gas phase is non-uniform, with relatively high gas saturations near boundaries and lower saturations in the interior of the samples.

Résumé

L'effet de conditions partiellement saturées sur la diffusion aqueuse a été étudié sur les schistes argileux de la formation de Queenston de l'Ordovicien supérieur dans le bassin du Michigan,

situé dans le sud-ouest de l'Ontario, au Canada. Les coefficients de diffusion effectifs (D_e) ont été déterminés pour un traceur d'iodure sur des échantillons dupliqués d'un segment de base, à l'échelle du centimètre. Des conditions partiellement saturées ont été créées avec une nouvelle méthode de pénétration de gaz qui tire parti de la relation entre la solubilité de N_2 et la pression. La méthode est conçue pour créer des pores partiellement saturés, quantifier le niveau de saturation partielle en gaz/saumure au sein des pores accessibles au traceur et mesurer le D_e dans des conditions saturées et partiellement saturées pour le même échantillon. La radiographie par rayons X est utilisée avec un traceur d'iodure pour quantifier le degré de saturation partielle et mesurer le D_e. Les valeurs du D_e en conditions saturées se situe entre 2.8×10^{-12} et 3.1×10^{-12} m^2 / s. Après la génération d'une phase gazeuse dans les pores (saturations moyennes en gaz de 4 à 6.7%), les valeurs de D_e diminuent de 20 à 22% par rapport à l'état saturé en eau interstitielle, indiquant que le facteur de tortuosité (rapport entre le pouvoir de constriction et la tortuosité) est sensible au niveau de saturation. Ceci suggère qu'une petite fraction des pores est responsable de la majorité du transport. La méthode de pénétration de gaz a réussi à générer une saturation partielle en gaz, mais la distribution de la phase gazeuse est non uniforme, avec des saturations en gaz relativement élevées près des surfaces de l’échantillon et des saturations en gaz inférieures à l'intérieur de ce dernier.

Acknowledgements

My time at the University of Ottawa has marked significant scientific, professional and personal growth in my life. I am grateful to have had the opportunity to meet and learn from many incredible people who have generously given their time, knowledge, support and enthusiasm.

Foremost, I would like to thank my supervisor Tom Al, who throughout this thesis has been patience, knowledgeable, curious and positive. He has pushed my own scientific curiosity and has been supportive and invaluable throughout this proccess. Thank you for helping me gain the knowledge and confidence needed to grow and achieve my scientific and professional goals.

I am grateful to Mark Jenson and Laura Kennell from the NWMO for their support and advice throughout the development of this project.

This project would not have been possible without the many members of the uOttawa staff that helped with various aspects including Monica Wilk-Alemany, Glen Poirier, Alain Mauviel, Gilles St-Jean and Norm St-Jean.

Thank you to Hervé Beaudoin and Benoit Raymond of the UOttawa machine shop whose expertise was invaluable to the project.

I would like to thank Dr. Fred Gaidies and Yannick Morneau from the University of Carleton for helping acquire X-ray images in the early aspects of the project. I would also like to thank Rich Amos from Carleton for generously allowing us to use his lab during this process.

Thank you to Murray Gringas from the University of Edmonton who generously helped acquire some of the samples used in this project.

Thank you, members of Tom's research group, all of you have contributed in some way to both the project and my professional growth. I would specifically like to thank Emilia, Magda, Duane, Jiujang and Sam; this project would not have been possible without your encouragement, knowledge, motivation and enthusiasm.

I am very thankful to my fellow graduate students. Your friendship, energy and support has made my time at UOttawa some of the best years of my life. I wish you all the very best.

Thank you to my parents, Andrew and Kelly, as well as my brother Zachary for your endless encouragement and support along this journey.

Finally, thank you Anne for joining me on this adventure, I can't image having gone through this without you. I cannot wait to embark on another journey.

Contents

List of Figures

Chapter 1

Chapter 2

Chapter 3

List of Tables

Chapter 1

Chapter 2

Chapter 3

Appendix A

Appendix B

Appendix C

Chapter 1: Introduction

This thesis reflects the work conducted to measure diffusion coefficients in low-permeability rocks that are partially saturated - containing a porewater and a gas phase in the pore space. The measurements were conducted with X-ray imaging techniques using a new X-ray CT instrument. Before the diffusion coefficient measurements could proceed, it was necessary to learn and document the limitations of the instrument and optimize instrumental parameters for the imaging project. Chapters one to four cover the background, methods, results, discussion and conclusions related to the development of a new method for measuring diffusion coefficients in partially saturated rocks. Appendices A to E contain details of the instrument optimization, data processing and systematics of X-ray interactions with rocks materials. Finally, this research has been accepted for publication in the peer-reviewed journal Applied Geochemistry and the final manuscript is included in Appendix F.

1.1 Solute Diffusion

Low-permeability sedimentary rocks are of scientific interest because they present barriers to the migration of fluids and contaminants, which is important in CO_2 sequestration, shale gas exploitation, and nuclear waste management (Al et al., 2015; Benson and Cole, 2008; Javadpour et al., 2007; Leung et al., 2014; Lindeberg and Bergmo, 2003; Mazurek et al., 2011; Russel and Gale, 1982). Diffusion is the dominant transport process in sedimentary formations when hydraulic conductivity (K) is less than about 10^{-10} m/s. The role of diffusive transport and its effect on barrier performance requires reliable measurements of effective diffusion coefficients (D_e) (Shackelford, 1991). Measurements of D_e have been conducted at the laboratory scale (cm) with several established techniques, including: through diffusion (Jacops et al., 2013; Rebour, 1997; Savoye et al., 2010; Van Loon et al., 2003; Xiang et al., 2016), in-diffusion (Cormenzana and Garcı., 2003), out-diffusion (Waber and Smellie, 2008), radial

diffusion (Van der Kamp and Van Stempvoort, 1996; Van Loon et al., 2004), X-ray computed tomography (CT) (Agbogun et al., 2013a,b), and radiography (Cavé et al., 2009; Loomer et al., 2013; Tidwell et al., 2000; Xiang et al., 2013). Drilling and sample collection for laboratory-scale measurements may cause thermo-mechanical disruption of cores, resulting in altered physical properties such as porosity and tortuosity. Attempts have been made to reproduce in-situ temperature and pressure conditions in the laboratory in order to determine the magnitude of these effects on diffusive transport (Savoye et al., 2011; Van Loon et al., 2004; Van Loon et al., 2003; Wise and Houghton., 1966; Xiang et al., 2016). In efforts to understand diffusive transport at a larger scale (10's to 100's of m), numerous researchers have employed measurements of naturally-occurring tracer distributions in rock porewater which, combined with solute-transport modelling and knowledge of paleohydrology, allows for estimation of D_e at the formation scale (Bensenouci et al., 2011; Desaulniers et al., 1981; Gimmi et al., 2007; Hendry et al., 2004; Hendry et al., 2013; Hendry and Harrington, 2014; Mazurek et al., 2011; Patriarche et al., 2004a, 2004b; Remenda et al., 1994).

The majority of laboratory-scale investigations have been conducted on fully saturated samples, but under in-situ conditions, partial saturation is expected in some circumstances. Examples include organic-rich sedimentary rocks that contain $CH_{4(g)}$ at concentrations in excess of solubility, resulting in exsolution and displacement of porewater, as well as tunnelling excavations, which can lead to partially saturated conditions in the Excavation Damaged Zone (EDZ) (Matray et al., 2007; Nagra, 2008). Investigations by Savoye et al. (2010, 2012, 2014) provide the most comprehensive assessment of the effect of partial saturation on solute diffusion in clay-rich rocks. They measured D_e for various tracers in the Callovo-Oxfordian

claystone under partially saturated conditions using the through diffusion method and demonstrated that partial gas saturation leads to a decrease in D_e for solutes in the aqueous phase. For iodide, the tracer which is the subject of the present study, they observed a decrease in the effective diffusion coefficient of Iodide (D_{e_I}) by a factor of 50 under conditions of 19% gas saturation. Additional examples of diffusion studies on partially saturated geologic materials include Badv and Faridfard (2005) Conca and Wright (1992), Hamamoto et al. (2009), Hamamoto et al. (2010) Mehta et al. (1995), Olesen et al. (2000), Porter et al. (1960) and Rowell et al. (1967).

Due to the time-consuming approaches to measuring the diffusion coefficients of solutes in unsaturated media, empirical models are often used to predict diffusion coefficients from physical characteristics of the geologic media. There have been many models proposed to describe diffusion in unsaturated media including Millington (1959), Sadeghi et al., (1989), Mehta et al., (1995) Olesen et al., (1996) with the two most widely used models being the Millington and Quirk Model proposed by Millington and Quirk. (1961) that was initially developed for gas diffusion, and the power-law diffusion dependence on saturation in the form of Archie's law (Archie, 1942).

The Upper Ordovician shales (Queenston, Georgian Bay and Blue Mountain formations) of the Michigan Basin in southwest Ontario, Canada, have been studied extensively at the Bruce Nuclear Site, where the 200-m thick low-permeability shale sequence has the necessary properties to act as natural geologic barrier for a proposed Deep Geological Repository (DGR) for low- and intermediate-level radioactive waste (Fig. 1.1) (CEAA, 2015).

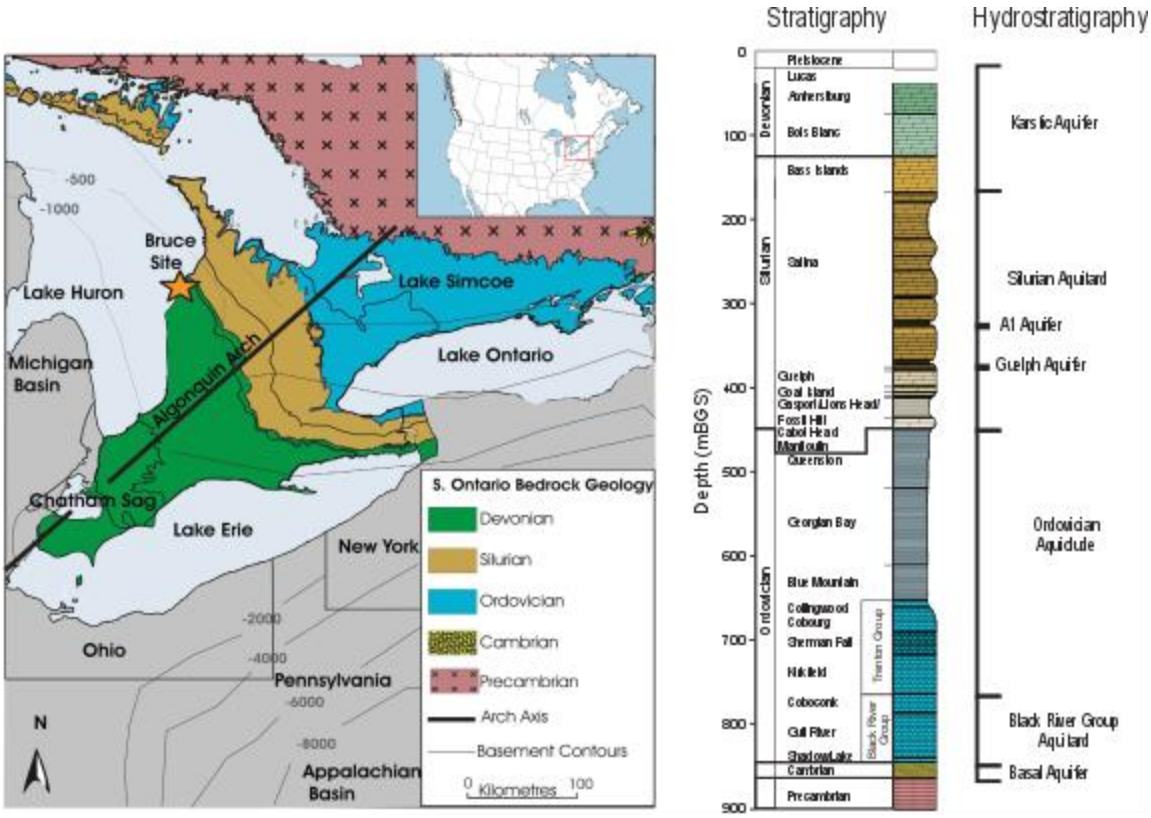

Fig. 1. 1 *Map showing the location of the Bruce Nuclear Site and stratigraphic column showing Queenston Formation (Al et al., 2015).*

Elevated $CH_{4(g)}$ concentrations have been measured in these shales (Clark et al., 2013), and it has been suggested that a gas phase of up to 10% may be present (Intera, 2011). The porewater in the shales has very high salinity, up to halite saturation (Al et al., 2015), and dewatering methods, such as that employed by Savoye et al. (2010, 2012, 2014), would lead to salt precipitation that could occlude pores and influence D_e.

1.2 Research Objectives

The objectives of this research are:

1) Develop a novel gas-ingrowth method for generation of a gas phase by manipulating pressure to control $N_{2(g)}$ solubility,

2) Improve signal-to-noise ratio (SNR) of the radiography technique (Cavé et al., 2009) to allow for measurement of the degree of gas saturation in the pore space, and
3) Quantify the change in D_e for I^- that results from the generation of partial gas saturation in samples of shale from the Michigan Basin.

1.3 Background

1.3.1 Diffusive solute transport

Diffusive solute transport occurs in the interconnected pores and microfractures of rocks in response to gradients in solute concentration. Throughout this process solutes may interact with minerals in rocks and can be retained in the rocks by a variety of processes including sorption, ion exchange and precipitation. Diffusion of a conservative solute can be described by Fick's laws, as reviewed by Crank (1975). Fick's first law relates the diffusive mass flux (J) of a solute (mol/m^2/s) in the direction i, to the solute concentration gradient under steady state conditions:

$$J_I = -D\frac{\Delta C}{\Delta x_i} \quad [1.1]$$

where: D(m^2/s) is the diffusion coefficient, C is the solute concentration (mol/m^3) and x is the spatial dimension in the direction of diffusion. Diffusion under transient conditions (t = time) is described by Fick's second law:

$$\frac{\Delta C}{\Delta t} = D\frac{\Delta^2 C}{\Delta x^2} \quad [1.2]$$

In a porous medium, diffusion of a solute will be slower when compared to diffusion in pure water due to the tortuosity (τ) and constrictivity (δ), which are properties of the porous

medium (Van Brakel and Heertjes, 1974). The pore diffusion coefficient (D_p) for a porous medium can be described in terms of the free-water diffusion coefficient (D_0), τ and δ:

$$D_p = D_0 * \frac{\delta}{\tau} \quad [1.3]$$

The τ is a geometric parameter that accounts for pore geometry which is defined as: $(l_e/l)^2$ where l_e is the effective (actual path) while l is the shortest possible transport distance (Van Brakel and Herrtjes., 1974) The δ is also a geometric parameter that only becomes important if the solute size is comparable to pore-throat sizes in the porous medium (Grathwohl, 1997). It is common to combine τ and δ into the tortuosity factor (τ_f):

$$D_p = D_0 * \tau_f \quad [1.4]$$

In the non-conservative case where a solute reacts with the porous media, another formulation of the diffusion coefficient known as the apparent diffusion coefficient (D_a) is used.

$$D_a = D_p * R_f \quad [1.5]$$

Where the decrease in mass flux due to reaction is taken into account by the retardation factor (R_f):

$$R_f = 1 + \left(\frac{\rho}{\theta}\right) * K_d \quad [1.6]$$

Where ρ is the bulk density, θ is the volumetric water content and K_d is the partition coefficient. In porous media, the presence of the solid phase (minerals) leads to a decrease in the cross-sectional area available for diffusion and this is accounted for with the use of the effective diffusion coefficient (D_e) term which includes a porosity term (ϕ):

$$D_e = \phi * D_p \quad [1.7]$$

1.3.2 X-ray radiography and Computed Tomography

1.3.2.2 Basic principles of X-ray radiography and computed topography

X-ray radiography imaging involves an X-ray source that generates X-rays which are directed toward an object where they are attenuated as they pass through, emerging X-ray intensities are measured and recorded at the detector as 2-D radiographs (Fig. 1.2). The attenuation properties of the imaged object (e.g. a rock sample) are a function of the physical and electron density, the chemical composition, and the photon path length through the object.

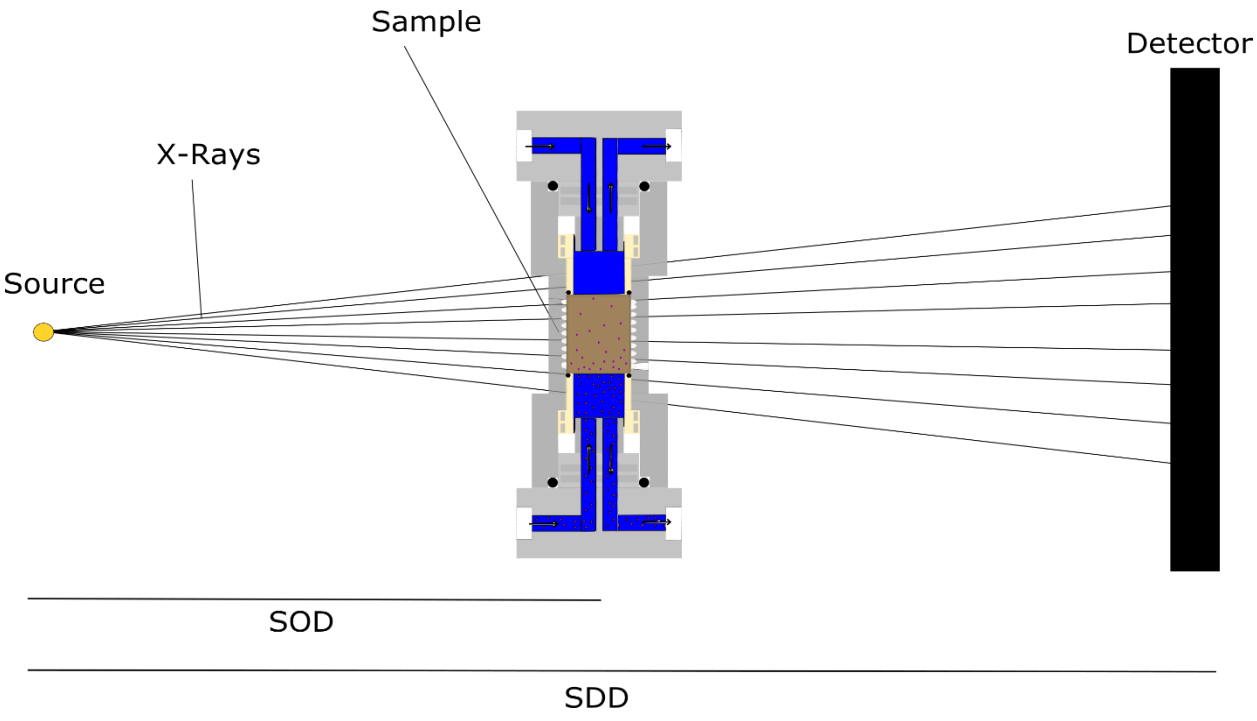

Fig. 1. 2 *X-ray radiography schematic diagram, showing source to object distance (SOD) and source to detector distance (SDD).*

Moving from radiography to Computed Tomography (CT) requires a rotational motion of the sample relative to the source-detector system in which 2-D radiographs can be recorded for

every step of rotation of a sample and are reconstructed into 3-D attenuation coefficient data sets with use of a computer algorithm (e.g. Feldkamp et al., 1984).

1.3.2.3 X-ray Source

X-ray generation involves bombarding a specific target material such as tungsten with accelerated electrons in a vacuum tube. This emits X-rays when incident electrons lose energy after collision with the electron cloud of the target (Nakasshimi, 2000; Wildenschild et al., 2002). The source focal-spot size, peak accelerating voltage and the intensity of X-rays can be adjusted for optimization with regard to a specific imaging problem. Generally, the focal spot size and magnification affect the resolution of an image. The focal spot size dictates the number of possible source-detector paths, the higher the number of paths the larger the blur on the image, this is often referred to as a Penumbra (Fig. 1.3).

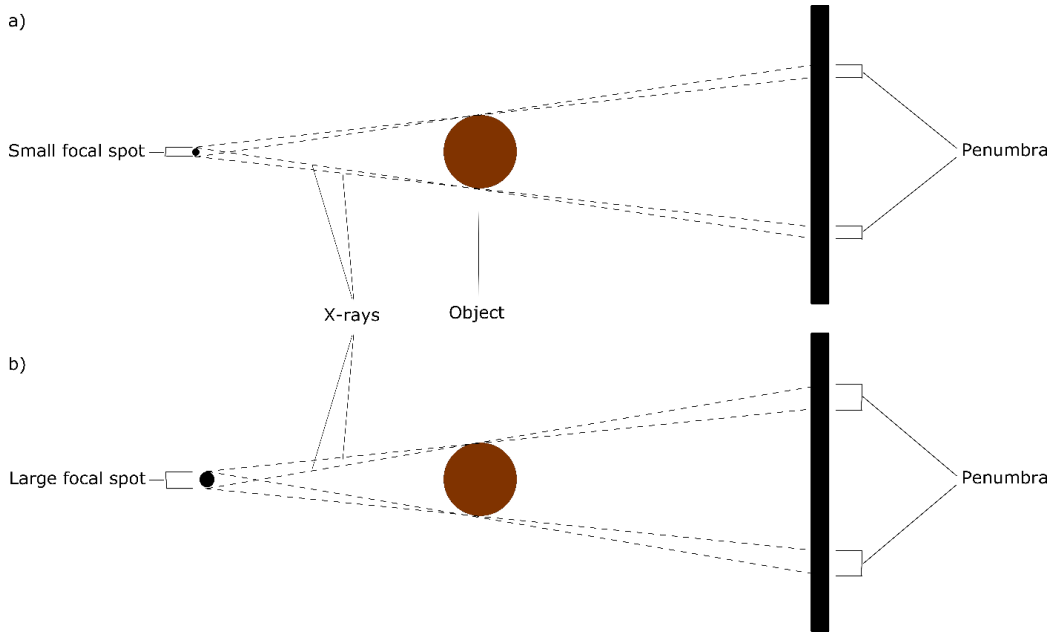

Fig. 1. 3 *Showing the difference in Penumbra's between a) small focal spot and b) large focal spot. The smaller focal spot has less possible source to detector paths creating a smaller penumbra effect therefore allowing for higher resolution images.*

The magnification, *M,* can be calculated by the source to detector and source to object positioning with the following equation:

$$M = \frac{SDD}{SOD} \quad [1.8]$$

Where *SDD* is the source to detector distance and SOD is the source to object distance (Fig.1.2).

A typical X-ray source produces a polychromatic X-ray emission spectrum that emits a range of X-ray energies. The energy spectrum is usually described in terms of the peak X-ray energy (keV or MeV) but actually consists of a continuum with the maximum intensity typically occurring at less than half of the peak energy (Fig.1.4). The peak energy is determined by the accelerating voltage that is applied at the source; an accelerating voltage of X kV will generate a source spectrum with a continuum of photon energies from 0 to X keV. Lower X-ray energies (below 10 keV) are generally considered soft X-rays and are sensitive to chemical composition and readily absorbed by materials, while higher X-ray energies (above 10 keV) are generally considered hard X-rays and are sensitive to chemical composition but can have higher penetration abilities, therefore highly attenuating samples may require sources with high X-ray energies while compositional imaging requires lower X-ray energies. Generally the process works as a continuum with lower energy X-rays being more readily absorbed than those at higher energies.

X-ray intensity, or flux, is controlled by the current setting at the source and increased current can be used to improve counting statistics, resulting in better signal to noise ratio.

However, high current/X-ray intensity causes heating of the source target, leading to the requirement for increased focal spot size and consequent decrease in image resolution.

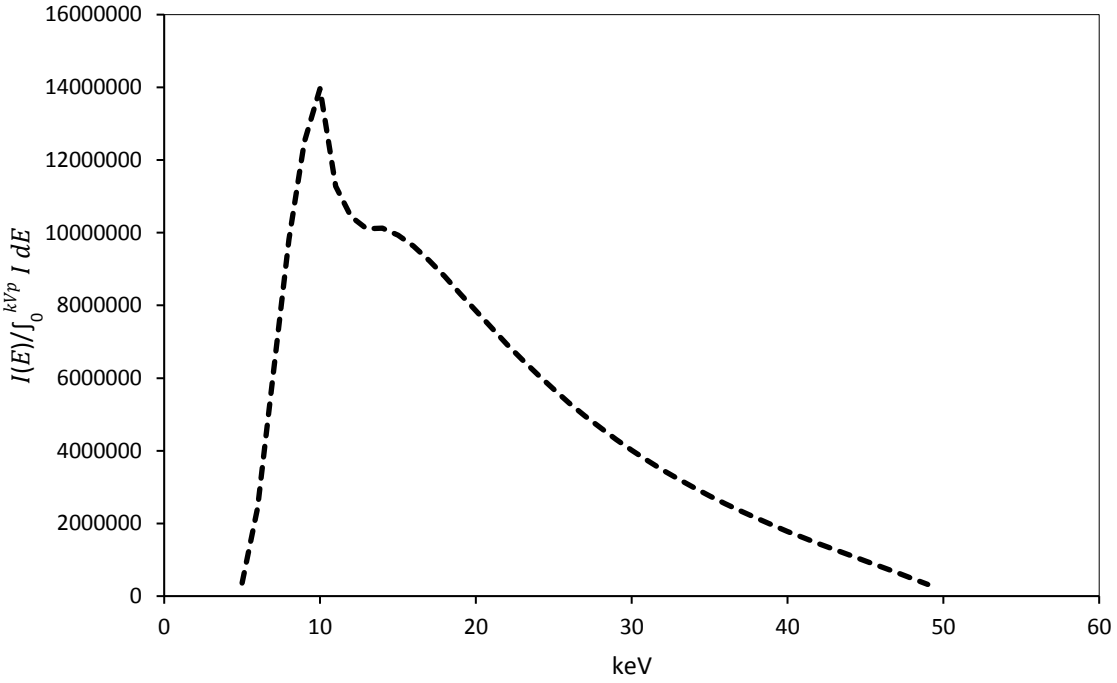

Fig. 1. 4 *Calculated emission spectrum for a tungsten X-ray source with a 50 keV peak energy and 750 mm SDD. Figure shows a peak energy at 50 keV while the bulk of the X-ray energies occur from 10-20 keV. Calculations were conducted with SpekCalc (Poludniowski et al., 2009).*

1.3.2.4 X-ray Attenuation

As X-rays pass through an object, they are attenuated by scattering and absorption. The basic equation for attenuation of a monoenergetic beam through a homogeneous material is Beer's Law:

$$I = I_0 exp[-\mu x] \quad [1.9]$$

Where I_0 is the initial X-ray intensity, μ is the linear attenuation coefficient of the material being scanned and x is the length of the X-ray path through the material. If the scanned object is composed of a number of different materials, the equation becomes:

$$I = I_0 exp[-\sum_i(\mu_i x_i)] \quad [1.10]$$

Where each increment *i* reflects a single material with attenuation coefficient μ_i over a linear extent x_i. As X-ray sources are polychromatic, and attenuation coefficients vary with X-ray energy, the comprehensive solution requires solving the equation over the energy range of the X-ray spectrum:

$$I = \int I_0\,(E)\; exp[-\sum_i(\mu_i(E)x_i)]dE \quad [1.11]$$

The variability of the X-ray spectrum from a polychromatic source complicates efforts to calculate attenuation and that has led to the use of monochromators. However, monochromators can dramatically reduce the beam intensity, so their use is commonly limited to high-intensity sources such as at synchrotron facilities.

The process of X-ray attenuation consists of three mechanisms; the photoelectric effect, Compton scattering and pair production. The photoelectric effect is the process of X-ray absorption when the total energy of an incident X-ray photon is transferred to an inner-shell electron of the atom, resulting in the ejection of the electron. This is the dominant interaction process with X-ray energies that, in general, are less than 100 keV (Hussein, 2010). Considering X-ray absorption by any specific element, with increasing photon energy there is an abrupt increase in photoelectric X-ray absorption at the energy corresponding to the binding energy of the K (innermost) shell electrons. Therefore, in rocks dominated by O, Si, Al, Fe, Ca, Na and K, the photoelectric effect will dominate at < 10 to 20 keV.

Compton scattering increases in significance with increasing X-ray energy, generally between 50 keV - 1.5 MeV. It results from a photon ejecting an electron, causing it to lose

energy and subsequently being deflected in different direction (Hussein, 2010). Pair production becomes significant at high energy, > 1 MeV, and occurs when an incident X-ray photon interacts with a neutron which then transforms into a positron-electron pair which absorbs the photon energy, transferring it into kinetic energy of the pair (Hussein, 2010).

1.3.2.5 Detector

There is a great variety of flat panel detectors available for capturing 2-D radiographs. They are made up of thousands of sensors that record the data represented by corresponding pixels in an image. The flat panel detector on the Pinnacle X-ray system at uOttawa (Varian 1313DX) is made with a CsI scintillating layer material coupled to a segmented (pixels) light-sensitive amorphous silicon layer that converts light generated by scintillations in the CsI to spatially resolved electrical signals used to generate the image. The detector can vary the exposure time required to acquire an image which is an important control on X-ray intensity. The pixel pitch (size) can affect the resolution of the image, but the source focal spot size and the magnification are also important controls on resolution.

1.3.2.6 Quantitative Analysis using a polychromatic source in geoscience

There have been many advancements in quantitative applications of X-ray radiography and CT in geosciences, such as measuring porosity of rocks (Withjack, 1988; Tidwell et al., 2000; Cave et al., 2009; Agbogun et al., 2013a,b; Loomer et al., 2013; Xiang et al., 2013), X-ray CT has been employed for pore scale imaging (Arns et al., 2005; Wildenschild and Sheppard., 2013; Blunt et al., 2014) and to characterize phase distributions (Tidwell and glass., 1994; Van Geet et al., 2001; Wildenschild et al., 2002; Cislerova and Votrubova., 2002; Katuwal et al., 2015; Paradelo et al., 2016). While other X-ray radiography and CT techniques have been developed to quantify transport properties of rocks including permeability and hydraulic conductivity

(Withjack et al., 1991; Paradelo et al., 2016) and tracer diffusion (Altman et al., 2004; Zhelezny and Shapiro., 2006; Cave et al., 2009; Xiang et al., 2013; Loomer et al., 2013; Agbogun et al., 2013a,b).

1.3.2.7 Limitations of X-ray computed tomography and radiography using a polychromatic system.

Limitations of X-ray CT derive from poor signal to noise ratio (SNR). The ability to distinguish features of interest from the background in an image is commonly assessed using the SNR. In the case of imaging with a tracer, it is the increased attenuation by the tracer that increases absolute contrast (the signal) and thereby enhances the SNR. Absolute contrast SNR can be described by:

$$SNR = \frac{\Delta I}{\sigma} \qquad [1.12]$$

ΔI is the change in intensity caused by a feature of interest, in the case of diffusion and porosity measurements a tracer, σ is the relative standard deviation on repeat measurements. Difference imaging (adding and subtracting images at different times) can be used to determine σ, taking into account source and detector (image) noise, misalignment and intensity variations (Fig. 1.5).

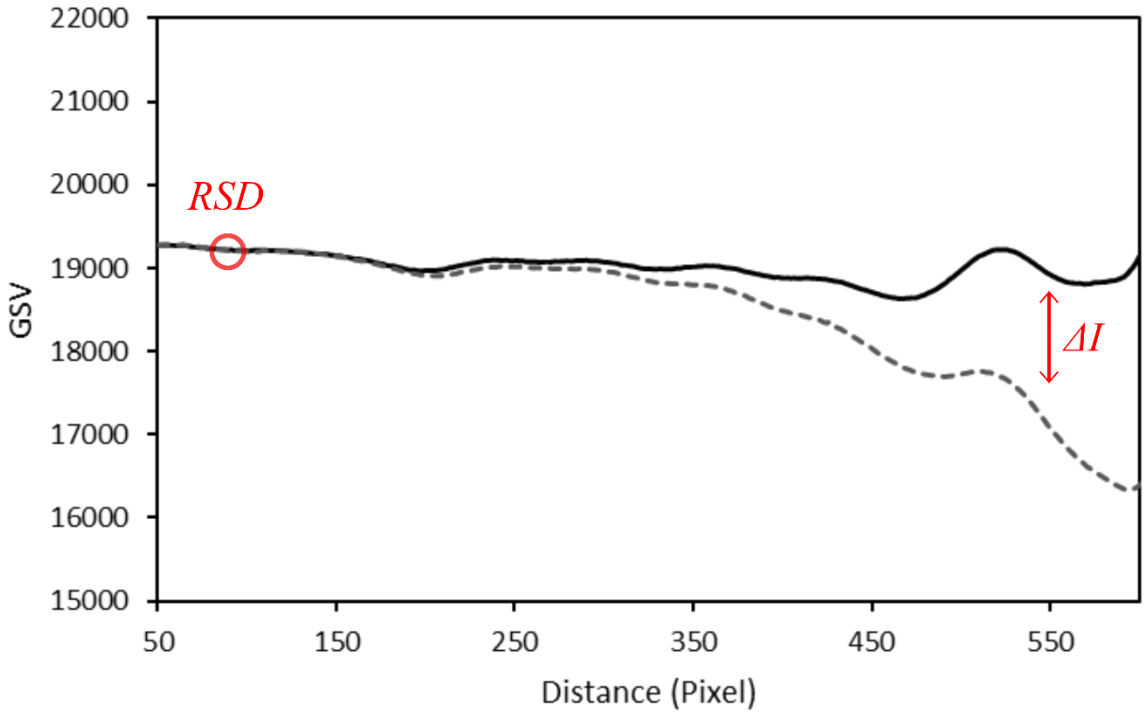

Fig. 1. 5 *Grey Scale Value profile using X-ray radiography and difference imaging of a sample showing an area displaying an absolute contrast SNR with 1 mol/kgw Iodide tracer and the unaffected area representing the RSD of the difference images (Equation 1.12).*

Image noise is random variation of brightness, and it manifests as random fluctuations in grey-scale values (GSV) recorded at pixels. The amount of image noise may be specific to a source/detector pair while additional noise can be related to photon saturation. X-ray intensity is an important control on image noise, low intensities at the detector can lead to a significant increase in image noise - this is known as the quantum mottle effect. The quantum mottle effect relates to the statistical distribution of photons around the detector, for simplicity the effect can be compared with a rain shower (Fig. 1.6). A light rain leaves the pavement spotted with water marks as the flux of water is not significant enough to provide an even distribution of rain, while a heavier rain shower provides an even distribution leaving the surface evenly wet (Fig. 1.6). It is therefore advantageous to maximize counts, but the upper limit is defined by the

X-ray detector, as detectors can be oversaturated with a photon flux, which over time can result in damage to the detector.

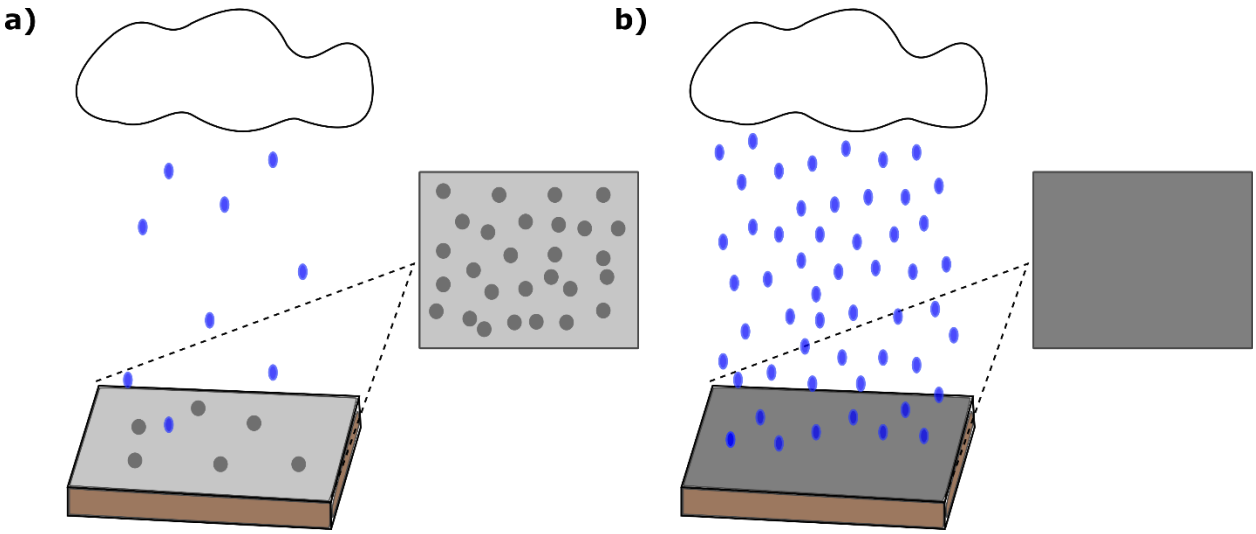

Fig. 1. 6 *Example to demonstrate the quantum mottle effect which results from low X-ray counts. Here the analogy is made with rain drop coverage on the ground surface for a) light rain and b) heavy rain.*

Use of an X-ray source spectrum in the range of photoelectric attenuation, < 100 keV, but ideally less than 50 or 60 keV, provides increased chemical contrast. This is ideal for chemical tracer detection, but low energy X-rays are strongly attenuated in the sample so high currents (source intensities) are required to achieve a satisfactory SNR.

Beam hardening results from preferential attenuation of the low energy region of a polychromatic X-ray spectrum as the beam passes through an object (Clausnitzer and Hopmans, 2000; Ketcham and Carlson, 2001; Roche et al., 2010). Lower energy X-rays are more readily attenuated than higher energy X-rays, resulting in preferential attenuation of the low-energy portion of the spectrum, or hardening, as a beam passes through an object. This causes artificial image contrast between the thinnest and thickest parts of a sample, or between the edge and

centre of a reconstructed CT image. This is an artifact that can be mistakenly interpreted as a variation in sample properties. Common mitigation techniques include: 1) the use of smaller sample sizes which results in shorter travel paths for incident X-rays, thereby minimizing loss of the low energy parts of the spectrum (Ketcham and Carlson., 2001); 2) prefiltering or hardening of the X-ray beam to remove lower energy X-rays; and 3) post-processing techniques in CT but this approach can distort quantitative data (Ketcham and Carlson., 2001). The best solution to eliminate beam hardening is to use a monochromatic X-ray source, but this is generally only possible with high-brightness X-ray sources such as those found at synchrotron facilities.

Partial volume effects can influence the measured attenuation coefficient at a pixel (radiography) or voxel (X-ray CT), as the volume depicts the average properties of materials within the area it represents (Fig. 1.7) (Ketcham and Carlson., 2001). This means that the GSV that reflects chemical and physical properties of a sample is an integrated measure of multiple materials that occur in the spatial region represented by a pixel or a voxel. In radiography this is assumed while in CT this can over-estimate or underestimate the properties of interest at discreet locations (Fig. 1.7). This problem can be addressed by using smaller pixel sizes to achieve higher resolution, or by adopting an REV approach using difference imaging (Tidwell et al.,2000; Cave et al., 2009; Agbogun et al., 2013a,b).

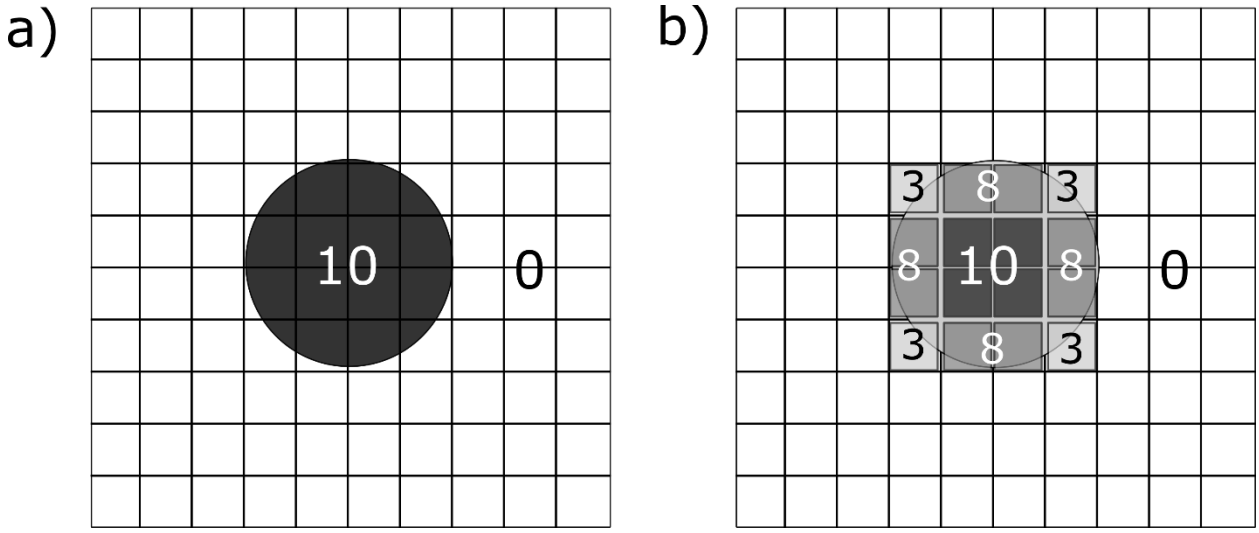

Fig. 1. 7 *a) Real signal intensity of a feature of interest b) Influence of partial volume effects on a feature of interest. Pixels on edges of the feature include both the feature and the background. Signal intensity in these pixels is the mean of the signal intensities of both the feature and the background. Figure modified from (Soret et al., 2007).*

Misalignment is a common problem during processing for difference imaging techniques and it results when there is stage and sample movement between corresponding images. The problem of misalignment is mitigated by careful sample placement, use of a micro positioning stage, use of alignment guides (Cave et al., 2009), and in the case of CT data, the use of registration software (Williamson, 2009; Agbogun et al., 2013a,b).

Instrumental source-intensity drift is another common problem for CT and difference imaging techniques. Instrumental drift can result in differences in intensity of the emission spectrum and detector sensitivity between images. Changes in the intensity of the spectrum can be caused by drift in a target heating within the source and fluctuations in the power grid during and between measurements, leading to errors during CT scans and difference images. Use of a standard can help account for instrumental drift by normalization (Cave et al., 2009; Agbogun et al., 2013a,b).

1.4 References

Agbogun, H.M.D., Al, T.A., Hussein, E.M.A., 2013a. Three dimensional imaging of porosity and tracer concentration distributions in a dolostone sample during diffusion experiments using X-ray micro-CT. J. Contam. Hydrol. 145, 44–53.

Agbogun, H.M.D., Hussein, E.M.A., Al, T.A., 2013b. Assessment of x-ray micro-CT measurements of porosity and solute concentration distributions during diffusion in porous geologic media. J. Porous Media 16, 683–694.

Al, T.A., Clark, I.D., Kennell, L., Jensen, M., Raven, K.G., 2015. Geochemical evolution and residence time of porewater in low-permeability rocks of the Michigan Basin, Southwest Ontario. Chem. Geol. 404, 1–17.

Altman, S.J., Uchida, M., Tidwell, V.C., Boney, C.M., Chambers, B.P., 2004. Use of X-ray absorption imaging to examine heterogeneous diffusion in fractured crystalline rocks. J. Contam. Hydrol. 69, 1–26. https://doi.org/10.1016/S0169-7722(03)00153-0

Altman, S.J., Uchida, M., Tidwell, V.C., Boney, C.M., Chambers, B.P., 2004. Use of X-ray absorption imaging to examine heterogeneous diffusion in fractured crystalline rocks. J. Contam. Hydrol. 69, 1–26.

Archie, G.E., others, 1942. The electrical resistivity log as an aid in determining some reservoir characteristics. Trans. AIME 146, 54–62.

Arns, C.H., Bauget, F., Limaye, A., Sakellariou, A., Senden, T., Sheppard, A., Sok, R.M., Pinczewski, V., Bakke, S., Berge, L.I., others, 2005. Pore scale characterization of carbonates using X-ray microtomography. Spe J. 10, 475–484.

Baba, R., Ueda, K., Okabe, M., 2004. Using a flat-panel detector in high resolution cone beam CT for dental imaging. Dentomaxillofacial Radiol. 33, 285–290.

Badv, K., Faridfard, M.R., 2005. Laboratory determination of water retention and diffusion coefficient in unsaturated sand. Water, Air, Soil Pollut. 161, 25–38.

Bensenouci, F., Michelot, J.L., Matray, J.M., Savoye, S., Lavielle, B., Thomas, B., Dick, P., 2011. A profile of helium-4 concentration in pore-water for assessing the transport phenomena through an argillaceous formation (Tournemire, France). Phys. Chem. Earth, Parts A/B/C 36, 1521–1530.

Benson, S.M., Cole, D.R., 2008. CO 2 sequestration in deep sedimentary formations. Elements 4, 325–331.

Blunt, M.J., Bijeljic, B., Dong, H., Gharbi, O., Iglauer, S., Mostaghimi, P., Paluszny, A., Pentland, C., 2013. Pore-scale imaging and modelling. Adv. Water Resour. 51, 197–216.

C\íslerová, M., Votrubová, J., 2002. CT derived porosity distribution and flow domains. J. Hydrol. 267, 186–200.

Cavé, L., Al, T., Xiang, Y., Vilks, P., 2009. A technique for estimating one-dimensional diffusion coefficients in low-permeability sedimentary rock using X-ray radiography: comparison with through-diffusion measurements. J. Contam. Hydrol. 103, 1–12.

CEAA, 2015. Joint Review Panel Environmental Assessment Report: Deep Geologic Repository for Low to Intermediate Level Radioactive Waste Project. CEAA Reference No. 17520. Ottawa, Canada. Report available online through https://www.ceaa-acee.gc.ca.

Clark, I.D., Al, T., Jensen, M., Kennell, L., Mazurek, M., Mohapatra, R., Raven, K.G., 2013. Paleozoic-aged brine and authigenic helium preserved in an Ordovician shale aquiclude. Geology 41, 951–954.

Clausnitzer, V., Hopmans, J.W., 2000. Pore-scale measurements of solute breakthrough using microfocus X-ray computed tomography. Water Resour. Res. 36, 2067–2079.

Cnudde, V., Boone, M.N., 2013. High-resolution X-ray computed tomography in geosciences: A review of the current technology and applications. Earth-Science Rev. 123, 1–17.

Conca, J.L., Wright, J., 1992. Diffusion and flow in gravel, soil, and whole rock. Hydrogeol. J. 1, 5–24.

Cormack, A.M., 1963. Representation of a function by its line integrals, with some radiological applications. J. Appl. Phys. 34, 2722–2727.

Cormenzana, J.L., Garc\ía-Gutiérrez, M., Missana, T., Junghanns, Á., 2003. Simultaneous estimation of effective and apparent diffusion coefficients in compacted bentonite. J. Contam. Hydrol. 61, 63–72.

Crank, J., 1979. The mathematics of diffusion. Oxford university press.

Der Kamp, G., Van Stempvoort, D.R., Wassenaar, L.I., 1996. Using intact cores to determine isotopic composition, chemistry and effective porosities for groundwater in aquitards. Water Resour. Res 32, 1815–1822.

Desaulniers, D.E., Cherry, J.A., Fritz, P., 1981. Origin, age and movement of pore water in argillaceous Quaternary deposits at four sites in southwestern Ontario. J. Hydrol. 50, 231–257.

Feldkamp, L.A., Davis, L.C., Kress, J.W., 1984. Practical cone-beam algorithm. JOSA A 1, 612–619.

Hamamoto, S., Moldrup, P., Kawamoto, K., Komatsu, T., 2010. Excluded-volume expansion of Archie's law for gas and solute diffusivities and electrical and thermal conductivities in variably saturated porous media. Water Resour. Res. 46.

Hamamoto, S., Perera, M.S.A., Resurreccion, A., Kawamoto, K., Hasegawa, S., Komatsu, T., Moldrup, P., 2009. The solute diffusion coefficient in variably compacted, unsaturated volcanic ash soils. Vadose Zo. J. 8, 942–952.

Hendry, M.J., Barbour, S.L., Novakowski, K., Wassenaar, L.I., 2013. Paleohydrogeology of the Cretaceous sediments of the Williston Basin using stable isotopes of water. Water Resour. Res. 49, 4580–4592.

Hendry, M.J., Harrington, G.A., 2014. Comparing vertical profiles of natural tracers in the Williston Basin to estimate the onset of deep aquifer activation. Water Resour. Res. 50, 6496–6506.

Hendry, M.J., Kelln, C.J., Wassenaar, L.I., Shaw, J., 2004. Characterizing the hydrogeology of a complex clay-rich aquitard system using detailed vertical profiles of the stable isotopes of water. J. Hydrol. 293, 47–56.

Hicks Jr, P.J., Narayanan, R., Deans, H.A., others, 1994. An experimental study of miscible displacements in heterogeneous carbonate cores using X-ray CT. SPE Form. Eval. 9, 55–60.

Hounsfield, G.N., 1973. Computerized transverse axial scanning (tomography): Part 1. Description of system. Br. J. Radiol. 46, 1016–1022.

Hussein, E.M.A., 2010. Radiation mechanics: Principles and practice. Elsevier.

Intera, 2011. Descriptive geosphere site model, Revision 0. DGR-TR-2011-24. Intera Engineering Ltd. Report prepared for the Nuclear Waste Management Organization NWMO. Report available online through http://www.nwmo.ca.

Jacops, E., Volckaert, G., Maes, N., Weetjens, E., Govaerts, J., 2013. Determination of gas diffusion coefficients in saturated porous media: He and CH 4 diffusion in Boom Clay. Appl. Clay Sci. 83, 217–223.

Javadpour, F., Fisher, D., Unsworth, M., others, 2007. Nanoscale gas flow in shale gas sediments. J. Can. Pet. Technol. 46.

Katuwal, S., Moldrup, P., Lamandé, M., Tuller, M., De Jonge, L.W., 2015. Effects of CT number derived matrix density on preferential flow and transport in a macroporous agricultural soil. Vadose Zo. J. 14.

Ketcham, R.A., Carlson, W.D., 2001. Acquisition, optimization and interpretation of X-ray computed tomographic imagery: applications to the geosciences. Comput. Geosci. 27, 381–400.

Leung, D.Y.C., Caramanna, G., Maroto-Valer, M.M., 2014. An overview of current status of carbon dioxide capture and storage technologies. Renew. Sustain. Energy Rev. 39, 426–443.

Lindeberg, E., Bergmo, P., 2003. The long-term fate of CO2 injected into an aquifer. Greenh. gas Control Technol. 1, 489–494.

Loomer, D.B., Scott, L., Al, T.A., Mayer, K.U., Bea, S., 2013. Diffusion--reaction studies in low permeability shale using X-ray radiography with cesium. Appl. geochemistry 39, 49–58.

Matray, J.M., Savoye, S., Cabrera, J., 2007. Desaturation and structure relationships around drifts excavated in the well-compacted Tournemire's argillite (Aveyron, France). Eng. Geol. 90, 1–16.

Mazurek, M., Alt-Epping, P., Bath, A., Gimmi, T., Waber, H.N., Buschaert, S., De Cannière, P., De Craen, M., Gautschi, A., Savoye, S., others, 2011. Natural tracer profiles across argillaceous formations. Appl. Geochemistry 26, 1035–1064.

Mehta, B.K., Shiozawa, S., Nakano, M., 1995. MEASUREMENT OF MOLECULAR DIFFUSION OF SALT IN UNSATURATED SOILS. Soil Sci. 159, 115–121.

Millington, R.J., 1959. Gas diffusion in porous media. Science (80-.). 130, 100–102.

Millington, R.J., Quirk, J.P., 1961. Permeability of porous solids. Trans. Faraday Soc. 57, 1200–1207.

Nagra, 2008. Effects of Post-disposal Gas Generation in a Repository for Low- and Intermediate-level Waste Sited in the Opalinus Clay of Northern Switzerland. Nagra Technical Report NTB 08-07. Wettingen, Switzerland.

Nakashima, Y., 2000. The use of X-ray CT to measure diffusion coefficients of heavy ions in water-saturated porous media. Eng. Geol. 56, 11–17.

Olesen, T., Moldrup, P., Henriksen, K., Petersen, L.W., 1996. Modeling diffusion and reaction in soils: IV. New models for predicting ion diffusivity. Soil Sci. 161, 633–645.

Olesen, T., Moldrup, P., Yamaguchi, T., Nissen, H.H., Rolston, D.E., 2000. Modified half-cell method for measuring the solute diffusion coefficient in undisturbed, unsaturated soil. Soil Sci. 165, 835–840.

Paradelo, M., Katuwal, S., Moldrup, P., Norgaard, T., Herath, L., de Jonge, L.W., 2016. X-ray CT-derived soil characteristics explain varying air, water, and solute transport properties across a loamy field. Vadose Zo. J. 15.

Patriarche, D., Ledoux, E., Michelot, J.-L., Simon-Coinçon, R., Savoye, S., 2004a. Diffusion as the main process for mass transport in very low water content argillites: 2. Fluid flow and mass transport modeling. Water Resour. Res. 40.

Patriarche, D., Michelot, J.-L., Ledoux, E., Savoye, S., 2004b. Diffusion as the main process for mass transport in very low water content argillites: 1. Chloride as a natural tracer for mass transport—Diffusion coefficient and concentration measurements in interstitial water. Water Resour. Res. 40.

Poludniowski, G., Landry, G., DeBlois, F., Evans, P.M., Verhaegen, F., 2009. SpekCalc: a program to calculate photon spectra from tungsten anode x-ray tubes. Phys. Med. Biol. 54, N433.

Porter, L.K., Kemper, W.D., Jackson, R.D., Stewart, B.A., 1960. Chloride diffusion in soils as influenced by moisture content. Soil Sci. Soc. Am. J. 24, 460–463.

Rebour, V., Billiotte, J., Deveughele, M., Jambon, A., Le Guen, C., 1997. Molecular diffusion in water-saturated rocks: A new experimental method. J. Contam. Hydrol. 28, 71–93.

Remenda, V.H., Cherry, J.A., Edwards, T.W.D., 1994. Isotopic composition of old ground water from Lake Agassiz: implications for late Pleistocene climate. Science (80-.). 266, 1975.

Roche, R.C., Abel, R.A., Johnson, K.G., Perry, C.T., 2010. Quantification of porosity in Acropora pulchra (Brook 1891) using X-ray micro-computed tomography techniques. J. Exp. Mar. Bio. Ecol. 396, 1–9.

Rowell, D.L., Martin, M.W., Nye, P.H., 1967. THE MEASUREMENT AND MECHANISM OF ION DIFFUSION IN SOILS III. THE EFFECT OF MOISTURE CONTENT AND SOIL-SOLUTION CONCENTRATION ON THE SELF-DIFFUSION OF IONS IN SOILS. Eur. J. Soil Sci. 18, 204–221.

Russell, D.J., Gale, J.E., 1982. Radioactive waste disposal in the sedimentary rocks of southern Ontario. Geosci. Canada 9.

Sadeghi, A.M., Kissel, D.E., Cabrera, M.L., 1989. Estimating molecular diffusion coefficients of urea in unsaturated soil. Soil Sci. Soc. Am. J. 53, 15–18.

Savoye, S., Beaucaire, C., Fayette, A., Herbette, M., Coelho, D., 2012. Mobility of cesium through the callovo-oxfordian claystones under partially saturated conditions. Environ. Sci. Technol. 46, 2633–2641.

Savoye, S., Goutelard, F., Beaucaire, C., Charles, Y., Fayette, A., Herbette, M., Larabi, Y., Coelho, D., 2011. Effect of temperature on the containment properties of argillaceous rocks: The case study of Callovo--Oxfordian claystones. J. Contam. Hydrol. 125, 102–112.

Savoye, S., Imbert, C., Fayette, A., Coelho, D., 2014. Experimental study on diffusion of tritiated water and anions under variable water-saturation and clay mineral content: comparison with the Callovo-Oxfordian claystones. Geol. Soc. London, Spec. Publ. 400, 579–588.

Savoye, S., Page, J., Puente, C., Imbert, C., Coelho, D., 2010. New experimental approach for studying diffusion through an intact and unsaturated medium: a case study with Callovo-Oxfordian argillite. Environ. Sci. Technol. 44, 3698–3704.

Shackelford, C.D., 1991. Laboratory diffusion testing for waste disposal—A review. J. Contam. Hydrol. 7, 177–217.

Soret, M., Bacharach, S.L., Buvat, I., 2007. Partial-volume effect in PET tumor imaging. J. Nucl. Med. 48, 932.

Tidwell, V.C., Glass, R.J., 1994. X ray and visible light transmission for laboratory measurement of two-dimensional saturation fields in thin-slab systems. Water Resour. Res. 30, 2873–2882.

Tidwell, V.C., Meigs, L.C., Christian-Frear, T., Boney, C.M., 2000. Effects of spatially heterogeneous porosity on matrix diffusion as investigated by X-ray absorption imaging. J. Contam. Hydrol. 42, 285–302.

Van Brakel, J., Heertjes, P.M., 1974. Analysis of diffusion in macroporous media in terms of a porosity, a tortuosity and a constrictivity factor. Int. J. Heat Mass Transf. 17, 1093–1103.

Van Geet, M., Swennen, R., 2001. Quantitative 3D-fracture analysis by means of microfocus X-Ray Computer Tomography (µCT): An example from coal. Geophys. Res. Lett. 28, 3333–3336.

Van Loon, L.R., Soler, J.M., Bradbury, M.H., 2003. Diffusion of HTO, 36 Cl- and 125 I- in Opalinus Clay samples from Mont Terri: effect of confining pressure. J. Contam. Hydrol. 61, 73–83.

Van Loon, L.R., Soler, J.M., Müller, W., Bradbury, M.H., 2004. Anisotropic diffusion in layered argillaceous rocks: a case study with Opalinus Clay. Environ. Sci. Technol. 38, 5721–5728.

Waber, H.N., Smellie, J.A.T., 2008. Characterisation of pore water in crystalline rocks. Appl. Geochemistry 23, 1834–1861.

Wildenschild, D., Sheppard, A.P., 2013. X-ray imaging and analysis techniques for quantifying pore-scale structure and processes in subsurface porous medium systems. Adv. Water Resour. 51, 217–246.

Wildenschild, D., Vaz, C.M.P., Rivers, M.L., Rikard, D., Christensen, B.S.B., 2002. Using X-ray computed tomography in hydrology: systems, resolutions, and limitations. J. Hydrol. 267, 285–297.

Williamson, M.D., 2009. An efficient algorithm for 3D image registration. M.Sc. thesis. Department of Computer Science. University of New Brunswick.

Wise, D.L., Houghton, G., 1966. The diffusion coefficients of ten slightly soluble gases in water at 10--60 C. Chem. Eng. Sci. 21, 999–1010.

Withjack, E.M., Orsham, S.K., Yang, C.T., others, 1991. CT determination of heterogeneities and miscible displacement characteristics. SPE Form. Eval. 6, 447–452.

Withjack, E.M., others, 1988. Computed tomography for rock-property determination and fluid-flow visualization. SPE Form. Eval. 3, 696–704.

Xiang, Y., Al, T., Mazurek, M., 2016. Effect of confining pressure on diffusion coefficients in clay-rich, low-permeability sedimentary rocks. J. Contam. Hydrol. 195, 1–10.

Xiang, Y., Al, T., Scott, L., Loomer, D., 2013. Diffusive anisotropy in low-permeability Ordovician sedimentary rocks from the Michigan Basin in southwest Ontario. J. Contam. Hydrol. 155, 31–45.

Zhelezny, P. V, Shapiro, A.A., 2006. Experimental investigation of the diffusion coefficients in porous media by application of x-ray computer tomography. J. Porous Media 9.

Chapter 2: Materials and Methods

2.1 Sample description

The samples used in this study are from the Ordovician Queenston Formation shale. The duplicate samples were collected from a 76-mm-diameter drill core segment at a depth of 472 m in borehole DGR-3 located at the Bruce nuclear site in southwest Ontario, Canada. Representative physical and mineralogical properties of the Queenston shale are provided in Table 2.1.

Table 2. 1 *Representative physical properties of the Queenston Formation shale, including porosity, diffusivity, hydraulic conductivity and mineralogy.*

Porosity, Diffusion and Hydraulic Conductivity				
Water-accessible porosity ϕ_w[a]	**Iodide-accessible porosity ϕ_I[a]**	**Effective-diffusion of HTO (perpendicular to bedding) $D_{e\text{-}HTO}$[a] m^2/s**	**Effective-Diffusion of Iodide (perpendicular to bedding) $D_{e\text{-}I}$[a] m^2/s**	**Hydraulic Conductivity K_h[b] m/s**
0.058 – 0.11	0.044 – 0.094	4.8×10^{-12}	1.20×10^{-12} – 3.4×10^{-12}	3.0×10^{-14}

Mineralogy (wt %)			
	DGR2[c]	**DGR3[d]**	**DGR4[d]**
Quartz	4.0-12.0	23.5-34.1	18.5
K-feldspar	<2	1.4-3.2	1.3
Plagioclase	<2	1.2-1.9	1.9
Calcite	8.0-57.0	6.1-14.6	31.6
Dolomite/ankerite	7.0-31.0	6.6-11.4	7.6
Clay minerals	29.0-53.0	41-45.2	36.6
Illite/mica [e]	-	58.2-60.9	60.1
Illite/smectite [e]	20-39	9.7	11.9
Chlorite [e]	9.0-14.0	29.1-39.1	24.5
Kaolinite [e]	<1	3	3.5
Pyrite	-	2.2	0.5
Hematite	-	0.12	2.1
Organic C	<0.1-0.3	-	0.13

[a] Xiang et al (2013); [b]Beauheim et al. (2014); [c] Koroleva et al. (2009); [d] Jackson et al. (2009); [e] Values are expressed as wt% of the clay fraction.

2.2.1 Sample preparation and apparatus

Samples for diffusion measurements were prepared in duplicate using a diamond coring bit to drill sample cores from the original 76-mm core sample. The samples (20-mm diameter and 20 to 23 mm length) were drilled normal to bedding, using air to cool the bit. Natural porewater in the Queenston shale is near saturation with respect to halite (Al et al., 2015; Clark et al., 2013) so any evaporation during sample preparation could result in halite precipitation and occlusion of the pores. In order to prevent this from affecting the porosity and diffusion measurements, a new approach was used whereby samples were initially resaturated in a closed chamber containing an open vessel with deionized water. The water chemical potential gradient between the deionized water and the sample porewater causes water transfer to the rock porewater via the vapor phase. Resaturation is accomplished by vapor-phase diffusion, and at the point when water droplets began to accumulate on the surface of the rock, the samples were fully immersed in a Queenston Synthetic Pore Water (Q-SPW; Table 2.2) formulated for the Queenston shale using methods modified after the approach of Cavé et al. (2009) and Xiang et al. (2013). The samples were immersed in Q-SPW under vacuum for four weeks prior to the start of experiments. Water- accessible porosity (ϕ_w) measurements were conducted on the rock material remaining after subcoring using the method described by Xiang et al. (2013). It is a gravimetric method that accounts for the porewater salinity and requires oven drying at 105 °C.

Table 2. 2 *Composition of Q-SPW and Queenston iodide tracer solution (Q-SPW-T) used in diffusion experiments.*

	Q-SPW	Q-SPW-T
Density (kg/L)	1.22	1.32

Element	mol/kgw	mol/kgw
Na	2.61	2.61
K	0.11	0.11
Ca	1.91	1.91
Mg	0.27	0.27
Cl	7.05	6.05
Br	0.06	0.06
Sr	0.02	0.02
I	0.00	1.00

A diffusion cell (Fig. 2.1) was specially designed to prevent expansion of the sample under the increased pressures experienced during nucleation and expansion of a gas phase in the pores (see below). An initial confining pressure of 0.83 MPa was applied to the samples using a calibrated relationship between vertical load and torque on the threaded end caps of the diffusion cell, similar to the approach employed by Van Loon et al. (2003). This confining pressure was intended to prevent expansion and damage to the sample during nucleation and growth of a gas phase, and it has no relationship to the confining pressure that affects the Queenston shale in natural subsurface conditions (12 MPa, Xiang et al. 2016). The cell was constructed with Delrin®, a form of polyoxymethylene thermoplastic, which was chosen for its rigidity and low X-ray attenuation and scattering properties. The silicone injection groves are created in a continuous spiral around the inner surface of the sleeve, allowing silicone to be injected in one of the ports and fill the annular space between the sample and the sleeve, forming an effective seal (Fig. 2.1).

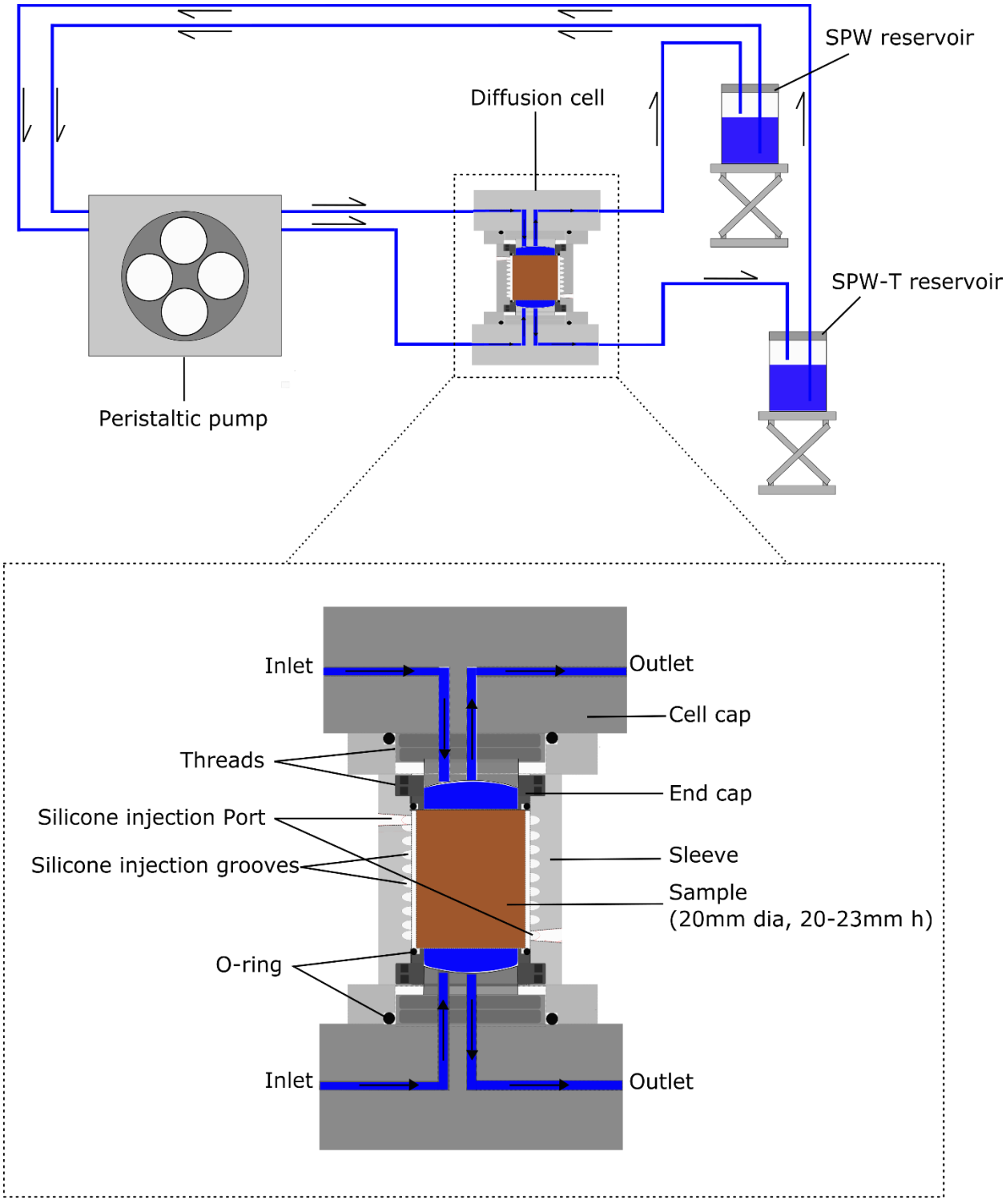

Fig. 2. 1 *Schematic diagram of the diffusion cell and experimental setup.*

2.2.2 Experimental procedures

Three sequential experimental procedures were performed on each of the duplicate samples (Fig. 2.2); first, in-diffusion experiments were conducted to establish diffusion coefficients for fully brine-saturated samples, the samples were then subjected to the gas generation procedure followed by measurement of the gas-saturation profiles, and finally, out-diffusion experiments were conducted to measure diffusion coefficients with the gas phase present.

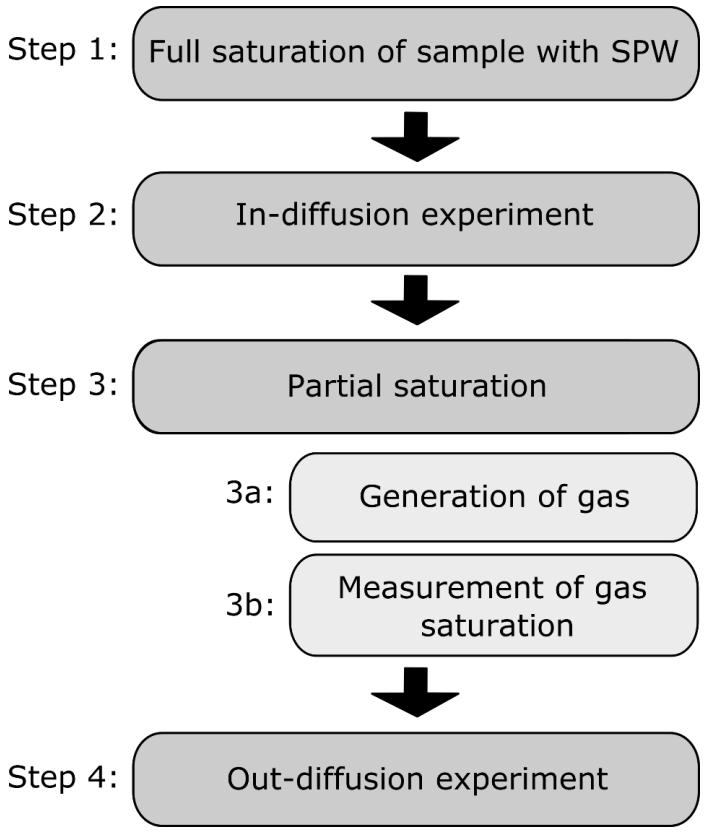

Fig. 2. 2 *Experimental procedures undertaken for a given sample.*

Diffusion measurements were conducted using the X-ray radiography technique described by Cavé et al. (2009) based on X-ray absorption by an aqueous iodide tracer (I^-). The method can be used to spatially resolve tracer concentrations through time, allowing for determination of pore diffusion coefficients (D_p), and to measure I^- accessible porosity (ϕ_I). Values of ϕ_I were determined for brine-saturated samples and for partially desaturated samples ($\phi_{I\text{-}g}$). A least squares regression analysis was used to obtain values for D_p by optimizing the fit between experimental data and the analytical solution to Fick's law (Crank et al., 1975):

$$C_i(x,t) = C_0 erfc \frac{x}{2\sqrt{D_p t}} \quad [2.1]$$

Were C_i is the concentration of tracer at distance x from the diffusion boundary at time (t) since the start of diffusion; C_0 is the concentration of tracer at the influx boundary, L is the maximum diffusion path length, equal to the sample thickness, and *erfc* is the complimentary error function. Having the initial and bounding conditions (Crank, 1975; Shackelford, 1991):

$$C_{(x,t)} = 0 \Big|_{x > 0}^{t = 0}$$

$$C_{(x,t)} = C_0 \Big|_{x = 0}^{t \geq 0}$$

$$C_{(x,t)} = 0 \Big|_{x = L}^{t \geq 0}$$

Measurements were conducted with an X-ray CT system (Pinnacle X-ray Systems, Atlanta, Georgia) equipped with a Varian® NDI-160/22 source coupled to a Gulmay® CPL series (CP2-1402) 3000 W generator and a Varian PaxScan®1313DX amorphous-silicon flat-panel

imaging detector. All data were collected as 16-bit tiff image files. Acquisition parameters were; 1 s exposure per frame, 32 frame averages per image, source voltage of 50 kV with 60 mA current, and source filtration with 3.3 mm aluminum. Prior to the start of diffusion experiments, the fluid reservoirs at the top and bottom of the diffusion cell (Fig. 2.1) were filled with Q-SPW solution. Experiments were initiated by replacing Q-SPW in the lower reservoir with I^- tracer solution (Q-SPW-T) prepared from the Q-SPW by substituting some NaCl with NaI (Table 2.2). Reference images (radiographs) were collected immediately after tracer solution was injected and images at different times were collected twice a day for the first two days, once a day for the following three days, and then the time interval increased to once every three-four days. All radiographs were collected with identical sample positioning and instrumental operating conditions. In all cases, pixel grey values from the radiograph images were converted to one-dimensional profiles that represent X-ray attenuation coefficients (μ) according to the method described by Cavé et al. (2009).

Diffusion was monitored in this way until tracer breakthrough occurred at the top boundary. The samples were then saturated with the I^- tracer solution by allowing in-diffusion from both ends. The influx of tracer was monitored by X-ray radiography over a period of eight to nine weeks until no further change in X-ray attenuation was observed. At this point, one-dimensional profiles of ϕ_t and C/C_0 were obtained following the method described by Cavé et al. (2009) and Agbogun et al. (2013). Relative concentration profiles allow for determinations of D_p by fitting experimental data to Equation 2.1, and when profiles are collected at different times the resulting D_p values can be averaged to find a representative value for the sample and the standard deviation provides an estimation of the variability associated with D_p. Repeat

measurements were conducted on several samples to assess uncertainty in the C/C_0 profiles due to instrumental positioning and source/detector variability. The point-to-point uncertainty, expressed as a relative standard deviation (RSD), is 0.39% which translates to an uncertainty in iodide concentration of 0.004 mol/kgw.

Three-dimensional CT scans where acquired to evaluate porosity and tracer concentration distributions throughout the sample following the calibrated approach described by Agbogun et al. (2013). Measurements were conducted with an X-ray CT system (Pinnacle X-ray Systems, Atlanta, Georgia) equipped with a Hamamatsu L12161-07 X-ray source and a Varian PaxScan®1313DX amorphous-silicon flat-panel imaging detector. All data were collected as 16-bit tiff image files. Acquisition parameters were; 5 s exposure per frame, 8 frame averages per projection image, source voltage of 60 kV with 250 uA current, source filtration with 3.3 mm aluminum and a rotational step of 0.75 degrees.

The 3-D CT image sets were collected before the diffusion experiments and after the samples were saturated with iodide solution. Projection image sets were reconstructed with NRECON-V1.7.1.0 (Bruker MicroCT), creating stacks of 2-D slices representing the full 3-D volume of each sample. The final CT datasets (iodide saturated) were digitally registered to the initial datasets using the Manual Seed Registration code (Williamson, 2009). The registrations were conducted using the coordinate positions of magnetite grains fixed as fiduciary points around the sample. Beam hardening effects were taken into account with a quantitative beam hardening approach detailed in Appendix D.4.2.2 Details of the CT data processing are presented in Appendix D.2.

2.3 Partial gas saturation

The fully tracer-saturated samples were subjected to partial gas generation with an approach that uses N_2 gas and takes advantage of the variability of N_2 solubility versus pressure as indicated by Henry's law (Equation 2.2):

$$S_i = K_{H_i} P_i \quad [2.2]$$

where S_i is the solubility of gas i (mol/L) in an aqueous solution; K_H is the Henry's constant ($mol \cdot L^{-1} \cdot atm^{-1}$ or M/atm); P_i is the partial pressure (atm). However, with increasing gas partial pressures the solubility-pressure relationship becomes non-linear and deviates from Henry's law. The solubility of N_2 in high ionic strength aqueous solutions (up to 7.7 mol/L) at 25°C can be calculated as a function of partial pressure, P_{N2}, using the model reported by Mao and Duan (2006). Calculations for the Queenston shale were conducted at the 7.7 mol/L ionic-strength limit of the model although the Q-SPW was a Na-Ca-Cl solution with ionic strength of 9.2 mol/kgw. As a result, the N_2 solubility in Q-SPW will be slightly overestimated by the model.

The method for generating partial saturation is based on the premise that changes in N_2 partial pressure from high (P_1) to low (P_2) causes the solubility of N_2 to decrease with the result that gas bubbles will form in the solution. For a brine solution occupying the pore spaces in a rock sample, gas bubbles should form in the pore spaces. If equilibrium is established at P_2, using the Henry's law approach, the moles of N_2 bubbles (n) can be calculated according to:

$$n_{bubble} = K_H V_p (P_1 - P_2) \quad [2.3]$$

where, V_p is the volume of the rock pores (L) initially occupied by brine. The volume of the gas bubbles (V_{bubble}; L) formed at P_2 can be calculated using the ideal gas law:

$$V_{bubble} = \frac{K_H V_p (P_1 - P_2) RT}{P_2} \quad [2.4]$$

If we assume that Henry's law and the ideal gas law are valid, the predicted volume occupied by gas (S_g%) will be:

$$S_g = \left[\frac{K_H (P_1 - P_2) RT}{P_2}\right] * 100\% \quad [2.5]$$

As noted previously, Henry's law does not accurately represent the gas solubility at high ionic strengths and, more importantly, it is not expected that the ideal gas law, as presented in Equation 2.5, can accurately represent gas bubble formation in the confined pore space of clay-rich rocks. In order for gas bubbles to nucleate and grow, porewater must be expelled from the system, so the process is limited by the relative permeability for the aqueous phase, which decreases with time due to the formation of the gas phase. Also, during the time required to expel porewater, N_2 will be lost from the system by diffusion in both the aqueous phase and, increasingly, in the growing gas phase. For these reasons, it is expected that the volume of gas phase created in the pore spaces will be lower than that predicted by Equation 2.5. X-ray radiography was used to quantify the final degree of N_2 saturation, but the method is limited to measurements of gas saturation in the tracer-accessible pore space.

As a first step toward inducing partial gas saturation, the diffusion cells, with end caps removed, were immersed for 33 days in I^- tracer solution inside a pressure vessel with 68 atm $N_{2(g)}$ in the head space. The high N_2 gas pressure causes an increase in N_2 solubility, allowing for

diffusion of elevated aqueous N_2 concentrations throughout the pore space of the rock. Based on the D_p values determined for I^- by in-diffusion, the time period of 33 days was considered sufficient to achieve 90 – 100% of the fully-equilibrated N_2 distribution in the sample. In the second step, the $N_{2(g)}$ overpressure in the head space was decreased to 1 atm which initiates nucleation and growth of $N_{2(g)}$ bubbles in the pore spaces, forcing tracer solution out of the sample. The evolution of partial gas saturation was monitored by X-ray radiography, and five days were sufficient for equilibration of the gas and brine saturation states. After equilibration between the gas phase and the tracer-containing brine, one-dimensional profiles of μ were collected again and used to obtain 1-D profiles of the I^-- accessible porosity in the presence of the gas phase ($\phi_{I\text{-}g}$). The ratio between $\phi_{I\text{-}g}$ and ϕ_I was used to determine the fraction of gas saturation ($S_{g\text{-}I}$) in the I^--accessible pore fraction.

$$S_{g-I} = \left[1 - \left(\frac{\phi_{I-g}}{\phi_I}\right)\right] 100\% \qquad [2.6]$$

Anion exclusion in clay-rich rocks leads to a condition where $\phi_I < \phi_w$, so it's important to note that these reported values for $S_{g\text{-}I}$ represent fractions of ϕ_I, rather than ϕ_w. In order to represent the gas-saturation values as a fraction of ϕ_w, we multiply by the fraction of anion-accessible porosity (f_a):

$$S_{g-w} = f_a \cdot S_{g-I} \qquad \text{where: } f_a = \phi_I/\phi_w \qquad [2.7]$$

The use of this relationship assumes that gas-bubble nucleation and growth occurs in the largest connected pores, which are also the anion-accessible pores. This assumption is consistent with known relationships between capillary-pressure and saturation.

Out-diffusion experiments were initiated with the partially-saturated samples by introducing Q-SPW (no tracer) into the reservoir adjacent to the influx boundary. In order to eliminate density effects, the cell was upended to maintain the higher-density solution at the bottom (outflux) boundary (Table 2.2). Radiographs were collected at different times using the same time increments as for in-diffusion experiments.

2.4 References

Agbogun, H.M.D., Hussein, E.M.A., Al, T.A., 2013. Assessment of x-ray micro-CT measurements of porosity and solute concentration distributions during diffusion in porous geologic media. J. Porous Media 16, 683–694.

Al, T.A., Clark, I.D., Kennell, L., Jensen, M., Raven, K.G., 2015. Geochemical evolution and residence time of porewater in low-permeability rocks of the Michigan Basin, Southwest Ontario. Chem. Geol. 404, 1–17.

Beauheim, R.L., Roberts, R.M., Avis, J.D., 2014. Hydraulic testing of low-permeability Silurian and Ordovician strata, Michigan Basin, southwestern Ontario. J. Hydrol. 509, 163–178.

Cavé, L., Al, T., Xiang, Y., Vilks, P., 2009. A technique for estimating one-dimensional diffusion coefficients in low-permeability sedimentary rock using X-ray radiography: comparison with through-diffusion measurements. J. Contam. Hydrol. 103, 1–12.

Clark, I.D., Al, T., Jensen, M., Kennell, L., Mazurek, M., Mohapatra, R., Raven, K.G., 2013. Paleozoic-aged brine and authigenic helium preserved in an Ordovician shale aquiclude. Geology 41, 951–954.

Crank, J., 1979. The mathematics of diffusion. Oxford university press.

Jackson, R., 2009. Organic Geochemistry and Clay Mineralogy of DGR-3 and DGR-4 Core, Revision 0. TR-08-29. Report prepared for Intera Engineering Ltd., November, 2009. Report available online through http://www.nwmo.ca.

Koroleva, M., de Haller, A., Mader, U., Waber, H.N., Mazurek, M., 2009. Borehole DGR-2: Pore-Water Investigations, Revision 0. TR-08-06. Report prepared for Intera Engineering Ltd. (now Geofirma Engineering Ltd.), August, 2009. Report available online through http://www.nwmo.ca.

Mao, S., Duan, Z., 2006. A thermodynamic model for calculating nitrogen solubility, gas phase composition and density of the N2--H2O--NaCl system. Fluid Phase Equilib. 248, 103–114.

Van Loon, L.R., Soler, J.M., Bradbury, M.H., 2003. Diffusion of HTO, 36 Cl- and 125 I- in Opalinus Clay samples from Mont Terri: effect of confining pressure. J. Contam. Hydrol. 61, 73–83.

Williamson, M.D., 2009. An efficient algorithm for 3D image registration. M.Sc. thesis. Department of Computer Science. University of New Brunswick.

Xiang, Y., Al, T., Scott, L., Loomer, D., 2013. Diffusive anisotropy in low-permeability Ordovician sedimentary rocks from the Michigan Basin in southwest Ontario. J. Contam. Hydrol. 155, 31–45.

Chapter 3: Results and discussion

3.1 Porosity

Measurements of ϕ_w range from 0.101 to 0.103 (Table 3.1) and provide representative values at the sample scale, but they give no indication of smaller scale variability. Alternatively, X-ray radiography provides 1-D spatially-resolved measurements of ϕ (Cavé et al., 2009; Tidwell et al., 2000). These measurements indicate that there are mm-scale cyclical changes in porosity across the samples in the direction normal to bedding (Fig. 3.1). Three-dimensional porosity distributions display similar cyclical changes in porosity, although the 3-D images display significant ring artifacts and beam hardening effects, leading to significant uncertainty and error (Fig. 3.2). These features were initially thought to be due to bedding and grain-size controlled porosity variations, but petrographic examination by scanning electron microscopy (SEM) revealed that they reflect bedding-parallel dolomite-cemented lenses; the dolomite domains having lower porosity than the surrounding alumino-silicate (shale) domains (Fig. 3.3). There is a larger-scale variation in porosity evident in both samples, with the highest porosity (approximately 0.065 to 0.070) at the influx boundary, reaching a minima of approximately 0.055 at a distance of 0.014 m, and then increasing slightly with increasing distance (Fig. 3.2). Average ϕ values derived from the 1-D profiles for brine-saturated samples range between 0.054 and 0.059 and their standard deviations reflect the internal variability in each sample (Table 3.1). These measurements indicate that the fraction of anion-accessible porosity (*fa*), represented by ϕ_i/ϕ_w ranges from 0.53 to 0.58 (Table 3.1). This is consistent with data reported by Xiang et al. (2013) and with previous research that indicates anion-accessible porosity in clay-rich rocks is lower than the total accessible porosity (Appelo et al., 2010; Bazer-

Bachi et al., 2006; Descostes et al., 2008; García-Gutiérrez et al., 2006; Mazurek et al., 2015; Van Loon et al., 2003a, 2003b, 2007).

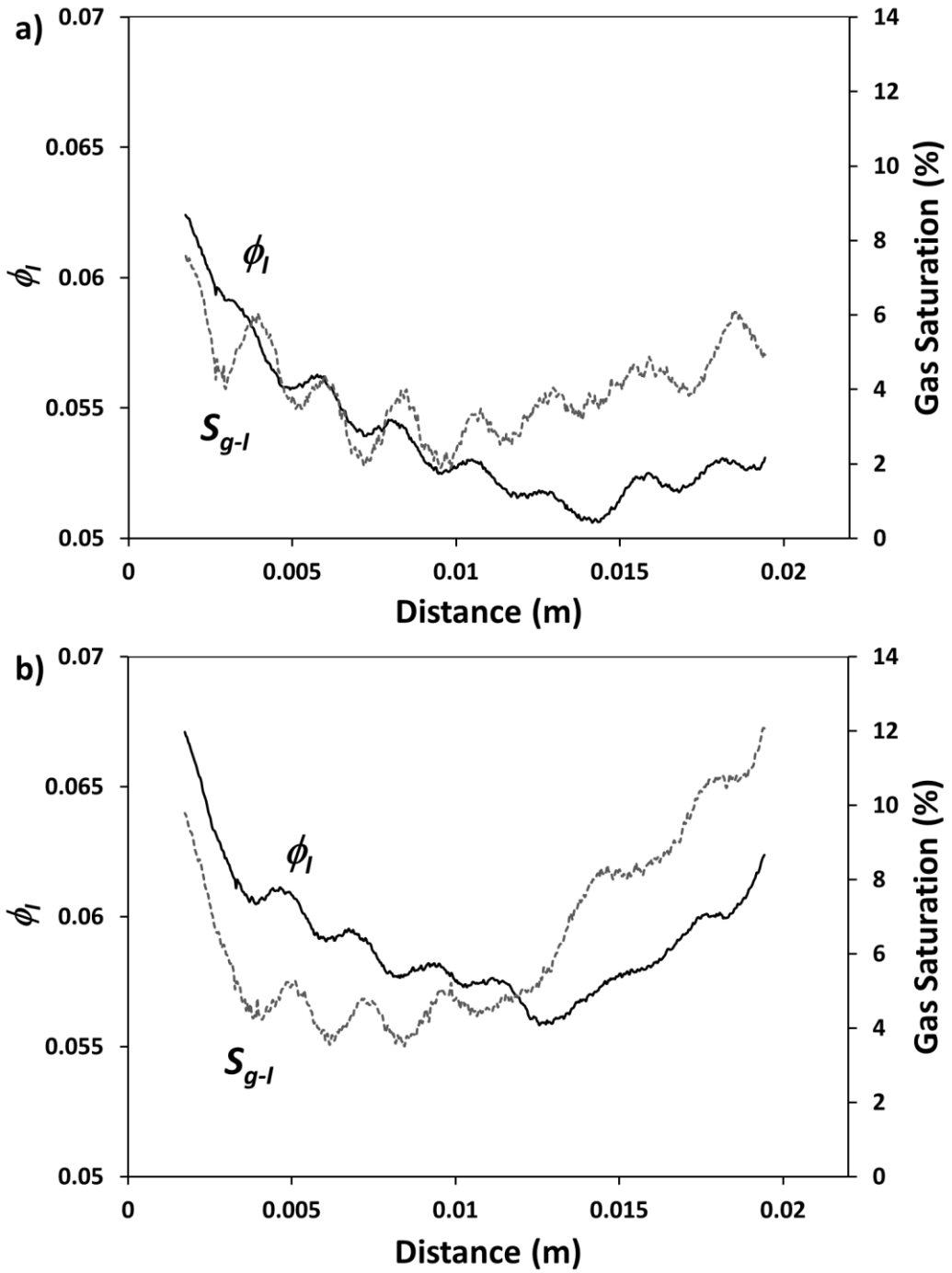

Fig. 3. 1 *Profiles for the spatial distribution of ϕI and gas saturation (S_{g-I}) in samples a) DGR3-472-A, and b) DGR3-472-B. Note that S_{g-I} values are relative to the total iodide-accessible porosity. The combined geometry of the samples and the cone-shaped X-ray beam causes some minor blurring of the signal near the boundaries, resulting in loss of data over a small distance.*

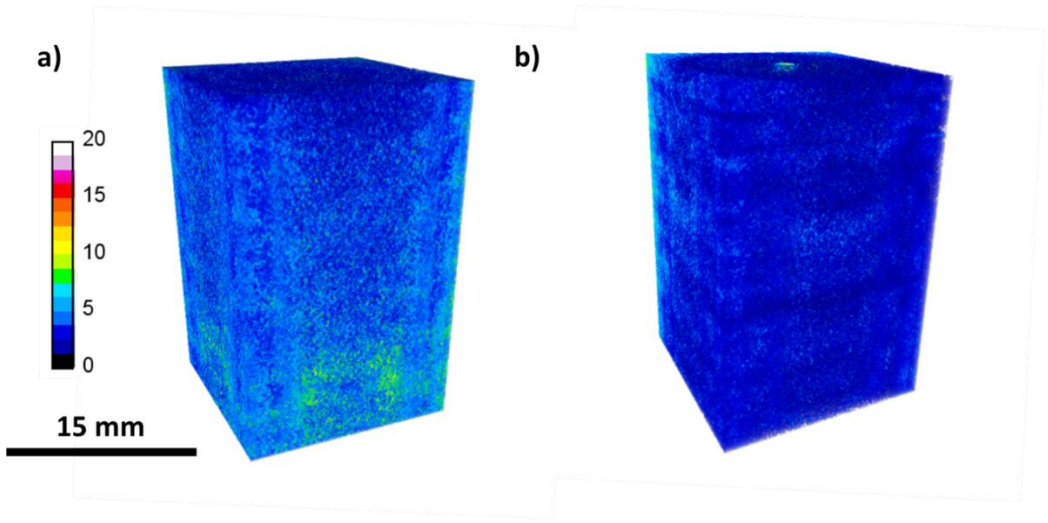

Fig. 3.2 *3-D computed tomographic image of a selected region reconstructed from projection data sets collected during saturated diffusion experiments for a) DGR3 472.56 A and b) DGR3 472.56 B. The colour legend represents the volume fraction (%) of each voxel that is accessible to the iodide tracer by diffusion.*

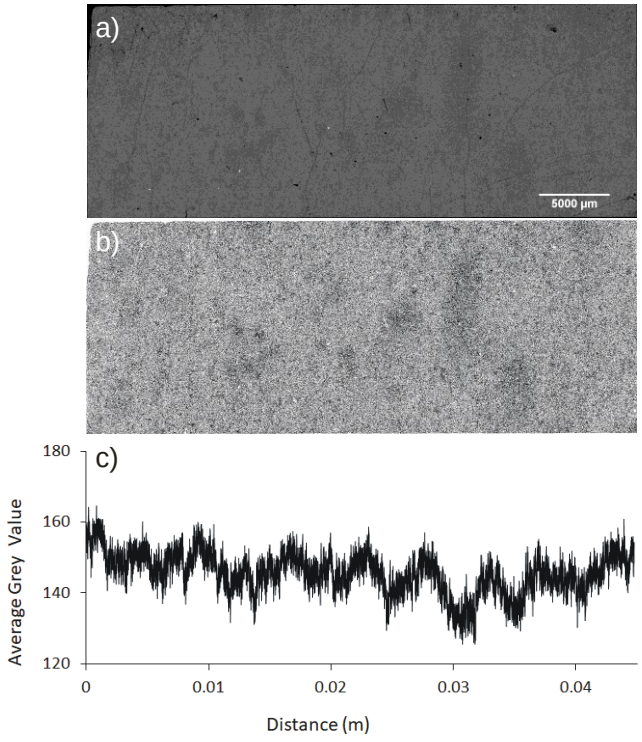

Fig. 3. 3 *a) A back-scattered-electron image from a petrographic thin section prepared directly adjacent to the diffusion samples. The plane of the section is oriented normal to bedding. b) A binary image of the region shown in (a), binarized using grey-scale thresholding to emphasize dolomite-rich regions (black). c) A profile generated from the binary image and displaying the average grey value for each column of pixels versus distance. The cyclical low grey values represent dolomite-cemented regions that have relatively low porosity.*

Table 3. 1 *Comparison of results from in-diffusion measurements on fully saturated samples to out-diffusion measurements on partially saturated (PS) samples.*

Sample	DGR3 472.56-A	DGR3 472.56-A-PS	DGR3 472.56-B	DGR3 472.56-B-PS
Water accessible porosity (ϕ_w)	0.101–0.103			
Iodide accessible porosity (ϕ_I)	0.054± [0.0030]	0.052± [0.0026]	0.059± [0.0024]	0.055± [0.0024]
f_a[a]	0.53		0.58	
$S_{g\text{-}I}$ %[b]	0	4.0± [1.1]	0	6.7± [2.6]
D_p (m^2/s)	5.8×10^{-11}± 2.6×10^{-12}	4.8×10^{-11}± 1.5×10^{-12}	4.8×10^{-11}± 2.9×10^{-12}	4.2×10^{-11}± 3.1×10^{-12}
ΔD_p (%)	18.9		13.3	
D_e (m^2/s)	3.1×10^{-12}± [2.4×10^{-13}]	2.5×10^{-12}± [1.5×10^{-13}]	2.8×10^{-12}± [2.3×10^{-13}]	2.3×10^{-12}± [2.2×10^{-13}]
ΔD_e (%)	22.3		20.3	

[a] Values of f_a are calculated from ϕ_I and ϕ_w measurements on adjacent samples.

[b] Gas saturation values are relative to ϕ_I.

3.2 Diffusion in saturated shale

Profiles of relative tracer concentrations (C/C_0) collected at different times in the porewater-saturated samples are shown in Figure 3.4a,b. The $D_{p\text{-}I}$ values derived from fitting the experimental data to the analytical model (Equation 2.1) range from 4.8×10^{-11} to 5.8×10^{-11} m^2/s (Table 3.1). These values can be transformed to the more commonly reported effective diffusion coefficient (D_e):

$$D_e = D_p \phi_I = \frac{\delta}{\tau^2} D_0 \phi_I \quad [3.1]$$

where δ is the pore constrictivity, τ is the tortuosity and D_0 is the free-water diffusion coefficient. The constrictivity and the tortuosity cannot be measured independently and are often combined in one tortuosity factor τ_f:

$$\tau_f = \frac{\delta}{\tau^2} \quad [3.2]$$

This results in a range of D_e from 2.8 x 10^{-12} to 3.1 x 10^{-12} m^2/s which is consistent with values reported for the Queenston Formation by Xiang et al. (2013) (Table 2.1). By propagating the error from the averaged ϕ values, and from multiple D_p values determined from C/C_0 data collected at different times, uncertainty bounds were calculated for D_e to reflect heterogeneity within a single sample. When expressed as the relative standard deviation, these are on the order of 7.7 to 8.2% (presented as 1 σ in Table 3.1). The variation in D_e between samples is similar (9.7%) indicating that adjacent samples have indistinguishable diffusion properties.

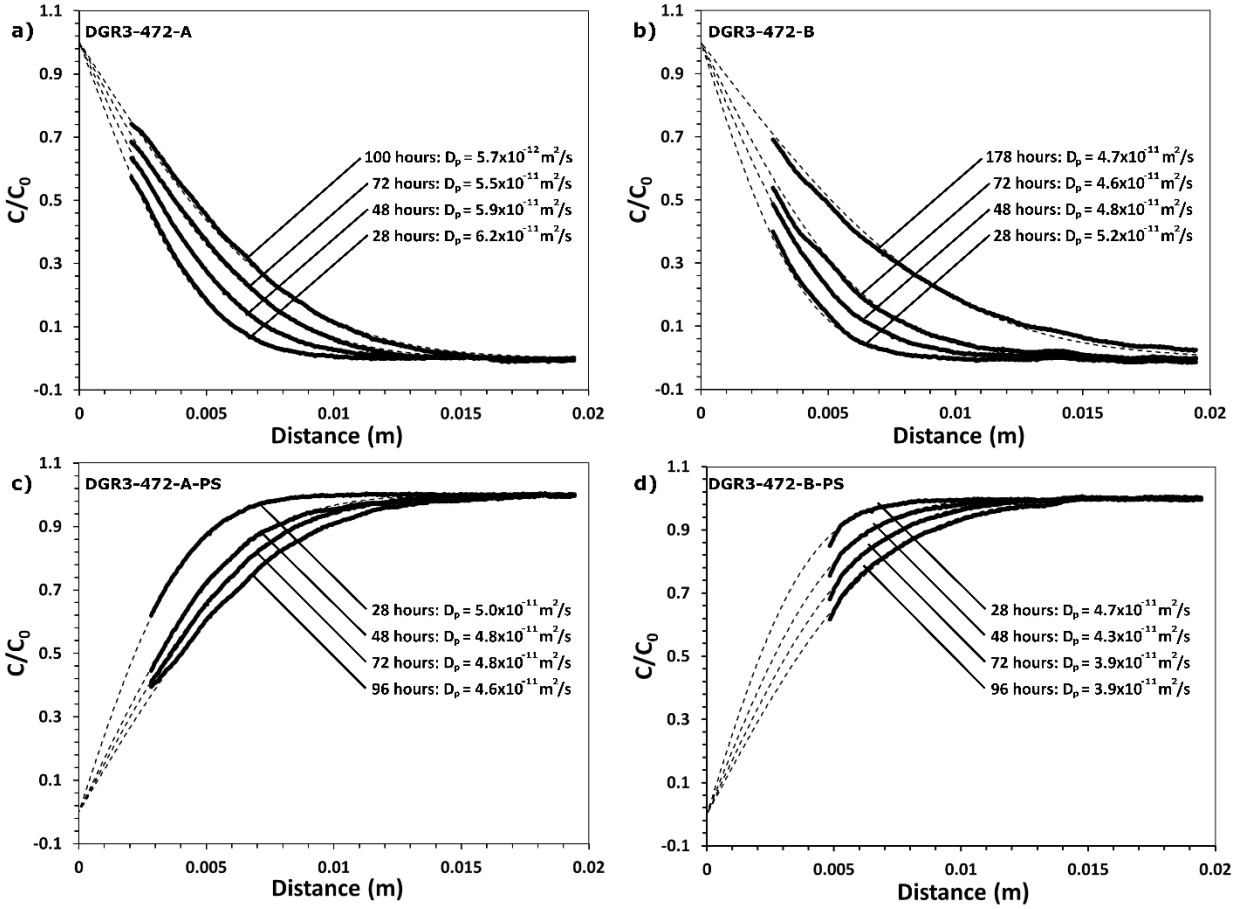

Fig. 3. 4 *One-dimensional, profiles of relative iodide concentration (C/C0) collected at different times: a) in-diffusion experiment with 0 % gas saturation (sample DGR-3-472.56-A), b) in-diffusion experiment with 0 % gas saturation (sample DGR-3-472.56-B) c) out -diffusion experiment with 4.0 % gas saturation (sample DGR-3-472.56-A), d) out-diffusion experiment with 6.7 % gas saturation (sample DGR-3-472.56-B). The combined geometry of the samples and the cone-shaped X-ray beam causes some minor blurring of the signal near the boundaries, resulting in loss of data over a small distance. However, the fitting procedure relies on the whole data profile and the imposed boundary condition, so the influence of this data gap near the boundary on the D_p determination should be negligible.*

3.3 Partial gas saturation

The radiographic measurements of gas saturation ($S_{g\text{-}I}$) represent the fraction of gas volume in the pore space relative to the total iodide-accessible pore volume (Equation 2.6). This paper is focused on iodide diffusion, so we use this approach consistently throughout.

As expected, gas saturation values are much lower than those predicted by Equation 2.5 which indicates values of approximately 28 % for P_1 = 68 atm. The profiles for gas saturation display cyclic variations that correlate with those observed in the profiles of ϕ (Fig. 3.1), with low and high points in the cycles reflecting the presence or absence, respectively, of secondary dolomite lenses (Fig. 3.3). The profiles are broadly U-shaped, with values at the influx and outflux boundaries ranging from 5 to 13%, and values midway along the length ranging from 2 to 5 % (Fig. 3.1). This observation is consistent with the expectation that gas bubbles will nucleate and grow faster near the boundaries because porewater can be expelled more rapidly due to a higher pressure gradient. The decreasing degree of gas saturation inward from the boundaries is also expected because, as the volume of gas increases near the boundaries, the relative permeability for the aqueous phase decreases (Van Genuchten, 1980), slowing the expulsion of porewater from the interior. This leads to a corresponding increase in the time available for N_2 loss by diffusion, and the rate of diffusive loss of N_2 will increase with time because the diffusion coefficient for N_2 will increase as the gas phase grows (Reardon and Moddle., 1985).

The foregoing discussion considers processes operative within a porous media with uniform porosity and pore-size distribution, but porosity in the Queenston Formation shale is not uniformly distributed (Fig. 3.1), and a uniform pore-size distribution is unlikely. In this case, during the initial stages of depressurization and gas exsolution, a random distribution of gas nucleation sites might be expected throughout the pore spaces (Du and Yostsos, 1999), but for nuclei to grow into bubbles, porewater must be forced out of the rock sample by advection. Consequently, gas bubbles will grow preferentially in small connected regions of the rock with relatively high permeability, and when these preferential pathways are connected by a

continuous gas phase, a critical gas saturation will be reached, allowing flow of the gas phase (Firoozabadi et al., 1992). It is possible that critical gas saturation was reached near the boundaries of the samples, but almost certainly not in the interior regions of the samples.

The gas-ingrowth mechanism used for these experiments is similar to what might occur at a larger scale in a natural organic-rich shale when hydrocarbon gases build up and exceed solubility, causing partial gas saturation. It is different from the dewatering mechanism used by (Savoye et al., 2010, 2012, 2014), which may better reflect evaporative and drainage processes in wall rocks adjacent to underground excavations. Dewatering is similar to the gas-ingrowth mechanism in that it will begin with water loss in the largest pores, however with gas ingrowth, once critical gas saturation is reached, growth of the gas phase will diminish or cease (Due and Yostros., 1999). If dewatering is accomplished by outflow of water, then the limit to dewatering should be reached at the percolation threshold, but if the water is removed by evaporation, or if a chemical potential gradient is employed, as with the osmotic technique used by Savoye et al. (2010, 2012, 2014), then water loss can continue via vapour-phase transfer and result in dewatering beyond the percolation threshold. Consequently, dewatering methods can generate a higher degree of gas saturation than gas exsolution and ingrowth.

3.4 Diffusion in partially saturated shale

Profiles of relative tracer concentrations (C/C_0) collected at different times in the partially saturated samples are shown in Figure 3.4c,d. The consistent baseline for the profiles (baseline = 1) demonstrates that the gas-saturation profiles are stable through time. Ingrowth of 4 % gas in sample DGR3-472-A results in a decrease of D_e by 22.3 % from 3.1×10^{-12} to 2.5 x

10^{-12} m^2/s and 6.7 % gas saturation in sample DGR3-472-B causes D_e to decrease by 20.3 % from $2.8x10^{-12}$ to 2.3 x 10^{-12} m^2/s (Table 3.1). These data demonstrate that diffusive transport in these rocks is dominated by a small fraction of the pore space such that generation of a small amount of gas has a significant effect on diffusivity. The decrease in D_e is partially accounted for by the decrease in ϕ, but the dominant factor is a decrease in τ_f (decreased δ and/or increased τ).

Archie's 2nd law has commonly been used to describe diffusion and electrical conduction in variably saturated porous media (Archie, 1942; Hamamoto et al., 2009; Hamamoto et al., 2010; Marshall, 1959; Mualem and Friedmen, 1991; Savoye et al., 2010, 2012, 2014). According to Hamamoto et al. (2010), Archie's 2nd law can be described by Equations 10 and 11:

$$\frac{D_e}{D_0} = \phi_w^m \left[\frac{\phi}{\phi_w}\right]^n \quad [3.3]$$

$$\frac{D_e}{D_e^*} = \left[\frac{\phi}{\phi_w}\right]^n \quad [3.4]$$

where ϕ is the water-filled porosity under partially saturated conditions, D_e is the effective diffusion coefficient for iodide at a given saturation; D_e^* is the effective diffusion coefficient in the fully saturated sample, *m* is the cementation exponent and *n* is the saturation exponent. Archie's laws have been known to underestimate diffusivity and it has been suggested by many authors (Balberg et al., 1986; Hamamoto et al., 2010; Martys, 1999; Moldrup et al., 2007; Savoye et al., 2010) that there is a critical water saturation at which the water phase is no longer connected and transport through the porewater is no longer possible at a representative

scale. Hamamoto et al. (2010) proposed a modified form of Archie's 2nd law to include a percolation threshold:

$$\frac{D_e}{D_0} = (\frac{\phi-\phi_{th}}{\phi_w-\phi_{th}})^n * (\phi_w - \phi_{th}{}^*)^m \quad [3.5]$$

$$\frac{D_e}{D_e{}^*} = (\frac{\phi-\phi_{th}}{\phi_w-\phi_{th}})^n \quad [3.6]$$

Where $\phi_{th}{}^*$ represents the fraction of the fluid phase that, under saturated conditions, does not participate in the solute-transport process, and ϕ_{th} represents the percolation threshold. In clay-rich rocks where diffusion is expected to be the dominant transport process, the assumption by Savoye et al. (2014) and Van Loon and Mibus (2015) that $\phi_{th}{}^*$ is equal to the fraction of the porewater that is inaccessible to anions is logical and seems reasonable. Furthermore, Hamamato et al. (2010) and Savoye et al. (2014) suggested it can be assumed that ϕ_{th} is equal to $\phi_{th}{}^*$.

Archie's law is an empirical relationship and there has been significant work directed at understanding the cementation exponent (*m)* in a variety of materials (Balberg, 1986; Boving and Grathwohl, 2001; Hunt, 2004; Revil and Cathles, 1999; Sen et al., 1981; Thompson et al., 1987; Van Loon and Mibus, 2015). In previous research on clay-rich rocks, *m* has been estimated to range from 2 to 3 (Descostes et al., 2008; Jacquier et al., 2013; Revil and Cathles, 1999; Savoye et al, 2010; Van Loon et al., 2003b; Van Loon and Mibus, 2015). Using Equation 3.5 and parameters presented in Table 3.1, we obtain values for *m* that fall in the same range (2.19 and 2.30 for DGR3-472-A and DGR3-472-B respectively; Table 3.2). There is a small number of published studies aimed toward understanding the values of the saturation

exponent (*n*) for various materials. In soils and sands, values for both *m* and *n* roughly equal to 2 have been found to provide a good fit to many data sets (Archie, 1942; CRWMS M&O, 2000; Revil and Jougnot, 2008; Hammanto et al., 2010; Thompson et al., 1987; Salem and Chilingarian, 1999). We are aware of only two studies (Savoye et al., 2010, 2014) that note values for *n* in clay rich rocks; they used a value of *n*=2 but acknowledged that it was associated with significant uncertainty.

It is desirable to have a generalized empirical relationship such as Archie's 2nd law that could allow estimation of diffusion coefficients as a function of saturation. Based on Equation 3.6, this would require confidence in the determination of values for *n* and ϕ_{th}. As noted above, in clay-rich rocks where diffusion is the dominant transport process, it should be reasonable to assume that ϕ_{th}^* is equal to the anion inaccessible porosity, and this parameter can be measured for I^- using the X-ray radiography technique described herein and by Cavé et al. (2009). However, desaturation and anion diffusion are very different processes, so we are less confident in the assumption that $\phi_{th} = \phi_{th}^*$ as suggested by Hamamato et al. (2010) and Savoye et al. (2014). However, considering capillarity constraints on desaturation and anion-size constraints on diffusion, we expect that ϕ_{th}^* should represent the lower bound for ϕ_{th}; or $\phi_{th}^* \leq \phi_{th}$. With little known about the value of *n* in clay-rich rocks, it is difficult to constrain, but since $n = 2$ has been used in previous studies (Savoye et al., 2010, 2014), we used that value in Equation 3.6 to calculate ϕ_{th}. Alternatively, we used the assumptions noted above that the anion-inaccessible porosity is equal to ϕ_{th}^*, which in turn is equal to ϕ_{th}, to calculate *n* with Equation 3.6 ($\phi_{th}^* = \phi_w - fa \cdot \phi_w$). With this approach, we obtain values for *n* that range from 5.7 to 2.8, and values for ϕ_{th} that range from 0.082 to 0.059 (Table 3.2). The derived values for ϕ_{th}

conform with our expectation that $\phi_{th}^* \leq \phi_{th}$, but in diffusion-dominated systems where ϕ_{th} is not known, but ϕ_{th}^*can be determined from f_a, the best approach to understand the *n* exponent in Archie's 2nd law should be to assume $\phi_{th} = \phi_{th}^*$ and then calculate values for *n* with Equation 3.6. This method was used to generate the curves on Figure 3.5 where it is obvious that when the degree of water saturation is high, diffusion coefficients obtained from Equation 3.6 are not highly sensitive to variations in *n*. This paper is primarily intended to present a new method for diffusion measurements with partially-saturated systems and it is clear that additional data are required to further refine Archie's 2nd law for clay-rich rocks. Additional further discussion and investigations are needed on the role of gas distrubution within the pore space and its effects on Archie's law exponents.

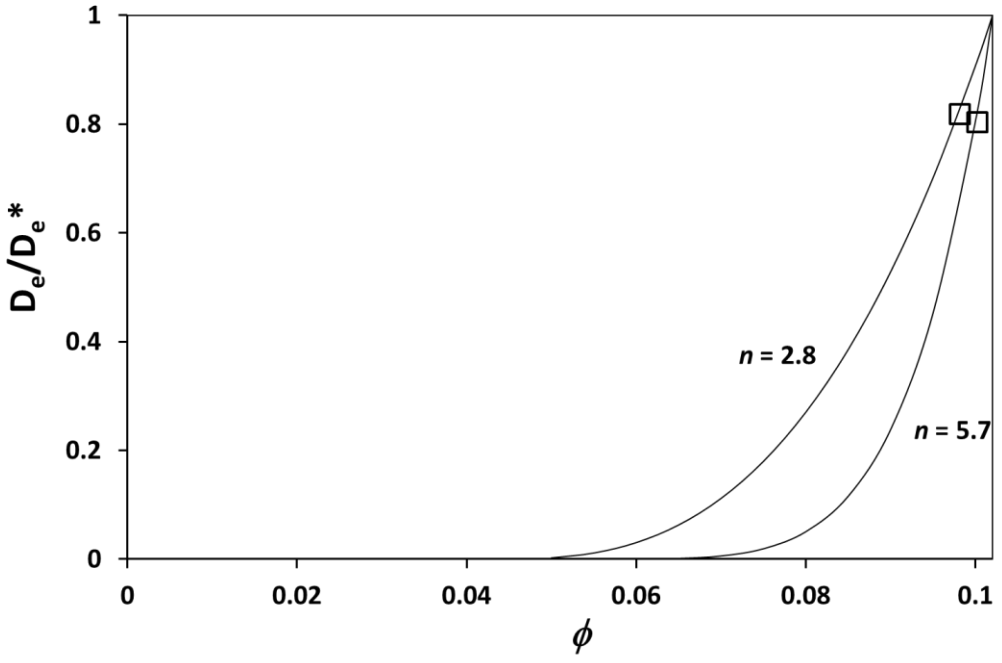

Fig. 3. 5 *Illustration based on Equation 3.6 to show variation in the iodide effective diffusion coefficient as a function of the water-filled porosity. Parameters are from Table 3.2. The square symbols represent measurements conducted in this study.*

Table 3. 2 *List of parameters used to estimate the range of values for n and ϕ_{th} with Equation 3.6.*

	Estimate Values for *n*		Estimate Values for ϕ_{th}	
	DGR-3 472.56-A	DGR-3 472.56-B	DGR-3 472.56-A	DGR-3 472.56-B
Saturation exponent (*n*)	5.7	2.8	2	2
Percolation threshold (ϕ_{th})	0.048	0.043	0.082	0.059
Cementation exponent (*m*)	2.19	2.30	2.19	2.30
Inactive Fluid phase *(ϕ_{th}*)*	0.048	0.043	0.048	0.043
Water-accessible porosity *(ϕ_w)*	0.102	0.102	0.102	0.102

3.6 References

Appelo, C.A.J., Van Loon, L.R., Wersin, P., 2010. Multicomponent diffusion of a suite of tracers (HTO, Cl, Br, I, Na, Sr, Cs) in a single sample of Opalinus Clay. Geochim. Cosmochim. Acta 74, 1201–1219.

Archie, G.E., others, 1942. The electrical resistivity log as an aid in determining some reservoir characteristics. Trans. AIME 146, 54–62.

Balberg, I., 1986. Excluded-volume explanation of Archie's law. Phys. Rev. B 33, 3618.

Bazer-Bachi, F., Tevissen, E., Descostes, M., Grenut, B., Meier, P., Simonnot, M.-O., Sardin, M., 2006. Characterization of iodide retention on Callovo-Oxfordian argillites and its influence on iodide migration. Phys. Chem. Earth, Parts A/B/C 31, 517–522.

Boving, T.B., Grathwohl, P., 2001. Tracer diffusion coefficients in sedimentary rocks: correlation to porosity and hydraulic conductivity. J. Contam. Hydrol. 53, 85–100.

Cavé, L., Al, T., Xiang, Y., Vilks, P., 2009. A technique for estimating one-dimensional diffusion coefficients in low-permeability sedimentary rock using X-ray radiography: comparison with through-diffusion measurements. J. Contam. Hydrol. 103, 1–12.

Descostes, M., Blin, V., Bazer-Bachi, F., Meier, P., Grenut, B., Radwan, J., Schlegel, M.L., Buschaert, S., Coelho, D., Tevissen, E., 2008. Diffusion of anionic species in Callovo-Oxfordian argillites and Oxfordian limestones (Meuse/Haute--Marne, France). Appl. Geochemistry 23, 655–677.

Du, C., Yortsos, Y.C., 1999. A numerical study of the critical gas saturation in a porous medium. Transp. Porous Media 35, 205–225.

Firoozabadi, A., Ottesen, B., Mikklesen, M., others, 1992. Measurements of Supersaturation and Critical Gas Saturation (includes associated papers 27920 and 28669). SPE Form. Eval. 7, 337–344.

García-Gutiérrez, M., Cormenzana, J.L., Missana, T., Mingarro, M., Molinero, J., 2006. Overview of laboratory methods employed for obtaining diffusion coefficients in FEBEX compacted bentonite/Descripci{ó}n de los m{é}todos de laboratorio empleados para obtener coeficientes de difusi{ó}n en bentonita compactada FEBEX. J. Iber. Geol. 32, 37.

Hamamoto, S., Moldrup, P., Kawamoto, K., Komatsu, T., 2010. Excluded-volume expansion of Archie's law for gas and solute diffusivities and electrical and thermal conductivities in variably saturated porous media. Water Resour. Res. 46.

Hamamoto, S., Perera, M.S.A., Resurreccion, A., Kawamoto, K., Hasegawa, S., Komatsu, T., Moldrup, P., 2009. The solute diffusion coefficient in variably compacted, unsaturated volcanic ash soils. Vadose Zo. J. 8, 942–952.

Hunt, A.G., 2004. Continuum percolation theory and Archie's law. Geophys. Res. Lett. 31.

Jacquier, P., Hainos, D., Robinet, J.C., Herbette, M., Grenut, B., Bouchet, A., Ferry, C., 2013. The influence of mineral variability of Callovo-Oxfordian clay rocks on radionuclide transfer properties. Appl. Clay Sci. 83, 129–136.

Marshall, D.J., Madden, T.R., 1959. Induced polarization, a study of its causes. Geophysics 24, 790–816.

Martys, N.S., 1999. Diffusion in partially-saturated porous materials. Mater. Struct. 32, 555–562.

Mazurek, M., Oyama, T., Wersin, P., Alt-Epping, P., 2015. Pore-water squeezing from indurated shales. Chem. Geol. 400, 106–121.

Moldrup, P., Olesen, T., Blendstrup, H., Komatsu, T., de Jonge, L.W., Rolston, D.E., 2007. Predictive-descriptive models for gas and solute diffusion coefficients in variably saturated porous media coupled to pore-size distribution: IV. Solute diffusivity and the liquid phase impedance factor. Soil Sci. 172, 741–750.

Mualem, Y., Friedman, S.P., 1991. Theoretical prediction of electrical conductivity in saturated and unsaturated soil. Water Resour. Res. 27, 2771–2777.

Olesen, T., Moldrup, P., Gamst, J., 1999. Solute diffusion and adsorption in six soils along a soil texture gradient. Soil Sci. Soc. Am. J. 63, 519–524.

Reardon, E.J., Moddle, P.M., 1985. Gas diffusion coefficient measurements on uranium mill tailings: implications to cover layer design. Uranium 2, 111–131.

Revil, A., Cathles, L.M., 1999. Permeability of shaly sands. Water Resour. Res. 35, 651–662.

Revil, A., Jougnot, D., 2008. Diffusion of ions in unsaturated porous materials. J. Colloid Interface Sci. 319, 226–235.

Salem, H.S., Chilingarian, G. V, 1999. The cementation factor of Archie's equation for shaly sandstone reservoirs. J. Pet. Sci. Eng. 23, 83–93.

Savoye, S., Beaucaire, C., Fayette, A., Herbette, M., Coelho, D., 2012. Mobility of cesium through the callovo-oxfordian claystones under partially saturated conditions. Environ. Sci. Technol. 46, 2633–2641.

Savoye, S., Imbert, C., Fayette, A., Coelho, D., 2014. Experimental study on diffusion of tritiated water and anions under variable water-saturation and clay mineral content: comparison with the Callovo-Oxfordian claystones. Geol. Soc. London, Spec. Publ. 400, 579–588.

Savoye, S., Page, J., Puente, C., Imbert, C., Coelho, D., 2010. New experimental approach for studying diffusion through an intact and unsaturated medium: a case study with Callovo-Oxfordian argillite. Environ. Sci. Technol. 44, 3698–3704.

Sen, P.N., Scala, C., Cohen, M.H., 1981. A self-similar model for sedimentary rocks with application to the dielectric constant of fused glass beads. Geophysics 46, 781–795.

Thompson, A.H., Katz, A.J., Krohn, C.E., 1987. The microgeometry and transport properties of sedimentary rock. Adv. Phys. 36, 625–694.

Tidwell, V.C., Meigs, L.C., Christian-Frear, T., Boney, C.M., 2000. Effects of spatially heterogeneous porosity on matrix diffusion as investigated by X-ray absorption imaging. J. Contam. Hydrol. 42, 285–302.

Van Genuchten, M.T., 1980. A closed-form equation for predicting the hydraulic conductivity of unsaturated soils. Soil Sci. Soc. Am. J. 44, 892–898.

Van Loon, L.R., Glaus, M.A., Müller, W., 2007. Anion exclusion effects in compacted bentonites: towards a better understanding of anion diffusion. Appl. Geochemistry 22, 2536–2552.

Van Loon, L.R., Mibus, J., 2015. A modified version of Archie's law to estimate effective diffusion coefficients of radionuclides in argillaceous rocks and its application in safety analysis studies. Appl. Geochemistry 59, 85–94.

Van Loon, L.R., Soler, J.M., Bradbury, M.H., 2003a. Diffusion of HTO, 36 Cl- and 125 I- in Opalinus Clay samples from Mont Terri: effect of confining pressure. J. Contam. Hydrol. 61, 73–83.

Van Loon, L.R., Soler, J.M., Jakob, A., Bradbury, M.H., 2003b. Effect of confining pressure on the diffusion of HTO, 36 Cl- and 125 I- in a layered argillaceous rock (Opalinus Clay): diffusion perpendicular to the fabric. Appl. Geochemistry 18, 1653–1662.

Xiang, Y., Al, T., Scott, L., Loomer, D., 2013. Diffusive anisotropy in low-permeability Ordovician sedimentary rocks from the Michigan Basin in southwest Ontario. J. Contam. Hydrol. 155, 31–45.

Chapter 4: Conclusions

This study successfully demonstrated a method to generate partial gas saturation in low-permeability shale with hypersaline porewater. The data indicate that small-scale heterogeneity in the porosity leads to similar variations in partial gas saturation. X-ray radiography was used to measure the change in $S_{g\text{-}I}$ in the iodide-accessible pore fraction in low permeability shale. Results are consistent with the expectation that an increase in partial gas saturation causes a decrease in D_e for aqueous solutes. The results indicate that τ_f is sensitive to partial saturation. When evaluating results in terms of Archie's 2nd law, the data indicate values for the *n* exponent ranging from 2.8 to 5.7, but more data are required over a greater range of gas saturations in order to better understand the value of this empirical approach. The high salinity of the natural porewater precludes the use of dewatering techniques, and the gas-ingrowth method presented in this paper is limited by the low permeability of the rocks such that N_2 losses by diffusion are significant before bubble growth can expel pore fluid. The gas ingrowth method is therefore prone to higher degrees of gas saturation at the ends of the sample. Future work will focus on samples with shorter length dimensions in an attempt to achieve higher, and more uniform gas distributions.

4.2 Future Recommendations

While the results of this study successfully demonstrate a promising approach to study diffusion in multiphase fluid systems. It also demonstrates the challenges, working with high salinity brines, long preparation and experimental times dictated by the diffusion properties of the rocks, and low SNR due to the low porosity of the Michigan basin shales.

The following are suggestions for future research directions:

a) Collection of larger data sets, which can be used to compare with known empirical relationships and unsaturated diffusion models. This will help identify the approaches necessary to account for gas saturation in formation scale site characterization models.
b) Improvements to SNR with use of new techniques and detectors.
c) When generating gas saturation, higher pressures are needed to overcome capillary effects in the Queenston shale. Results in this study were limited to 1000 psi by equipment, but pressures as high as 3000 psi may be needed to achieve significant gas ingrowth. Use of shorter sample lengths may also help achieve higher partial gas ingrowth and create more uniform gas distribution profiles.
d) Comparison with dewatering techniques will help identify limitations to each of the methods and may help identify effects of gas distributions on diffusion.
e) Numerical modeling of gas generation profiles may provide additional insight in the small-scale processes effecting gas ingrowth in samples including gas distributions.

Appendix A: Sandstone Samples

A.1 Introduction

Results of site-characterization studies at the Bruce nuclear site suggest that porewater saturation may be less then 100% in Ordovician shale cap rock. Due to the low-permeability nature of the shale, initial method development experiments where preformed on both homogenous and heterogenous sandstone samples. The purpose of this portion of the study is to:

- Identify limitations to the gas exsolution method.
- Understand the gas distributions that can be expected in samples.
- Analyze the effect of a gas phase on D_e using the method.

A.2 Methods

A.2.1 Sample Descriptions

A.2.1.1 Carbon Tan Sandstone (Homogenous)

The Carbon Tan sandstone was chosen for this study based on its homogenous mineralogical and physical properties and was ordered through Kocurek Industries. Physical and mineral properties of the sandstones can be found in Table A.1.

Table A. 1 *Properties of Carbon Tan sandstone including porosity and mineralogy.*

[a]Mineralogy (wt %)	
Quartz	64
calcite	10
dolomite	11
k-spar	15
albite	
smectite (dioctohedral)	
chlorite	
illite	
kaolinite	
pyrite	

Hematite	
[a]**Porosity ϕ_w**	12.8
[a]Loomer et al (2013)	

A.2.1.2 Edmonton Group Sandstone (Heterogenous)

A bioturbated sandstone form the Edmonton Group was chosen for preliminary testing based on its heterogenous properties. The sample is composed of fine to medium grained sand which is made up of quartz (55%), plagioclase (25%) and rock fragments which consist mostly of chert (15–20%). The grains are cemented weakly with calcite and siderite cement (Gingras et al., 2002). The sample is pervasively Macaronichnus-burrowed, to the degree that original lamination of the rock is no longer evident (Gingras et al 2002). The burrows are around 1.4 mm in diameter and are sinuous to meandering and unbranched (Gingras et al., 2002). The burrows are generally parallel to the bedding and ramp gently upward or downward in different directions (Gingras et al., 2002). Porosity of the sandstone was estimated with petrographic thin section by Gingras et al. (2002) indicating values from 12.1–14.4 % in burrowed portions of the sandstone and 10.6–13.9 % in unburrowed sections.

A.2.2 Measurements of Diffusion coefficients and porosity

A.2.2.1 Sample preparation and acquisition parameters

Samples were prepared using a diamond coring bit to drill sample cores. The samples (20 mm diameter and 20 to 23 mm length) were drilled normal to bedding, using water to cool the bit. Samples where initially flushed with CO_2 gas for 4 hours, followed by forcing a sandstone synthetic porewater (S-SPW) (Table A.2.) through the sample with a syringe. The samples where left immersed in S-SPW under vacuum for two weeks prior to the start of experiments to ensure full saturation. Samples were mounted in a diffusion cell (Fig. 2.1.) that

was specifically designed to prevent expansion of the sample under the increased internal gas pressures.

Table A. 2 *Composition of S-SPW and iodide tracer solution (S-SPW-T) used in diffusion experiments.*

Element	S-SPW mol/kgw	S-SPW-T mol/kgw
Na	0.00	0.00
K	1.00	1.00
Ca	0.00	0.00
Mg	0.00	0.00
Cl	1.00	0.00
Br	0.00	0.00
Sr	0.00	0.00
I	0.00	1.00

Porosity, gas saturation and measurements were conducted using the X-ray radiography and computed tomography technique's described in Appendix D based on Cave et al. (2009) and Agbogun et al. (2013a,b). X-ray radiography measurements were conducted with an X-ray CT system (Pinnacle X-ray Systems, Atlanta, Georgia) equipped with a Varian® NDI-160/22 source coupled to a Gulmay® CPL series (CP2-1402) 3000 W generator and a Varian PaxScan®1313DX amorphous-silicon flat-panel imaging detector. Computed tomography data sets where collected with the same X-ray CT system (Pinnacle X-ray Systems, Atlanta, Georgia) equipped with a second, microfocus X-ray source (Hamamatsu L12161-07). All data were collected as 16-bit tiff image files and acquisition parameters for radiography and computed tomography can be found in Table (A.3).

Table A. 3 *Acquisition parameters for radiography and computed tomography in sandstone experiments.*

Radiography					
Sample	**kV**	**mA**	**filtration (mm) Al**	**Exposure time (s)**	**Frame Averages**
Carbon Tan	50	60	3.3	0.33	32
Edmonton Group	50	60	3.3	0.33	32
Computed Tomography					
Sample	**kV**	**µA**	**filtration (mm) Al**	**Exposure time (s)**	**Frame Averages**
Carbon Tan	60	250	3.3	5	8
Edmonton Group	60	250	3.3	5	8

A.2.2.2 Radiography

Initial radiography and computed tomography measurements where collected prior to the start of diffusion experiments, the fluid reservoirs at the top and bottom of the diffusion cell (Fig. 2.1) were filled with S-SPW solution. Experiments were initiated by replacing S-SPW in the lower reservoir with I^- tracer solution (S-SPW-T), prepared from the S-SPW by substituting KCl with KI (Table A.2). The lower reservoir was chosen to ensure the higher-density solution was at the bottom, thereby limiting density-driven mixing between the two solutions. Reference images (radiographs) were collected immediately after tracer solution was added to the reservoir and time-series images were collected over 24 hours. All radiographs were collected with identical sample positioning and instrumental operating conditions. In all cases, pixel grey values from the radiograph images were converted to one-dimensional profiles that represent X-ray attenuation coefficients (μ) according to the method described by Cavé et al. (2009). Diffusion was monitored in this way until tracer breakthrough occurred at the top

boundary. The samples were then saturated with the I^- tracer solution by allowing in-diffusion from both ends. The influx of tracer was monitored by X-ray radiography over a period of 10 days until no further change in X-ray attenuation was observed. At this point, one-dimensional profiles of ϕ were obtained following the method described in a modification of the Cavé et al. (2009) approach as described in Appendix D.

A.2.2.3 Computed Tomography

Three-dimensional computed tomography scans were acquired to evaluate porosity and tracer concentration distributions throughout the sample following the calibrated approach described by Agbogun et al. (2013a,b). The 3-D CT image sets were collected before the diffusion experiments and after the samples were saturated with iodide solution. Projection image sets were reconstructed with NRECON-V1.7.1.0 (Bruker MicroCT), creating stacks of 2-D slices representing the full 3-D volume of each sample. The final CT datasets (iodide saturated) were digitally registered to the initial datasets using the Manual Seed Registration code (Williamson, 2009). The registrations were conducted using the coordinate positions of high attenuating fiduciary points in the sample. Details of the CT data are based on the approach developed by Agbogun et al. (2013a,b) processing as presented in Appendix D.2.

A.2.3 Gas generation

The fully tracer-saturated samples were subjected to partial gas generation with an approach that uses N_2 gas and takes advantage of the variability of N_2 solubility versus pressure that is described in further detail in section 2.3 of Chapter 2. The solubility of N_2 was recalculated using the model reported by Mao and Duan (2006) for the S–SPW. Pressures and predicted gas saturations can be found in Table (A.4). Although it is expected that the volume

of gas phase created in the pore spaces will be lower than that predicted by Equation [2.5] in Chapter 2 due to capillarity effects. X-ray radiography is therefore employed to quantify the final degree of N_2 saturation.

As a first step toward inducing partial gas saturation, the diffusion cells, with end caps removed, were immersed for 8-10 days in I^- tracer solution inside a pressure vessel with elevated $N_{2(g)}$ pressures in the head space Table (A.4). The high N_2 gas pressure causes an increase in N_2 solubility, allowing for diffusion of elevated aqueous N_2 concentrations throughout the pore space of the rock. Based on the D_p values determined for I^- by in-diffusion, the time period of 8–10 days was considered sufficient to achieve 93%–99% of the fully-equilibrated N_2 distribution in the sample. In the second step, the $N_{2(g)}$ overpressure in the head space is decreased to 1 atm which initiates nucleation and growth of $N_{2(g)}$ bubbles in the pore spaces, forcing tracer solution out of the sample. The evolution of partial gas saturation was monitored by X-ray radiography, and 24 hours was sufficient for equilibration of the gas and brine saturation states. After equilibration, one-dimensional profiles of μ were collected again, and the ratio between these, and the profiles collected previously from the fully tracer-saturated samples were used to determine the fraction of gas saturation. X-ray radiography and 3-D CT projection image sets were collected with gas growth using different pressures applied to the same samples (Table A.4).

Table A. 4 *Experimental pressures and predicted % gas saturations.*

Carbon Tan	P_1 (PSI)	P_2 (PSI)	[a]Predicted % gas saturation
A	100	14.6	0.07
B	250	14.6	0.19
C	450	14.6	0.35
D	650	14.6	0.51
Edmonton Group	**P_1 (PSI)**	**P_2 (PSI)**	**[a]Predicted % gas saturation**
A	100	14.6	0.07

[a]Calculated with Equation (2.3) in Chapter 2.

Out-diffusion experiments were conducted on the Carbon Tan sandstone following gas generation with 100 psi and 250 psi initial gas pressures. The experiments were initiated by adding S-SPW (no tracer) to the reservoir and monitoring the diffusion of iodide outward from the porewater to the reservoir. To eliminate density effects, the cell was upended to maintain the higher-density solution at the bottom boundary. Radiographs were collected in time series using similar time increments as for in-diffusion experiments.

A.3 Results

A.3.1 Porosity

A.3.1.1 Carbon Tan Sandstone

Results collected by X-ray radiography indicate minor fluctuations in porosity (Fig. A.1), that likely correspond to bedding changes. Average ϕ values derived from the 1-D profiles for tracer-saturated samples are 0.127 (12.7%) (Table A.5), indicating that ϕ is approximately equal to the total accessible porosity (represented by ϕ_w) reported by Loomer et al. (2013) (Table

A.1). Computed tomography reconstruction images of the Carbon Tan sandstone visually some variations in porosity throughout the sample (Fig. A.2). X-ray CT can be used to provide a quantitative analysis of the porosity distribution within a sample and indicate that the Carbon Tan sandstone displays a narrow pore distribution, indicative of a more homogenous material (Fig. A.3).

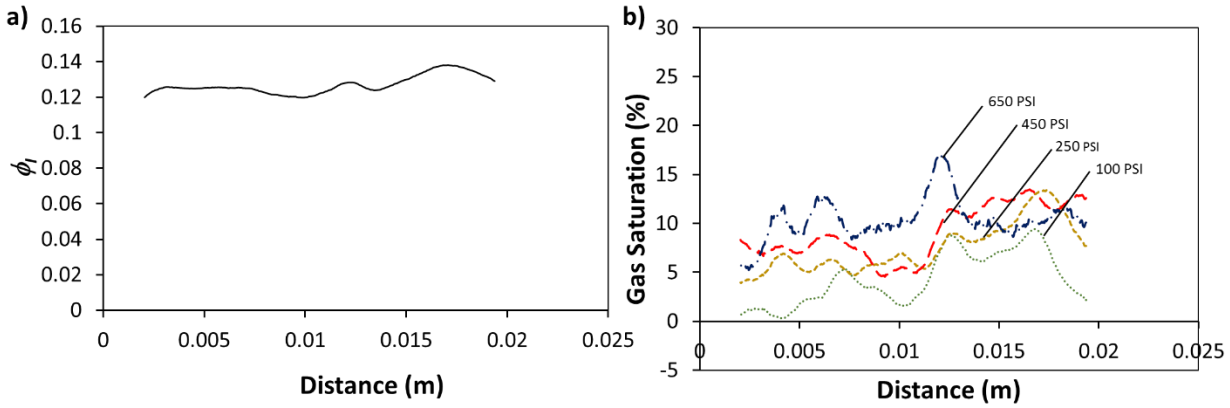

Fig. A. 1 *Profiles for the spatial distribution of a) ϕ_I and b) gas saturation ($S_{g\text{-}I}$) in Carbon Tan sandstone.*

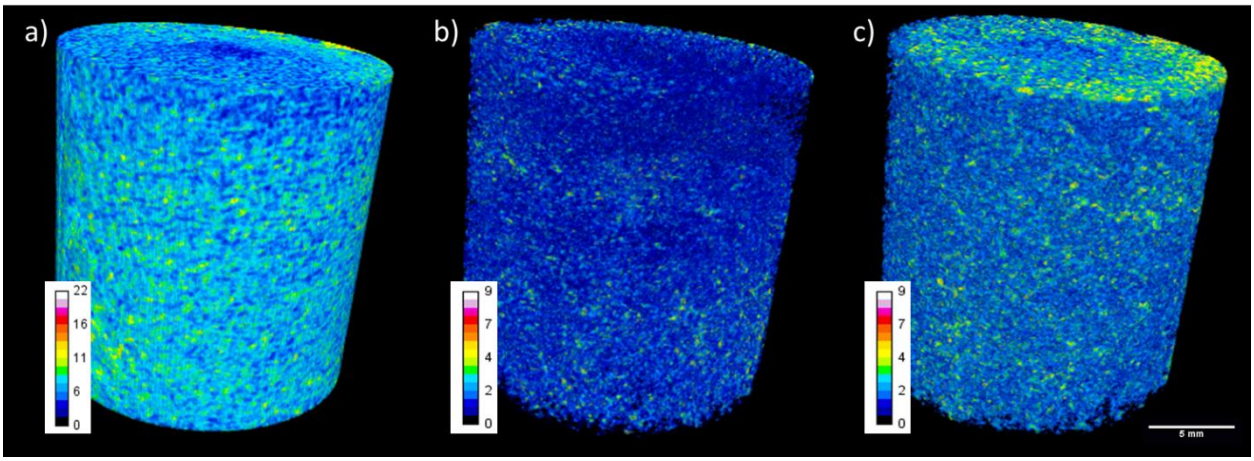

Fig. A. 2 *3-D computed tomographic images of Carbon Tan sandstone showing a) saturated porosity, b) gas-filled porosity after generation at 250 PSI and c) gas-filled porosity after generation at 650 PSI.*

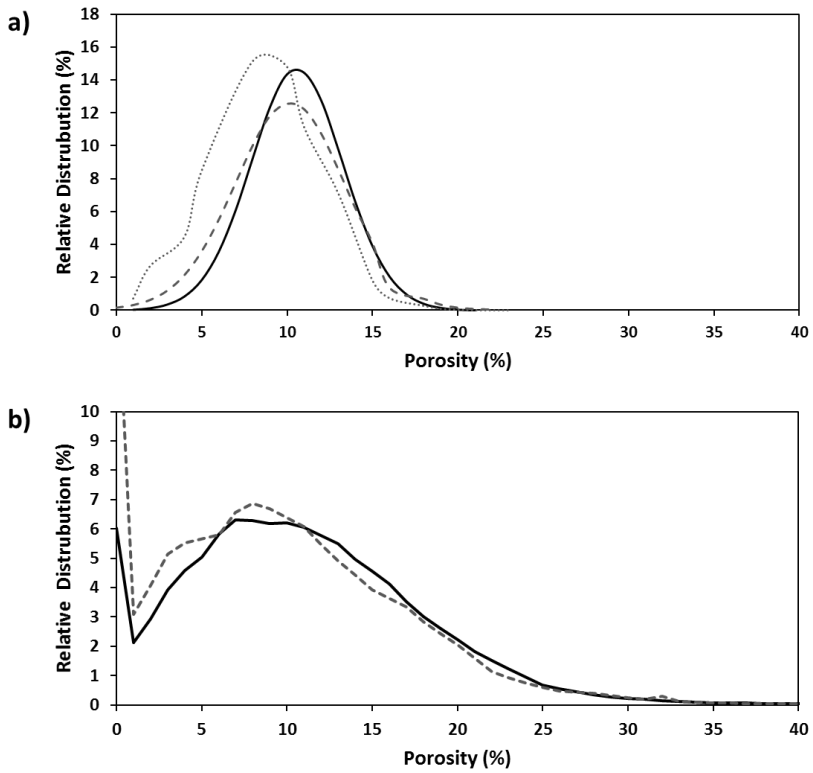

Fig. A. 3 *Porosity distribution measured by 3-D CT images for a) Carbon Tan sandstone and b) Edmonton Group sandstone.*

Table A. 5 *Comparison of sample average results for Carbon Tan sandstone from in-diffusion measurements on fully saturated samples to out-diffusion measurements on partially saturated (PS) samples.*

Sample	Carbon Tan	Carbon Tan – A (100psi)	Carbon Tan – B (200psi)	Carbon Tan – C (450psi)	Carbon Tan – D (650psi)
Average Iodide accessible porosity (ϕ_1)	0.127	0.121	0.117	0.115	0.113
% Gas Sat[a]	–	4.1	7.5	9.1	10.4
D_p (m^2/s)	$2.7x10^{-10}$± $8.3x10^{-12}$	$2.2x10^{-10}$± $5.0x10^{-11}$	$2.3x10^{-10}$± $4.1x10^{-11}$	–	–
	–	16.7	13.2	–	–
D_e (m^2/s)	$3.4x10^{-11}$± $1.1x10^{-12}$	$2.7x10^{-11}$ ± [$6.1x10^{-12}$]	$2.7x10^{-11}$ ± [$4.8x10^{-12}$]	–	–
	–	21.1	20.7	–	–

A.3.1.2 Edmonton Group Sandstone

Results from X-ray radiography indicate fluctuations in porosity that likely relate to the bioturbation and bedding variations in the sample. An average ϕ_I value of 8.9% was derived from the 1-D profiles for tracer-saturated samples (Fig. A.4) (Table A.6), and the profiles did not show extreme heterogeneity, consistent with the small differences in porosity between zones with and without bioturbation reported by Gingras et al. (2002). However, computed tomography reconstruction indicates areas of the sample with significantly higher porosity that likely correspond to areas of pervasive bioturbation features (Fig. A.5). X-ray CT derived porosity distribution curves for the Edmonton group sandstone displays a wide porosity range indicative of a more heterogeneous pore space.

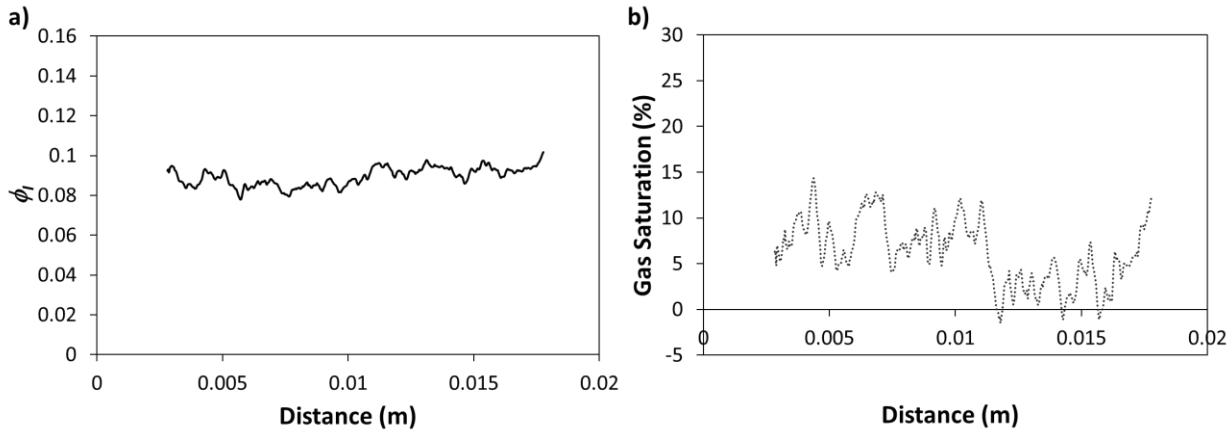

Fig. A. 4 *Profiles for the spatial distribution of a) ϕ_I and b) gas saturation ($S_{g\text{-}I}$) at 100 PSI in the Edmonton Group sandstone.*

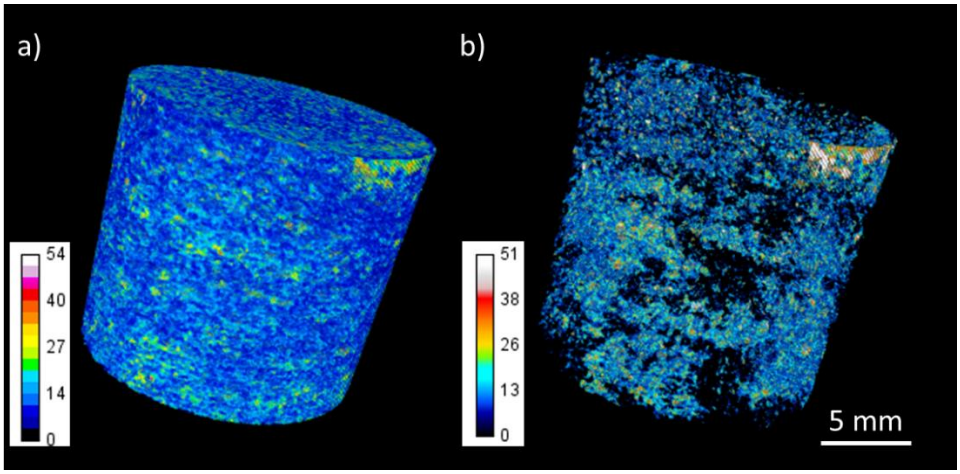

Fig. A. 5 *3-D computed tomographic images of Edmonton Group sandstone showing a) saturated porosity (%) and b) gas-filled porosity (%) after generation at 100 PSI.*

Table A. 6 *Comparison of sample average results for Edmonton Group sandstone measured by X-ray radiography.*

Sample	Edmonton Group	Edmonton Group (100psi)
Average Iodide accessible porosity (ϕ_I)	0.089	0.084
% Gas Sat[a]	–	6.3

A.3.2 Connectivity Analysis

Connectivity is a challenging thing to assess quantitatively, a Eular characterization can be used with 3-D CT images to provide a semi-quantitative indication of the connectivity of a porous media (Aboufoul et al., 2017; Ahmad, 2016; Katuwal et al., 2015; Toriwaki et al., 2002; Yio et al., 2016). Typically, this approach requires imaging resolutions high enough for pore-scale imaging with limited partial volume effects. In this study we use a REV approach and do not have pore-scale resolution to do a proper analysis of the connected pore space. Alternatively, we propose to evaluate the connectivity of higher porosity regions within a

sample by a porosity thresholding approach. This approach provides a semi-quantitative approach to evaluate connectivity in higher porosity regions.

The porosity above a given threshold value is binarized and the connectivity of the pore space above the threshold porosity can be analyzed. The connectivity analysis by Eular characterization was performed with use of the ImageJ plugin BoneJ (Doube et al., 2012; Toriwaki et al., 2002).

The connectivity of the Carbon Tan sandstone indicates that above a 10% threshold porosity the pore space begins to become disconnected and above a 14% threshold the porosity is no longer well connected (Fig. A.6). Analysis of connectivity for the Edmonton Group sandstone indicates that the pore space starts losing connectivity above a 10% threshold and by 22% the majority of the pore space is disconnected (Fig. A.6).

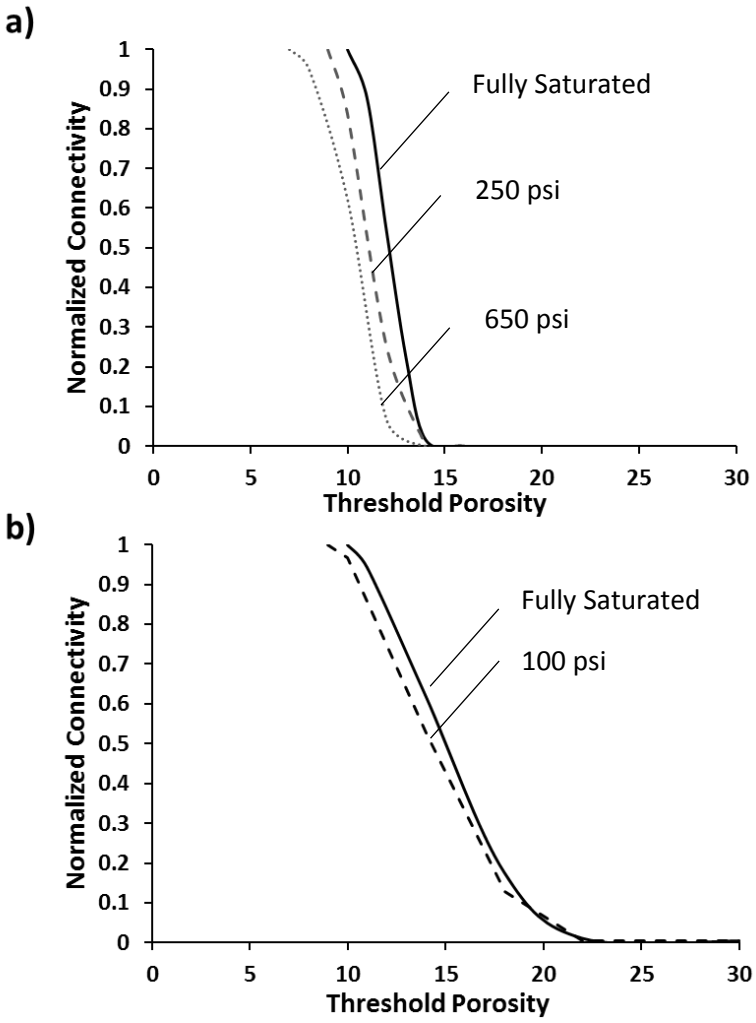

Fig. A. 6 *Eular characterization of porosity connectivity for various porosity threshold values in 3-D CT image datasets for a) Carbon Tan sandstone and b) Edmonton Group sandstone.*

A.3.3 Partial gas generation

A.3.3.1 Carbon Tan Sandstone

One-dimensional partial gas profiles were measured for the Carbon Tan sandstone, and as expected, gas saturation values are much lower than those predicted by Equation 2.5 (Table A.4.). There is a trend of increased gas saturation with increased N_2 pressure, although this trend is nonlinear and indicates that there is a limit to partial gas growth with this method (Fig. A.7). In 1-D partial gas profiles, areas of higher porosity generally display higher gas ingrowth,

and these areas are common to profiles for all initial pressures (Fig. A.1). Reconstructed 3-D computed tomography images (Fig. A.2, Fig. A.8 and Fig. A.9) also indicate that zones with higher gas growth correspond to areas with relatively high porosity. It is important to note that not all areas of higher porosity see significant gas growth (Fig. A.3) and when comparing 3-D CT slices between 250PSI and 650PSI we see gas growth in similar regions in sample, although at 250PSI we see less gas growth in the center of the sample (Fig. A.8 and Fig. A.9). This may be indicative higher pressures needed to overcome capillary effects within the center of the sample. The majority of the gas growth occurs in regions of the sample where porosity ranges from 10-14% (Fig. A.3) and this corresponds to the highest connectivity regions of the sample (Fig. A.6).

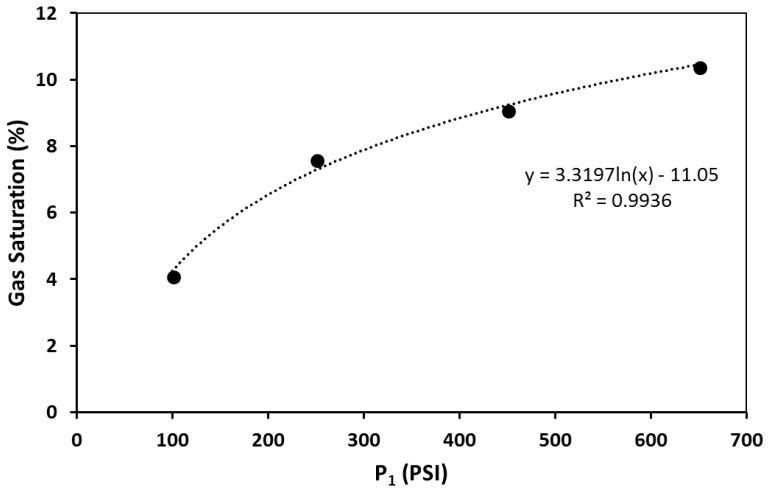

Fig. A. 7 *Showing logarithmic trend of gas saturation with P1 pressure.*

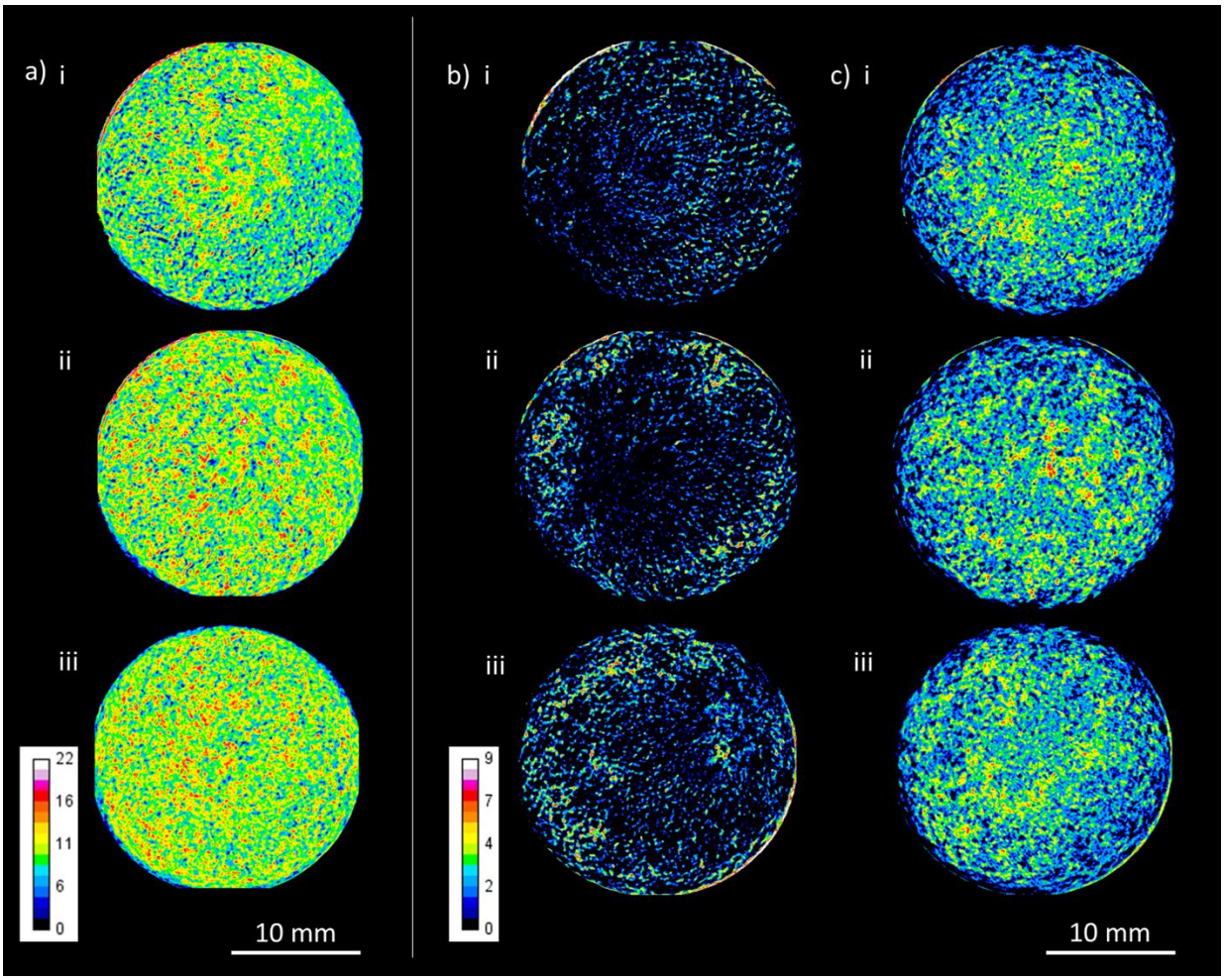

Fig. A. 8 *3-D computed tomographic x-y slices of Carbon Tan sandstone a) water-saturated porosity (%), b) gas-filled porosity (%) after generation at 250 PSI, and c) gas-filled porosity (%) after generation at 650 PSI. Taken at different positions in the sample i) 0.24 cm ii) 0.64 cm and iii) 1.66 cm from the base of sample.*

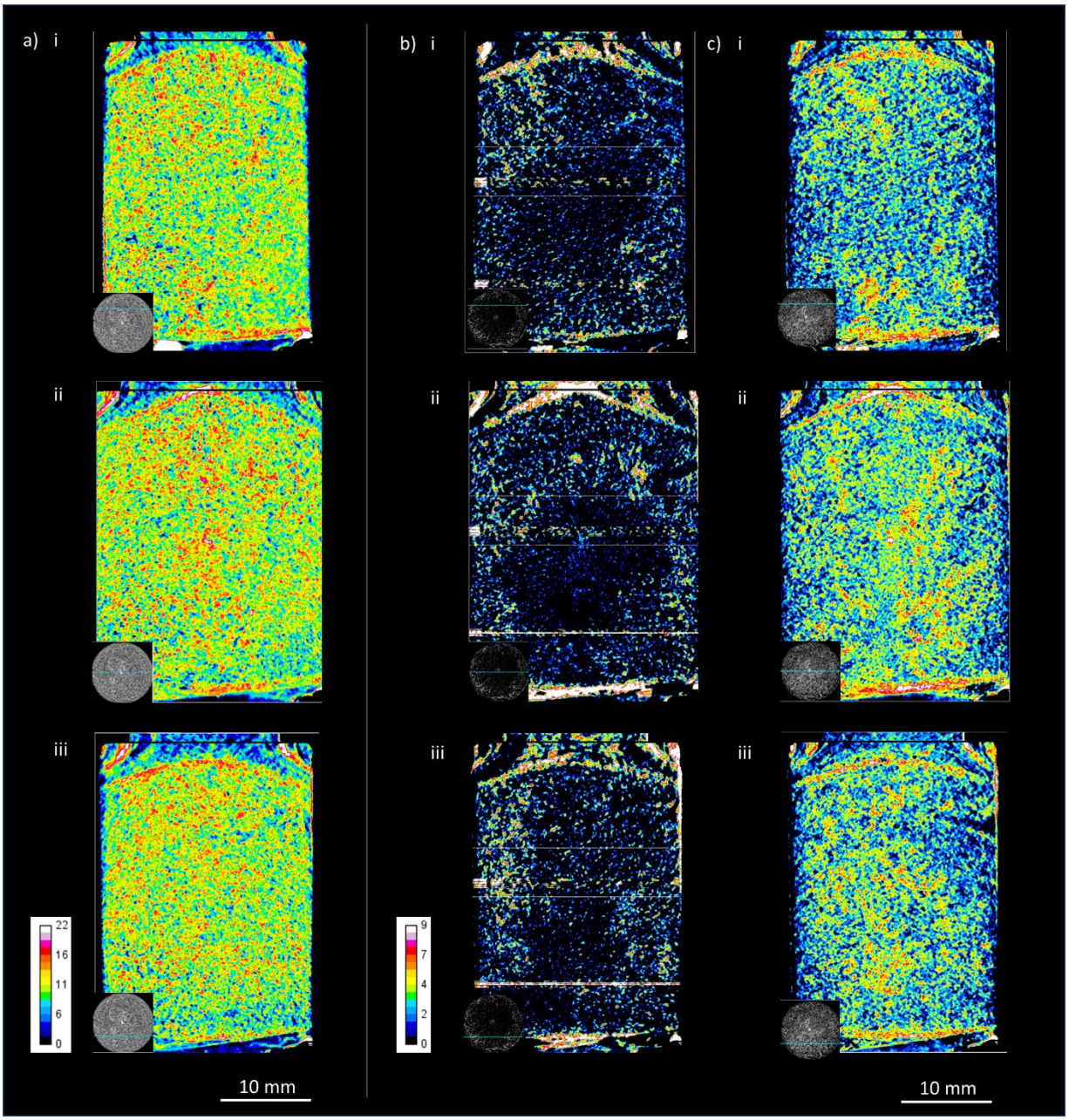

Fig. A. 9 *3-D computed tomographic x-z slices of Carbon Tan sandstone a) water-saturated porosity (%), b) gas-filled porosity (%) after generation at 250 PSI, and c) gas-filled porosity (%) after generation at 650 PSI. Taken at different positions in the sample i) 0.4 cm ii) 1.0 cm and iii) 1.6 cm from the front of sample.*

A.3.3.2 Edmonton Group sandstone

One dimensional partial gas profiles where collected and compared for the Edmonton group sandstone (Fig. A.4); gas saturation values are close to those predicted by Equation 2.5 in

Chapter 2.3 (Table A.6). Reconstructed 3-D computed tomography images (Fig. A.10 and Fig. A.11) show that most, but not all, areas of higher gas growth generally correspond to areas with higher porosity. In 3-D computed tomography images we can see that gas growth occurs in separate clusters that form in areas of higher porosity and grow to become connected. In some of these areas we see nearly 100% gas saturation, which is significantly higher than predicted by equation 2.5 in chapter 2.3. The build up of gas generally seems to occur near the edges of the sample similar and may indicate that higher pressures are needed to overcome capillary effects at the centre of the sample (Fig. A.10 and Fig. A.11). The majority of the gas growth in the sample occurs in regions where the porosity ranges from 10-17% (Fig. A.3), corresponding to the highest connected porosity regions of the sample (Fig. A.6).

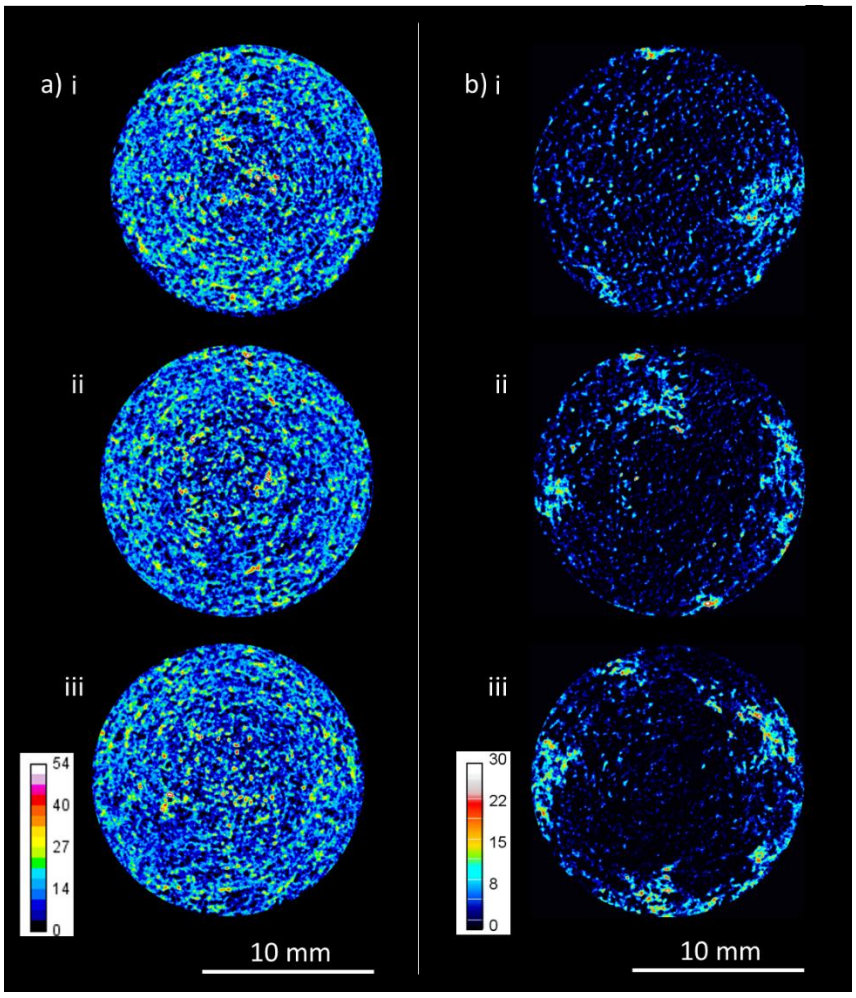

Fig. A. 10 *3-D computed tomographic x-y slices images of Edmonton Group sandstone a) water-saturated porosity (%), b) gas-filled porosity (%) after generation at 100 PSI, and c) percent gas-filled porosity (%) after generation at 100 PSI. Taken at different positions in the sample i) 0.85 cm ii) 0.62 cm and iii) 0.29cm from the base of sample.*

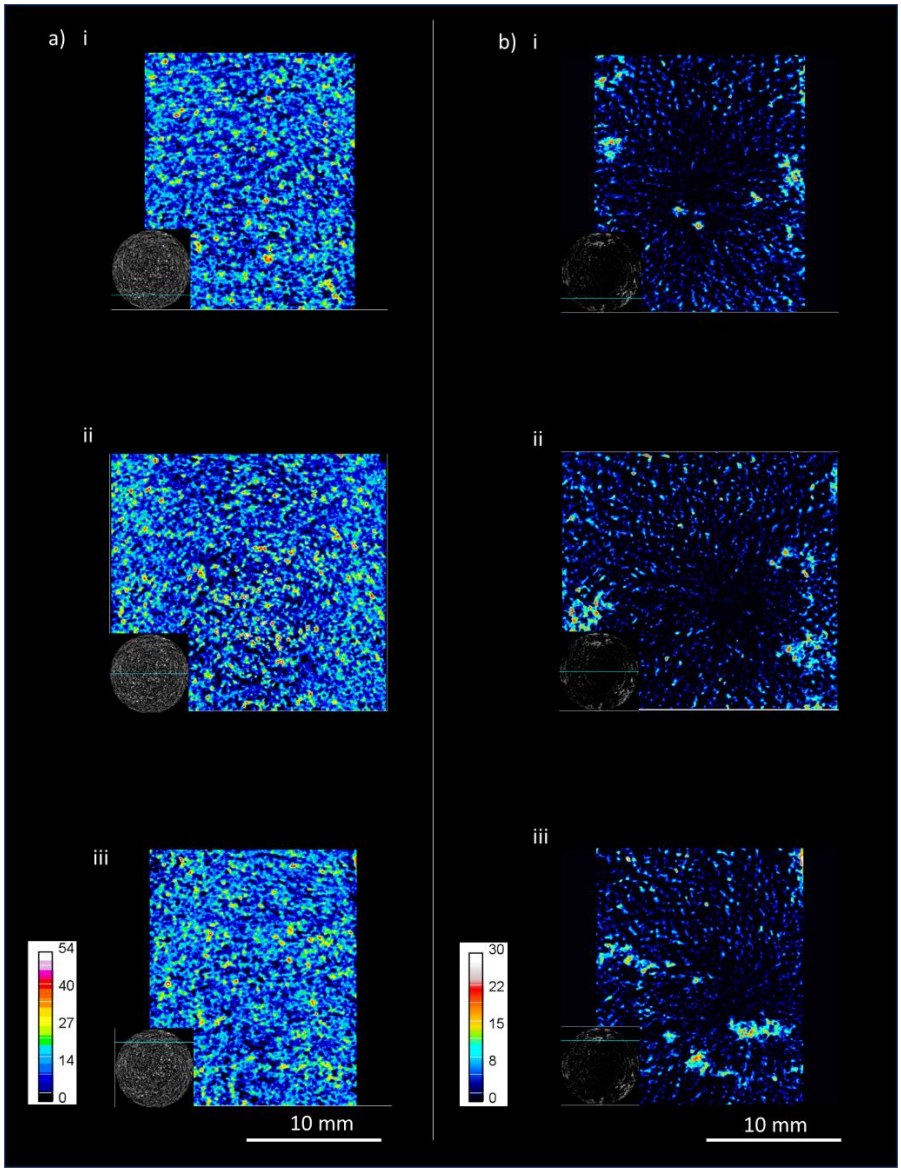

Fig. A. 11 3-D computed tomographic x-z slices images of Edmonton Group sandstone a) water-saturated porosity (%), b) gas-filled porosity (%) after generation at 100 PSI, and c) percent gas-filled porosity (%) after generation at 100 PSI. Taken at different *positions in the sample i) 0.3 cm ii) 1.0 cm and iii) 1.7 cm from front of sample.*

A.3.4 Diffusion

A.3.4.1 Carbon Tan

The time-series profiles for relative tracer concentrations (C/C_0) in the porewater-saturated Carbon Tan sample are shown in Fig. A.12. The average D_{e-l} values derived from fitting the experimental data to the analytical model are 2.7 x 10^{-11} m^2/s for the Carbon Tan

sandstone (Table A.5) with a relative standard deviation of 1.1×10^{-12} m^2/s (presented as 1 σ in Table A.5). Ingrowth of 4 % gas in the carbon tan sandstone resulted in decrease in D_e by 21.7% and an ingrowth of 7% resulted in a decrease in 20.7%. The decrease in D_e is partially accounted for by the loss of iodide-accessible porosity, but a decrease in τ_f (decreased δ and/or increased τ) is primarily responsible for the decrease in D_e. It is interesting that the decrease of around 20% at 250 psi is similar to the loss of connectivity of higher porosity regions of the sample by 16% (Fig.A.6).

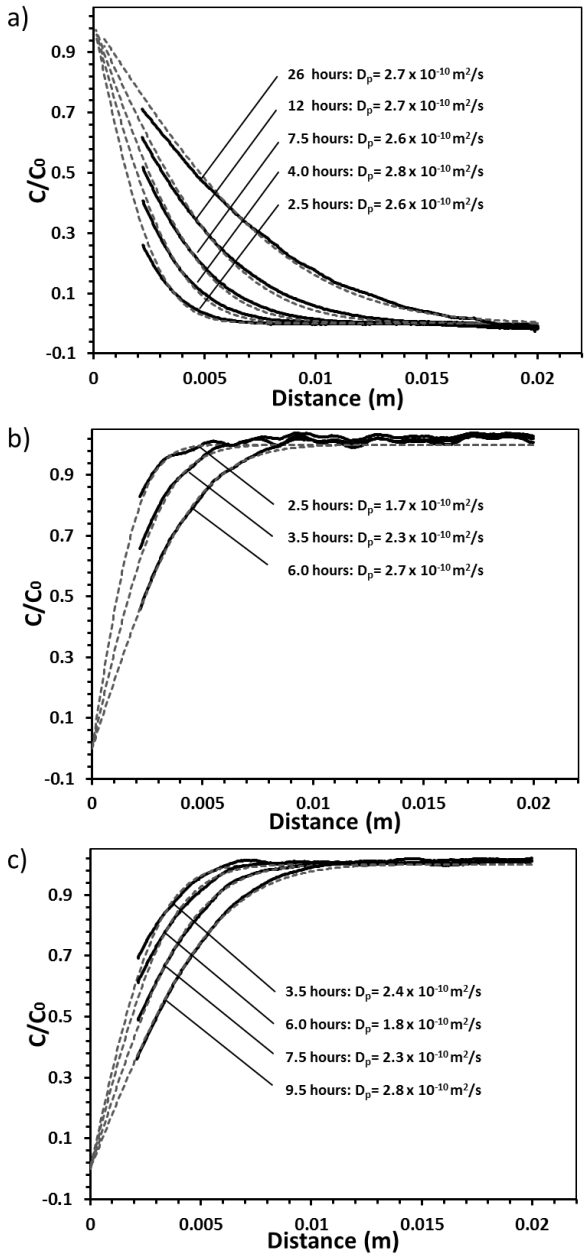

Fig. A. 12 *One-dimensional, time-series diffusion profiles for relative iodide concentration (C/C_0) in Carbon Tan sandstone: a) in-diffusion experiment with 0 % gas saturation, b) out-diffusion experiment with 4.1 % gas saturation and c) out-diffusion experiment 7.5 % gas saturation.*

A.4 Discussion

A.4.1 Gas Generation

In 1-D gas distribution profiles for the Carbon Tan we observe preferential gas growth in areas of higher porosity while for the Edmonton group there is no clear correlation. Repeat

measurements on the Carbon Tan sandstone indicate limitations in the method's ability to generate gas, with decreasing amount of gas generated with increasing initial pressures from 250-650 PSI (Fig. A.5). The upper limit on gas saturation versus pressure likely corresponds the critical gas salutation, which limits gas growth to the amount of gas needed for bulk gas flow (Firoozabadi et al., 1992). Typically critical gas is measured by depressurization of waterflooded cores (Petersen et al., 2004) or solution gas drive experiments (Bondino et al., 2007).

3-D computed tomography data for the Carbon Tan and Edmonton Group sandstones clearly show that gas growth occurs preferentially in higher porosity areas of the sample, above 10% but does directly correlate with high porosity, indicating that porosity is a governing factor but other factors such as connectivity may also be important. Areas of gas growth in the samples achieve significantly higher gas saturations than predicted in Table A.4; likely a result of diffusive transport of N_2 from areas with limited gas growth.

A.4.2 Diffusion in unsaturated media

Archie's 2nd law has commonly been used to describe diffusion and electrical conduction in variably saturated porous media (Archie, 1942; Hamamoto et al., 2009; Hamamoto et al., 2010; Marshall, 1959; Mualem and Friedmen, 1991; Savoye et al., 2010, 2012, 2014). According to Hamamoto et al. (2010), Archie's 2nd law can be described by Equations [3.5] and [3.6].

A similar approach as in section x.x to evaluating the carbon Tan sandstone with Archie's law was used. The following assumptions were made of the assumptions that $\phi_{th} = \phi_{th}^*$ *and that* ϕ_{th}^* is equal to the anion inaccessible porosity. Sandstones are not prone to anion exclusion thus the $\phi_{th}^*=0$. We then compare results with the two assumptions that $\phi_{th} = \phi_{th}^*$ and $n=2$.

The cementation exponent (*m*) was found to be 1.95 and with the assumption $\phi_{th} = \phi_{th}$* a saturation exponent (*n*) of 2.8–4.7 was found to be a good fit to the data (Fig. A.13) (Table A.7). Under the assumption that *n=2* a percolation ϕ_{th} threshold of 0.035–0.075 was found to be a good fit to the data. Both approaches indicate that the gas generation is occurring in the areas of the sample most responsible for transport.

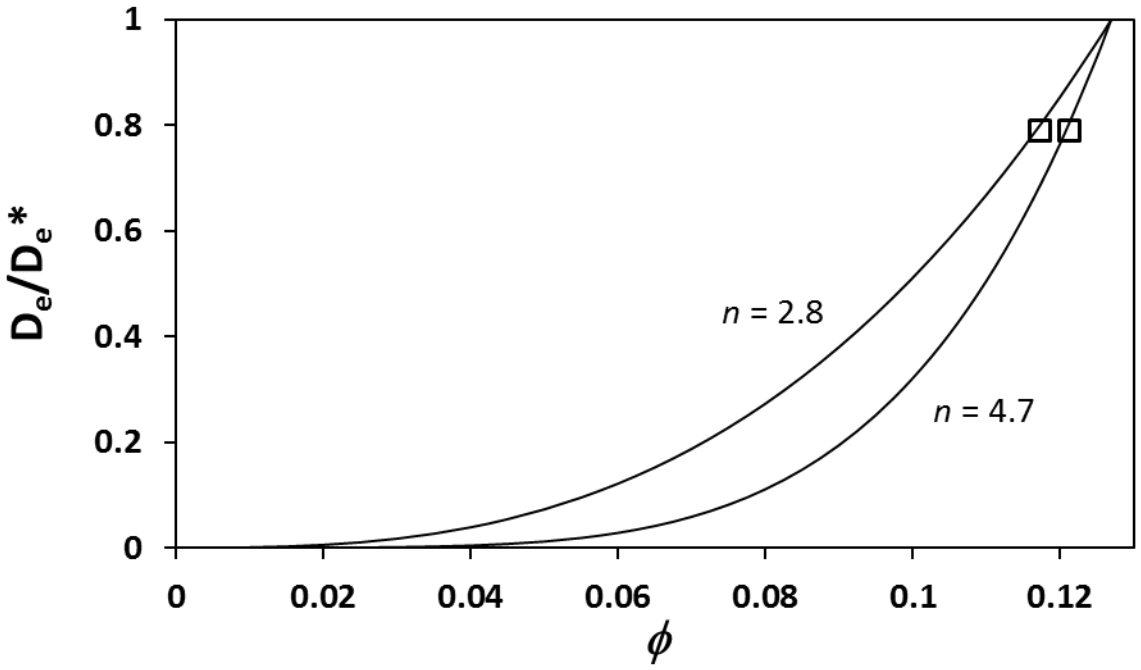

Fig. A. 13 *Illustration based on Equation 3.6 in Chapter 3 to show variation in the iodide effective diffusion coefficient as a function of the water-filled porosity. Parameters are from Table 3.2. The square symbols represent measurements conducted in this study.*

Table A. 7 *List of parameters used to estimate the range of values for n and ϕ_{th} with Equation 3.6.*

	Estimate Values for *n*		Estimate Values for ϕ_{th}	
	Carbon Tan (100PSI)	Carbon Tan (250PSI)	Carbon Tan (100PSI)	Carbon Tan (250PSI)

Saturation exponent (*n*)	4.7	2.8	2	2
Percolation threshold (ϕ_{th})	0.0	0.0	0.072	0.035
Cementation exponent (*m*)	1.95	1.95	1.95	1.95
Inactive Fluid phase (ϕ_{th}*)	0.0	0.0	0.0	0.0
Water-accessible porosity (ϕ_w)	0.127	0.127	0.127	0.127

A.5 Conclusions

This study successfully demonstrated a method to generate partial gas saturation and provide reliable measurements of the partial gas created. The technique allows for repeat measurements to be made on the same sample. The method shows that gas growth occurs in higher porosity regions within a sample and connectivity plays an important role in diffusive transport. The ability of the method to generate high degrees of gas saturation may be limited by the critical gas saturation, corresponding to the gas saturation at which bulk gas flow occurs.

X-ray radiography was used to measure the change in gas saturation and corresponding diffusion properties. Results are consistent with the expectation that an increase in partial gas saturation causes a decrease in D_e for aqueous solutes. More data are required from a wider range of gas saturations to allow for a proper comparison with Archie's laws.

A.6 References

Agbogun, H.M.D., Al, T.A., Hussein, E.M.A., 2013a. Three dimensional imaging of porosity and tracer concentration distributions in a dolostone sample during diffusion experiments using X-ray micro-CT. J. Contam. Hydrol. 145, 44–53.

Agbogun, H.M.D., Hussein, E.M.A., Al, T.A., 2013b. Assessment of x-ray micro-CT measurements of porosity and solute concentration distributions during diffusion in porous geologic media. J. Porous Media 16, 683–694.

Ahmad, M.A., 2016. Quantifying relationships between X-ray imaged macropore structure and hydraulic conductivity.

Archie, G.E., others, 1942. The electrical resistivity log as an aid in determining some reservoir characteristics. Trans. AIME 146, 54–62.

Bondino, I., Long, J., McDougall, S.R., Hamon, G., others, 2007. A pore-scale network modeling study of gravitational effects during solution gas drive: Results from macroscale simulations, in: EUROPEC/EAGE Conference and Exhibition.

Cavé, L., Al, T., Xiang, Y., Vilks, P., 2009. A technique for estimating one-dimensional diffusion coefficients in low-permeability sedimentary rock using X-ray radiography: comparison with through-diffusion measurements. J. Contam. Hydrol. 103, 1–12.

Doube, M., K\losowski, M.M., Arganda-Carreras, I., Cordelières, F.P., Dougherty, R.P., Jackson, J.S., Schmid, B., Hutchinson, J.R., Shefelbine, S.J., 2010. BoneJ: free and extensible bone image analysis in ImageJ. Bone 47, 1076–1079.

Firoozabadi, A., Ottesen, B., Mikklesen, M., others, 1992. Measurements of Supersaturation and Critical Gas Saturation (includes associated papers 27920 and 28669). SPE Form. Eval. 7, 337–344.

Gingras, M.K., MacMillan, B., Balcom, B.J., Saunders, T., Pemberton, S.G., 2002. Using magnetic resonance imaging and petrographic techniques to understand the textural attributes and porosity distribution in Macaronichnus-burrowed sandstone. J. Sediment. Res. 72, 552–558.

Loomer, D., Xiang, Y., Al, T. Investigations of methods for quantifying the diffusion transport processes in sedimentary rock, NWMO-TR-2013-18. University of New Brunswick. Report prepared for the Nuclear Waste Management Organization NWMO. Report available online through http://www.nwmo.ca.

Hamamoto, S., Moldrup, P., Kawamoto, K., Komatsu, T., 2010. Excluded-volume expansion of Archie's law for gas and solute diffusivities and electrical and thermal conductivities in variably saturated porous media. Water Resour. Res. 46.

Hamamoto, S., Perera, M.S.A., Resurreccion, A., Kawamoto, K., Hasegawa, S., Komatsu, T., Moldrup, P., 2009. The solute diffusion coefficient in variably compacted, unsaturated volcanic ash soils. Vadose Zo. J. 8, 942–952.

Katuwal, S., Arthur, E., Tuller, M., Moldrup, P., de Jonge, L.W., 2015. Quantification of soil pore network complexity with X-ray computed tomography and gas transport measurements. Soil Sci. Soc. Am. J. 79, 1577–1589.

Mao, S., Duan, Z., 2006. A thermodynamic model for calculating nitrogen solubility, gas phase composition and density of the N2--H2O--NaCl system. Fluid Phase Equilib. 248, 103–114.

Marshall, D.J., Madden, T.R., 1959. Induced polarization, a study of its causes. Geophysics 24, 790–816.

Mualem, Y., Friedman, S.P., 1991. Theoretical prediction of electrical conductivity in saturated and unsaturated soil. Water Resour. Res. 27, 2771–2777.

Petersen, E.B., Agaev, G.S., Palatnik, B., Ringen, J.K., Øren, P.E., Vatne, K.O., 2004. Determination of critical gas saturation and relative permeabilities relevant to the depressurisation of the Statfjord field, in: SCA Symposium, Abu Dhabi. pp. 5–9.

Savoye, S., Beaucaire, C., Fayette, A., Herbette, M., Coelho, D., 2012. Mobility of cesium through the callovo-oxfordian claystones under partially saturated conditions. Environ. Sci. Technol. 46, 2633–2641.

Savoye, S., Imbert, C., Fayette, A., Coelho, D., 2014. Experimental study on diffusion of tritiated water and anions under variable water-saturation and clay mineral content: comparison with the Callovo-Oxfordian claystones. Geol. Soc. London, Spec. Publ. 400, 579–588.

Savoye, S., Page, J., Puente, C., Imbert, C., Coelho, D., 2010. New experimental approach for studying diffusion through an intact and unsaturated medium: a case study with Callovo-Oxfordian argillite. Environ. Sci. Technol. 44, 3698–3704.

Toriwaki, J., Yonekura, T., 2002. Euler number and connectivity indexes of a three dimensional digital picture. FORMA-TOKYO- 17, 183–209.

Williamson, M.D., 2009. An efficient algorithm for 3D image registration. M.Sc. thesis. Department of Computer Science. University of New Brunswick.

Yio, M.H.N., Wong, H.S., Buenfeld, N.R., n.d. 3D Pore Structure Characterisation of Blended Cement Pastes using Laser Scanning Confocal Microscopy.

Appendix B: Image noise optimization

B.1 Introduction

The number of photon counts registered by an X-ray detector is an important control on image noise. Low count numbers can lead to a significant increase in image noise this is known as the quantum mottle effect (Chapter 1). Image noise can be reduced by i) increasing photon counts at the detector and ii) averaging image frames that are collected sequentially. The following sections describe experiments that were conducted to define imaging parameters that limit noise.

B.2 Frame averaging and image noise

The following describes efforts made to address signal to noise when designing experimental parameters. Image noise was compared over a range of GSV (counts) and frame averages.

B.2.1 Methods

A piece of pure aluminum plate 9.9 mm thick was placed upright on the stage to cover the detector. It was chosen for its homogenous chemical properties and uniform thickness. X-ray radiography images where collected with an X-ray imaging system (Pinnacle X-ray Systems, Atlanta, Georgia) equipped with a Hamamatsu L12161-07 X-ray source and a Varian PaxScan®1313DX amorphous-silicon flat-panel imaging detector. All data were collected as 16-bit tiff image files. Tube voltage settings were held constant throughout experiments while tube current and frame rate were adjusted to achieve a range of GSV values. The current was adjusted to achieve a given GSV and then additional images were collected with different numbers of frame averages.

Data was processed with ImageJ (ver.1.49v). Line profiles were extracted from each of the radiograph images, and the mean and standard deviation (SD) of each of the line profiles were recorded. A relative standard deviation (RSD) was calculated for each image:

$$RSD\ \% = \frac{SD(GSV)}{Mean(GSV)} \times\ 100$$

B.2.2 Results/Discussion

The RSD can be considered a proxy for the noise so it was plotted for a range of GSV and frame averages (Fig. B.1). Images with GSV <4000 display elevated RSD due to low count numbers, and there is a general decrease in RSD with increasing numbers of frame averages. There appears to be an irreducible amount of noise (RSD = 0.22 %) that might be attributable to error of the detector. Calibration functions for RSD (%) with a different frame averages and GSV can be fitted to collected data and found in Table B.1.

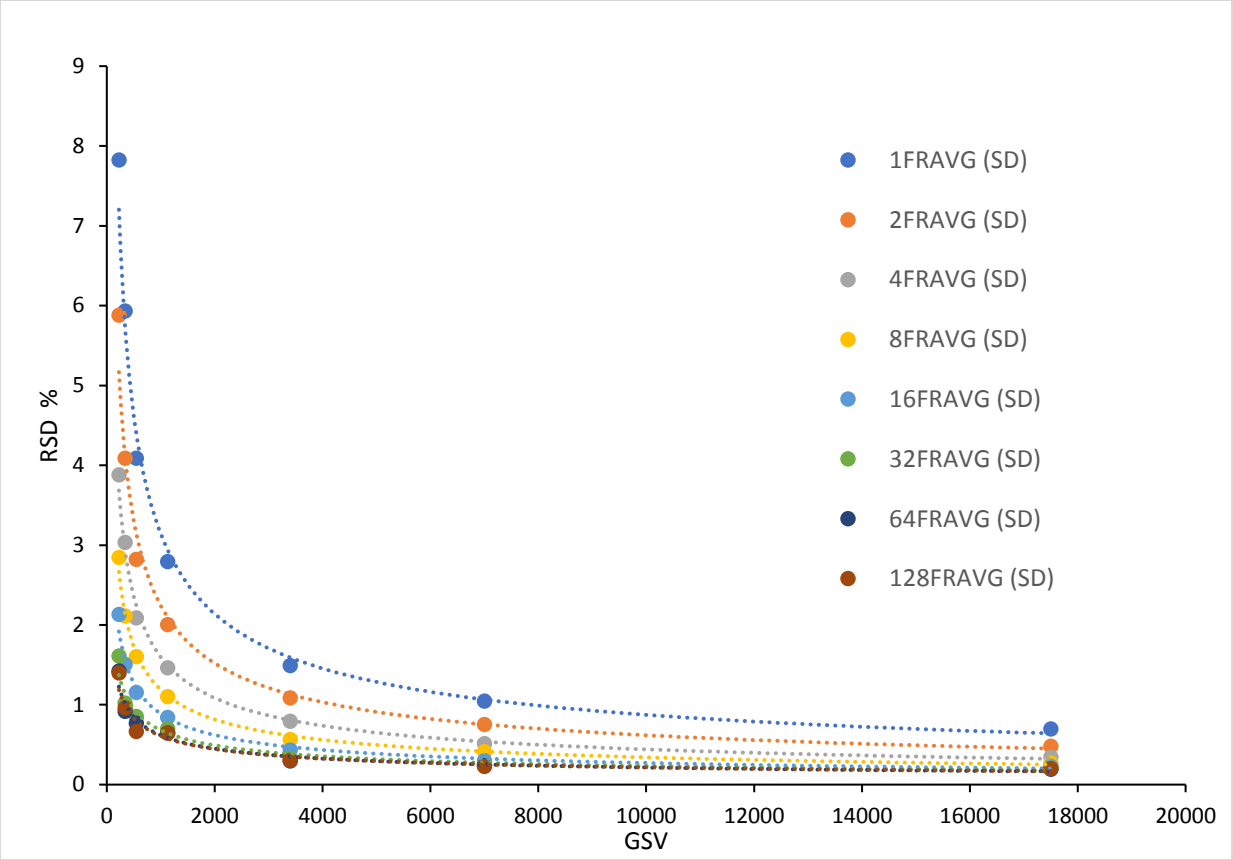

Fig. B. 1 *RSD values from averaged images versus GSVs obtained for different tube current settings. The images were collected from a homogenous aluminum plate.*

Table B. 1 *Noise calibration functions for number of frame averages.*

Number of Frame Averages	Equation	R^2
1	$y = 146.14x^{-0.556}$	0.9945
2	$y = 107.1x^{-0.56}$	0.993
4	$y = 76.181x^{-0.559}$	0.9966
8	$y = 50.1x^{-0.542}$	0.9968
16	$y = 31.482x^{-0.517}$	0.9896
32	$y = 17.447x^{-0.469}$	0.9702
64	$y = 14.852x^{-0.46}$	0.9718
128	$y = 13.547x^{-0.449}$	0.9605

B.3. Increasing Intensity (screen)

Flat-panel imaging detectors do not measure the energy of an X-ray photon, just the total number of X-ray photon counts. X-ray detectors can be oversaturated if a high photon

flux reaches the pixels at the detector, and such high fluxes, particularly at high energies, can damage the detector elements. X-ray imaging at relatively low energies requires higher photon fluxes to reach adequate intensities (GSV) at the detector (Fig. B.1). Photon paths from the source that travel through the sample result in strong attenuation, but pathways outside of the sample result in high intensities at the detector and over time this can result in damage to the detector. It is difficult to avoid this oversaturation outside of the sample because optimal signal-to-noise ratios (SNR) require high photon counts for pathways through the sample, thus the source intensity must be high. In order to allow for the use of high source intensities without risk to the detector, an X-ray blocker/screen was designed to protect areas of the detector that surround the sample. The X-ray blocker/screen was designed for both radiography and computed tomography. It can be adjusted for samples of different sizes and it is made of a material that can be used for image normalization.

B.3.1 Methods

Mycalex Ceramic (McMaster Carr) was chosen for the material of the X-ray blocker/screen based on its homogenous chemical properties (Table B.2). The design of the screen is presented in Fig. B.2. Ceramic blocks were cut with a 10 degree slope that allows for overlap to prevent gaps that would cause X-ray leakage. The screen was designed to be both attached to the stage and a separate stage mount was designed for X-ray computed tomography (Fig. B.3).

Table B. 2 *Chemical composition of Mycelex Ceramic.*

Chemical Component	[a]Mass Percentage
Boron Trioxide (B2O3)	25%
Silicon Dioxide (SiO2)	23%
Aluminum Oxide (Al2O3)	17%
Magnesium Oxide (MgO)	12%
Sodium Oxide (Na2O)	8%
Strontium Oxide (SrO)	5%
Potassium Oxide (K2O)	5%
Fluorine (F)	4%
[a]Porosity	0.00
[a]Density cm^3/g	2.77
[a]McMaster Carr	

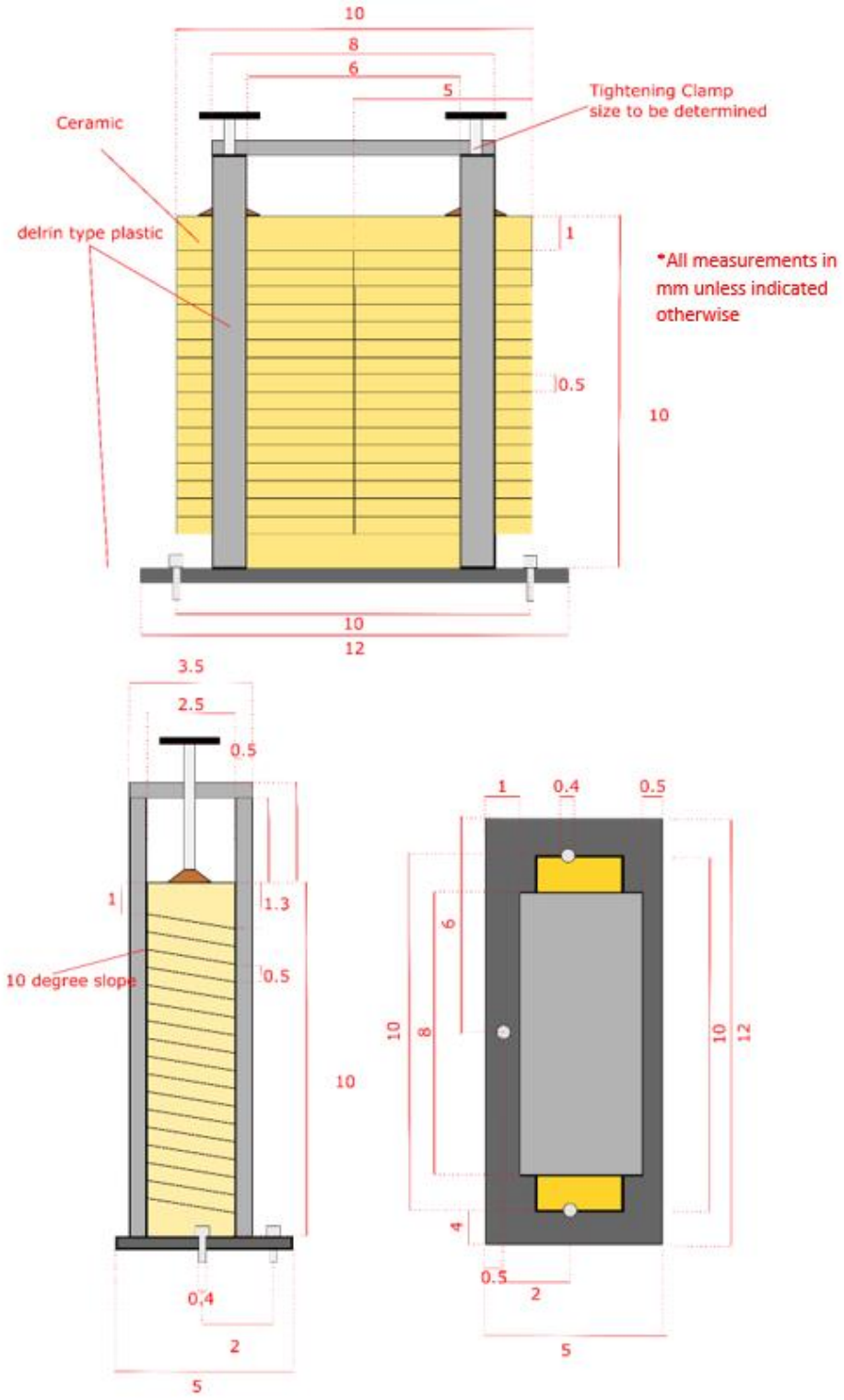

Fig. B. 2 *Schematic design of X-ray screen, Mycalex is yellow and Delrin is grey a) front-view b) side-view and c) top-view.*

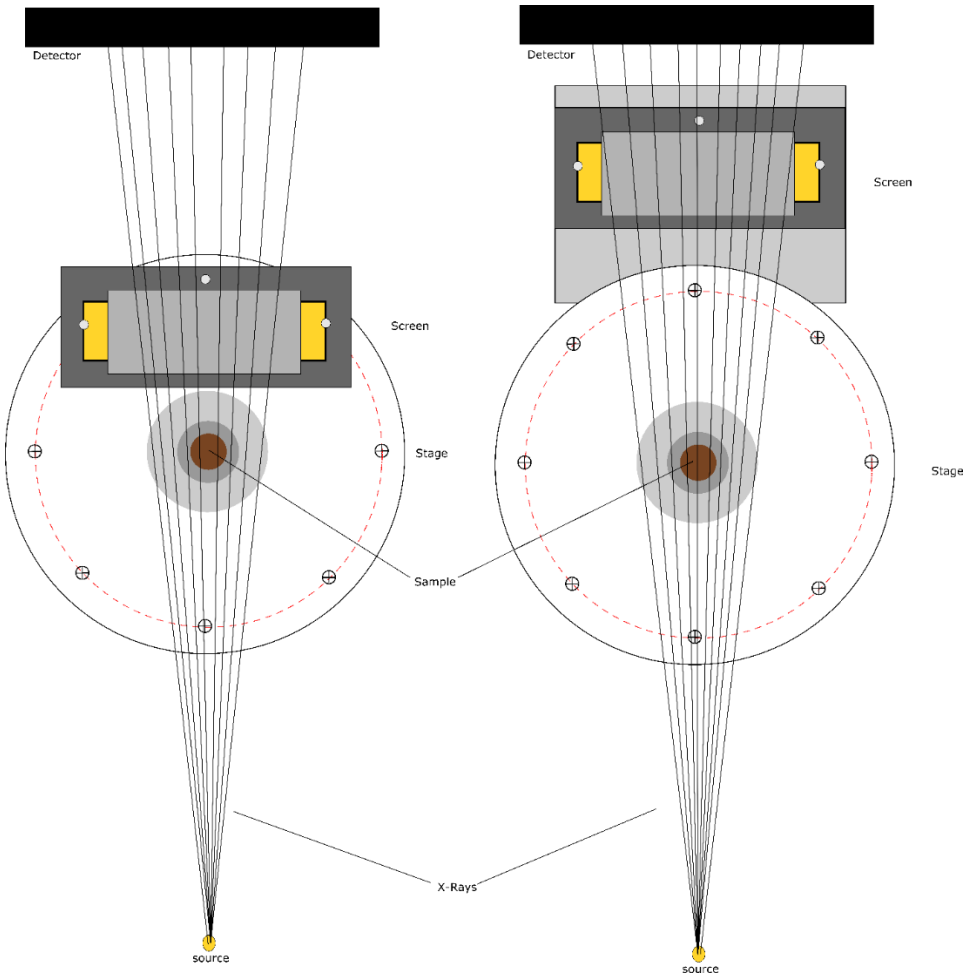

Fig. B. 3 *Top view showing mounting of screen for a) radiography where it's mounted on the stage, and b) X-ray computed tomography which uses a separate mount.*

B.3.3 Results

For both the radiographs and CT scanning, the screen effectively limits photon flux in areas outside of the sample, allowing for higher photon fluxes to be used at lower x-ray spectrum energies, thereby increasing count rates and improving SNR. At 50 kV the screen allowed for an increase of penetration over 18x (Fig. B.4).

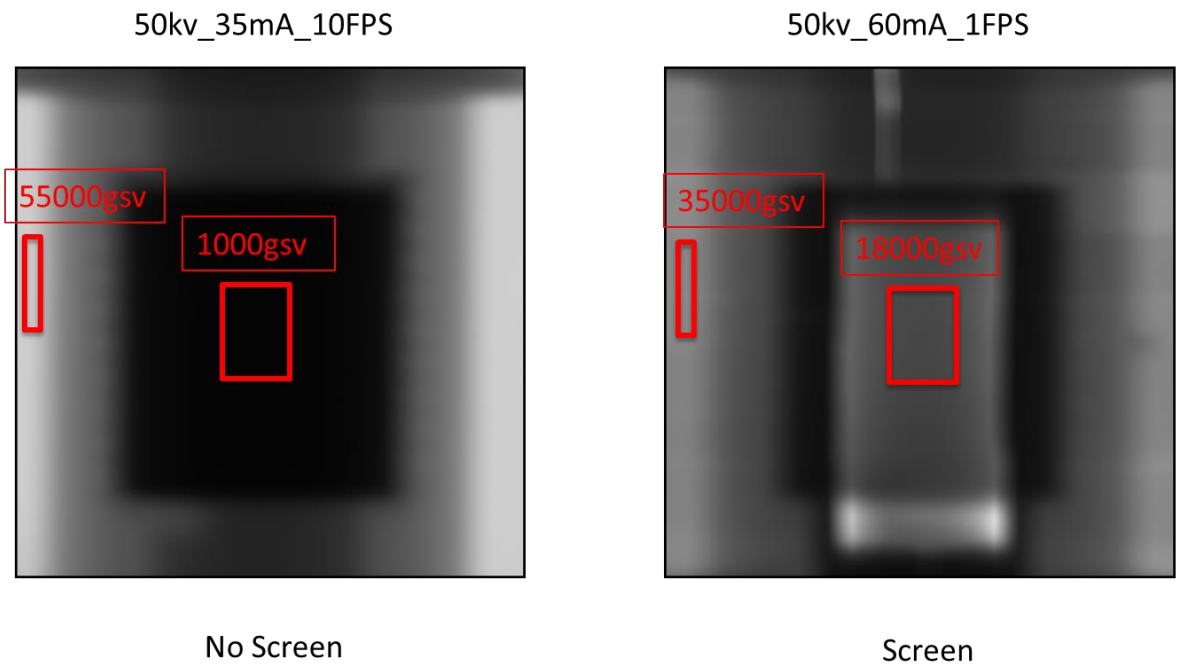

Fig. B. 4 *X-ray radiography images showing penetration achievable at 50 kV a) without screen and b) with screen.*

Appendix C: Attenuation Calculations

C.1 Introduction

As discussed in Chapter 1.3.2.6 certain imaging artifacts, such as beam hardening and image noise can be reduced with effective parameter optimization. Different imaging problems may require specific parameter optimization and quantitative image analysis requires considerable care for setup. To help determine the optimal parameters for a given imaging project, the following approach was developed for calculating attenuation in the sample and modelling the transmitted beam spectrum.

C.2 Methods

C.2.1 Attenuation

As previously discussed in Chapter 1.3.2.4 as X-rays pass through an object, they are attenuated by scattering and absorption. The basic equation for attenuation of a monoenergetic beam through a homogeneous material is Beer's Law:

$$I = I_0 exp[-\mu x] \quad [C.1]$$

Where I_0 is the incident X-ray intensity, μ is the linear attenuation coefficient of the material being scanned and x is the length of the X-ray path through the material. If the scanned object has heterogeneous material properties, the equation becomes:

$$I = I_0 exp[-\sum_i(\mu_i x_i)] \quad [C.2]$$

where increments in i represent individual materials with attenuation coefficient μ_i that are present over a linear extent x_i along the X-ray path. X-ray sources are polychromatic, emitting photons over a range of energy, and attenuation coefficients vary with X-ray energy. The

comprehensive solution requires solving Equation C.3 across the range of energies in the X-ray spectrum:

$$I = \int I_0\,(E) exp[-\sum_i (\mu_i(E) x_i)] dE \qquad [C.3]$$

The complete solution to Equation [C.3] provides the means for modelling, or simulating the X-ray radiography results, but this requires knowledge of the full photon energy spectrum for the source and an estimate of the attenuation coefficients and respective path lengths for material components present between the source and detector (Fig. C.1).

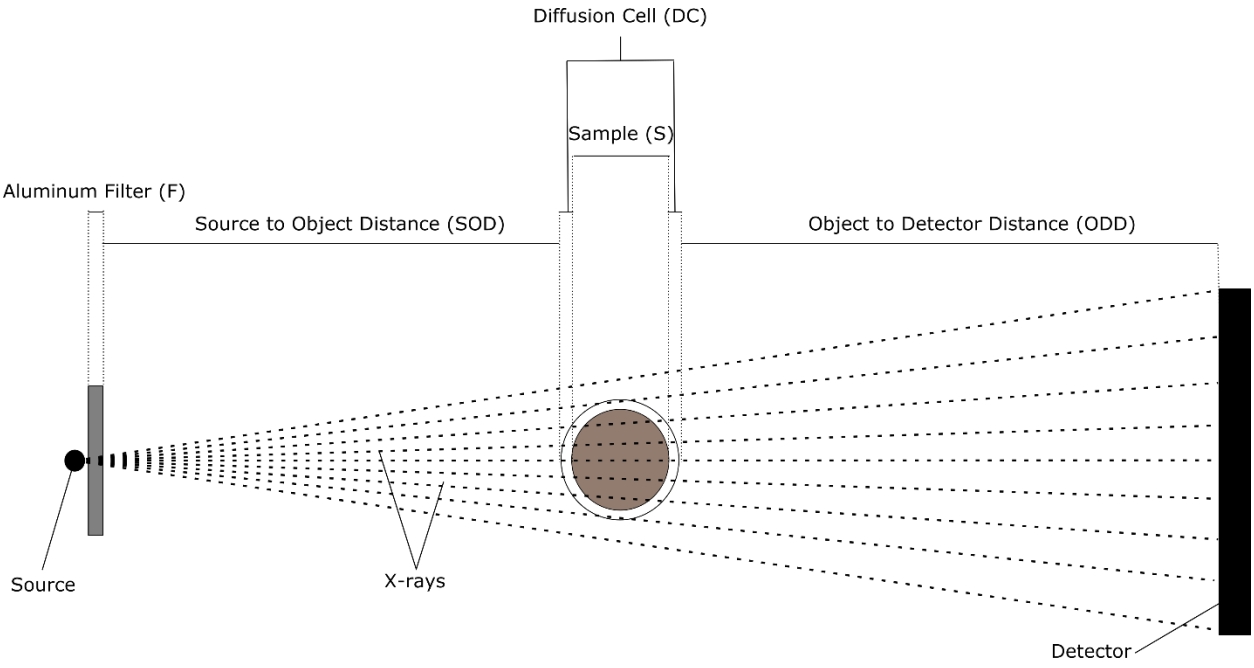

Fig. C. 1 *X-ray radiography schematic diagram, showing conceptual model of X-ray photon path length.*

The linear attenuation coefficients (μ) as a function of energy for each material component can be estimated for a variety of elements and minerals using mass attenuation coefficients (μ_m) available from the NIST XCOM database (https://physics.nist.gov/PhysRefData/Xcom/html/xcom1.html). The mass attenuation

coefficients are multiplied by the corresponding density for each material component to obtain the linear attenuation coefficients:

$$\mu(E)_i = \mu_m(E)_i * \rho_i \quad [C.4]$$

Were ρ_i is the density of a specific material component, i. The distance and linear attenuation of the material along the photon path length can be conceptualized in Figure C.1 and Table C.1 to be used in Equation C.5:

$$\sum_i \mu_i(E)x_i = \mu_F(E)x_F + \mu_{SOD}(E)x_{SOD} + \mu_{DC}(E)x_{DC} + \mu_S(E)x_S + \mu_{ODD}(E)x_{ODD} \quad [C.5]$$

To properly estimate the attenuation of the sample, the chemical (mineralogical) composition of the solids and the porewater, and their respective path lengths must be known. In a saturated sample, the product of the fractional porosity (ϕ) and the sample thickness (d) is a measure of the porewater path length. The linear attenuation coefficient of the sample becomes:

$$\mu_S(E)_{x_s} = \mu_{PW}(E)\emptyset d + \mu_M(E)(1-\emptyset)d \quad [C.6]$$

In order to solve Equations C.5 and C.6, chemical (mineralogical) compositions for the Crab Orchard Sandstone, Carbon Tan Sandstone, Berea Sandstone and the Queenston shale (Table C.2.) were used to calculate linear attenuation coefficients using the NIST XCOM database, considering only photoelectric absorption (Fig. C.2.). In addition, to complete the requirements for solving Equation C.6, the NIST XCOM database was used to determine μ_{pw} values based on porewater compositions S-SPW (Table C.2.) and Q-SPW (Table 2.2.).

Table C. 1 *Materials along X-ray radiography photon path length.*

Material	Symbol	Composition	Chemical Formula	Density (g/cm^3)
Filter	F	Aluminum	Al	2.702[a]
Source to object distance	SOD	Air	N_2 78.084% O_2 20.9476% Ar 0.934% CO_2 0.0314%	1.22e-3[b]
Diffusion Cell	DC	Delrin	CH_2O	1.41[a]
Sample -Porewater -Solid Matrix	S (pw) (M)	Table C.2 (S-SPW), Table 2.2 (Q-SPW) Table E.2 (Matrices)	–	–
Object to detector distance	ODD	Air	N_2 78.084% O_2 20.9476% Ar 0.934% CO_2 0.0314%	1.22e-3[b]

[a]McMaster Carr material property data
[b]Randell, (2010)

Table C. 2 *Mineralogy entered for initial model predictions.*

			Crab Orchard	Carbon Tan	Berea	Queenston
			Porosity[a] (ϕ_w)	Porosity[a] (ϕ_w)	Porosity[a] (ϕ_w)	Porosity (ϕ_l)
			5.4	12.8	20	5.8
				Weight %		
	Chemical formula[c]	Density (g/cm^3)[c]	Mineralogy[a]	Mineralogy[a]	Mineralogy[a]	Mineralogy[b]
Quartz	O2Si1	2.655	90	64	88	10
calcite	C1O3Ca1	2.71	0	10		20
dolomite	C2O6Mg1Ca1	2.86	0	11	2	10
K-spar	O8Al1Si3K1	2.59	2	15	5	0
albite	O8Na1Al1Si3	2.62				0
smectite (dioctohedral)	H6O25Na1Mg1Al5Si4Ca0Fe1	2.5				15
chlorite	H8O28Mg2Al6Si4Mn2Fe5	2.95				5
illite	H4O24Al6Si7K2	2.75	8		1	40
kaolinite	H8O18Al4Si4	2.645			5	
pyrite	S2Fe1	4.99				
Hematite	O3Fe2	5.254				

[a]Loomer et al., (2013)
[b]estimated based on Intera, (2011)
[c]Nesse, (2012)

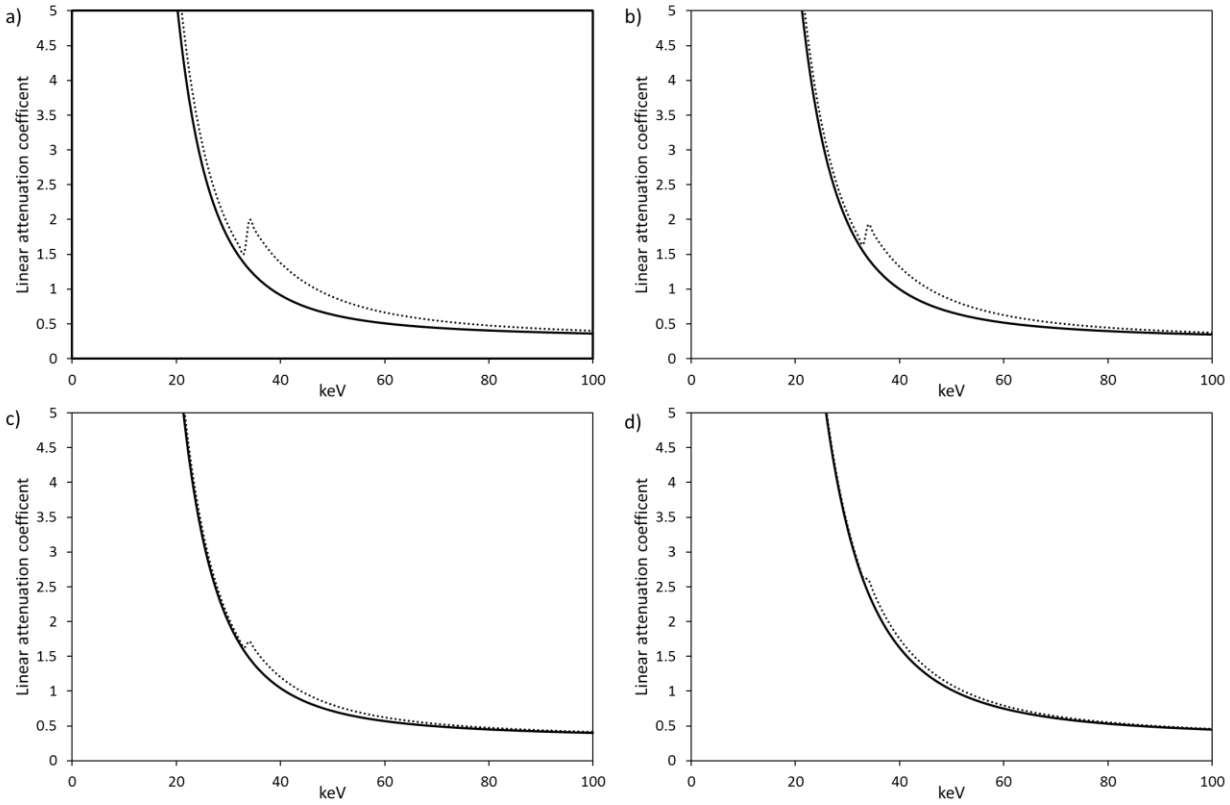

Fig. C. 2 *Plot of linear X-ray attenuation coefficients versus photon energy (keV) without tracer solution (solid) and with 1 mol/kgw I^- tracer solution (dashed) for a) Berea sandstone, b) Carbon Tan sandstone, c) Crab Orchard sandstone and d) Queenston shale.*

C.2.2 Emission spectrum

The program SPEKCALC (Poludniowski et al, 2009) solves for the relative intensities ($I(E)/\int_0^{kVp} I\,dE$) of photon energies emitted from a tungsten X-ray source. Calculated spectra for 50 kV_p (maximum tube voltage) are shown in Fig. C.3. These relative intensity emission spectra can be used to calculate $\Delta\mu$ but can not correctly estimate the actual intensity and GSV measured without a scaling factor specific to a given source and detector.

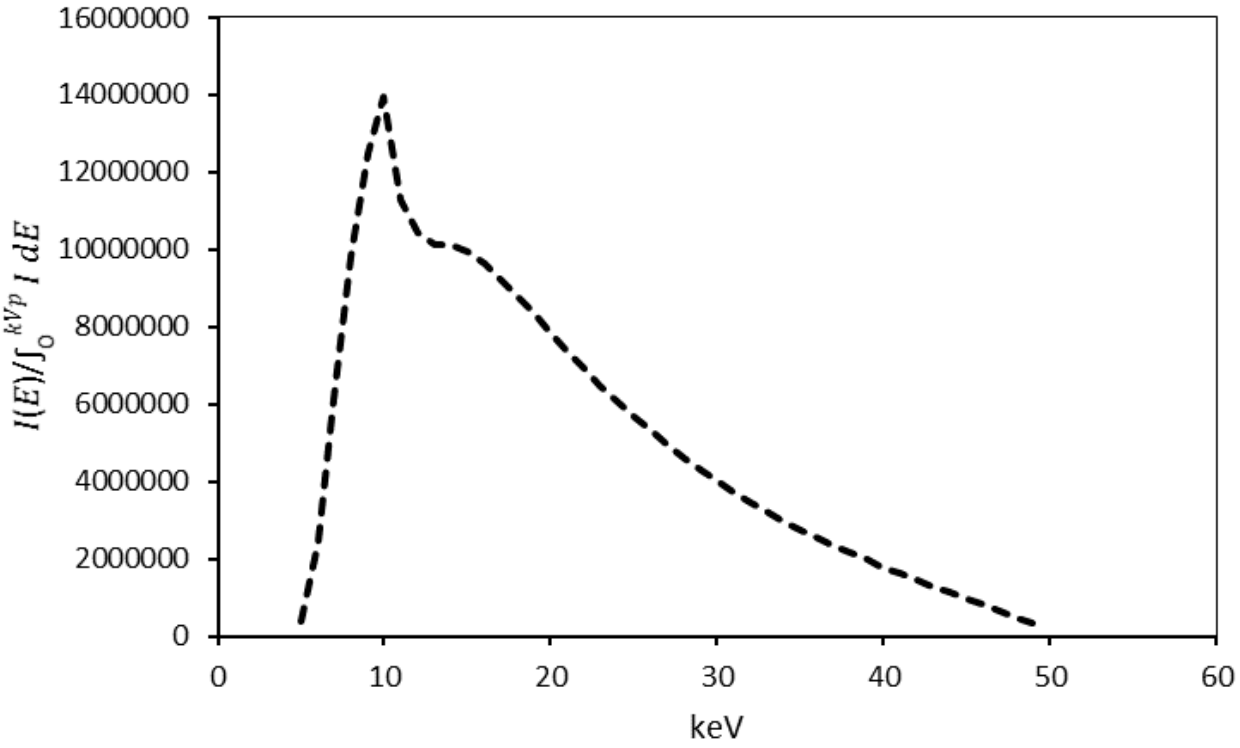

Fig. C. 3 *Calculated emission spectrum for a tungsten X-ray source with a 50 keV peak energy and 1000 mm Source-Detector Distance (SDD). Calculations were conducted with SpekCalc (Poludniowski et al, 2009).*

C.2.3 Intensity Scaling

To calibrate the relative intensity emission spectrum of the source used in radiography experiments, measurements were obtained by varying frame rate and current, and recording the intensity measured in GSVs at the detector (Fig. C.4). The measurements were used to create scaling functions to convert from relative estimations of intensity in GSV (Table C.3). Initially two separate scaling functions were created for exposure and current (Fig. C.4) (Table C.3). The scaling functions for exposure and current were combined (Table C.3) to create one function by normalizing the current function to 1.6 mA the setting used for exposure measurements (Table C.3).

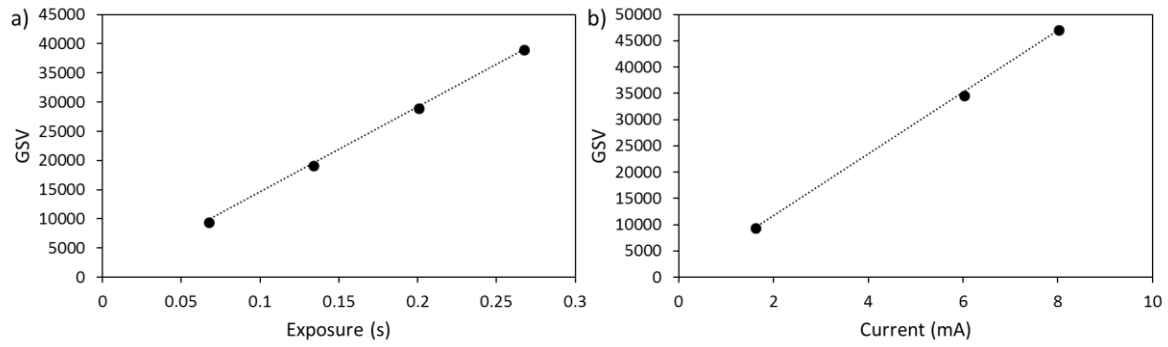

Fig. C. 4 *Intensity (GSV) at a distance of 1000 (mm) measured at the detector with varying a) exposure time (reciprocal of frame rate) at 1.6 mA current and b) current at 0.667s exposure.*

Table C. 3 *Intensity calibration functions measured at detector at 1000mm SDD.*

kV	Exposure (s)	R^2	Current (mA)	R^2	Normalized current (mA)	Calibration function
50	y=146047x	0.9998	y=5875x	0.9994	y=0.6119x	I_{cal}=[0.6119*(mA)]*[146047*(s)]

As the scaling functions are determined at a distance from the source the loss of intensity due to the attenuation in air needs to be considered. This can be done by calculating the relative intensity of the emission spectrum to the point of scaling function measurements and applying the functions to intensity spectrum at this point. Intensities can then be back calculated to represent the intensity at the source.

The intensity of an X-ray source beam can vary significantly with SDD, the inverse squares law can be used to calculate an intensity calibration function (I_f) for varying SDD measurements:

$$I_f = \frac{1}{\left(\frac{SDD}{SDD_{Cal}}\right)^2} \quad [C.7]$$

Where SDD_{Cal} is the source to detector distance at calibration in (m). The incident intensity at the source can be corrected for variable distance by:

$$I_0 = I_f I_{cal} \quad [C.8]$$

Were I_{cal} is the intensity predicted by the calibration curves at calibration distance SDD_{cal} (Table C.3).

C.3 Results/Discussion

Experimental and model results for the parameters in Table C.4 are compared in Table C.5. Modeled results (Equation C.3) overestimate the intensity values measured at the detector by 9-28% with corresponding overestimation of $\Delta\mu$ ranging from 10 to 17% (Table C.5). .

Table C. 4 *Measurement and model parameters for experiments.*

Sample	kV	mA	FPS	Al Filter thickness (cm)	Source to object (cm)	Source to Detector (cm)
Crab orchard	50	60	3	0.33	20	1000
Carbon tan	50	60	3	0.33	20	1000
Berea	50	60	3	0.33	20	1000
DGR3 472- A	50	60	1	0.33	20	1000
DGR3 472- B	50	60	1	0.33	20	1000

Table C. 5 *Compared measured and initial spectral attenuation model results.*

Sample	Crab Orchard	Carbon Tan	Berea	DGR3 472- A	DGR3 472- B
I (GSV) measured 0.00 Mol I^-	18432	18726	26761	19294	19467
I (GSV) measured 1.00 Mol I^-	14906	11682	13751	15872	15724
Measured $\Delta\mu$	0.212	0.471	0.66	0.195	0.213
I (GSV) Modeled 0.00 Mol I^-	23420	25942	31597	26146	26146
I (GSV) Modeled 1.00 Mol I^-	18581	15864	15167	21800	21801
Modeled $\Delta\mu$	0.231	0.492	0.73	0.182	0.182
% Difference *I* 0.00 Mol I^-	21	28	15	26	26
% Difference *I* 1.00 Mol I^-	20	26	9	27	28
% Difference $\Delta\mu$	8	4	10	7	17

Discrepancies between modeled and experimental data could be related to several factors including differences in the modeled and actual emission spectra emitted by the source,

the attenuating effect of Compton scattering (only the photoelectric effect was considered), the modeled versus actual porosities and errors in calibration.

The modelled spectra incident on the detector are displayed in Fig. C.5. The effects of beam hardening are evident in that the spectrum of the Queenston shale has shifted higher than the spectra for the sandstones.

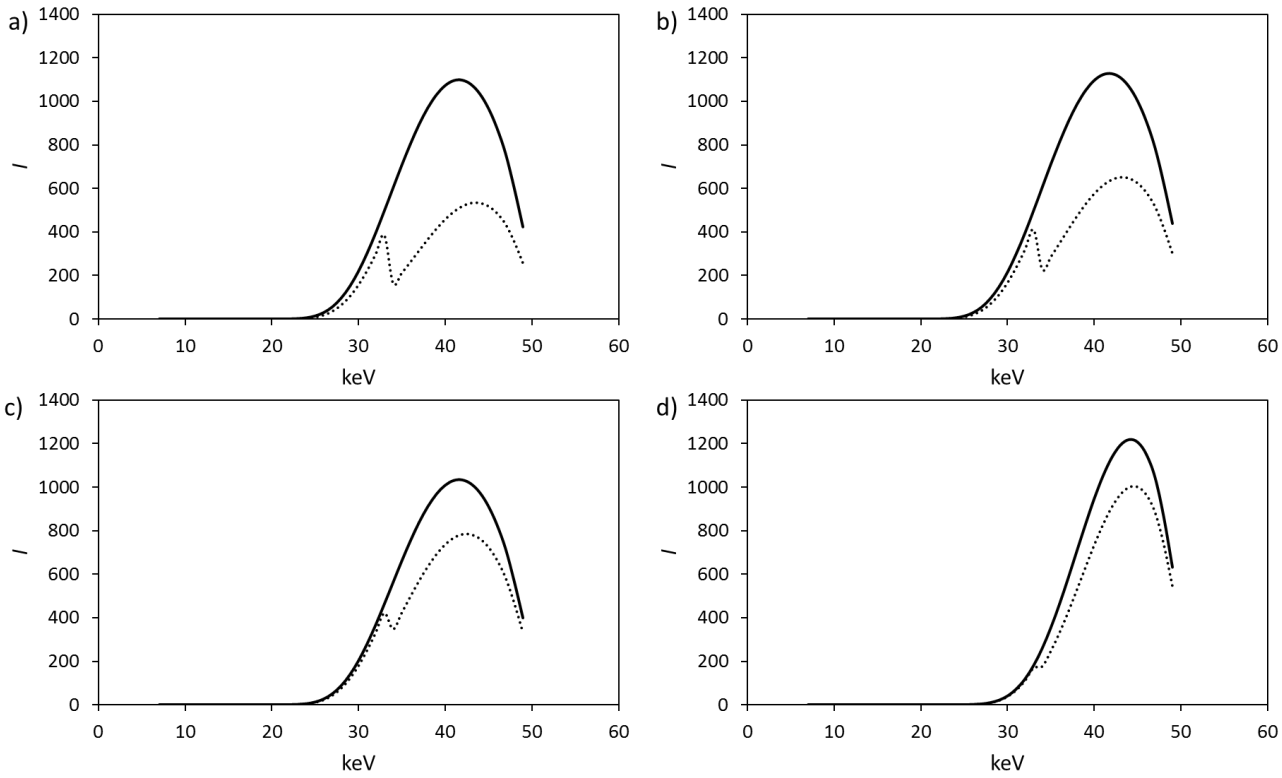

Fig. C. 5 Modelled spectra for the beam that is incident on the detector with 0.0M I^-(solid) and 1M I^-(dashed) solution at 50 k*V* 3.3 mm Al filtration for a) Berea Sandstone with S-SPW b) Carbon Tan Sandstone with S-SPW c) Crab Orchard sandstone and c) Queenston *shale with Q-SPW.*

C.4 Conclusion

This approach to modeling the attenuation of a polychromatic X-ray source is a useful approach for optimization and experimental planning that should be used to determine in advance the optimal experimental parameters for a given project.

Improvements could be made to the modeling approach by measuring and comparing the modeled emission spectrum to the actual spectrum and providing a better calibration system. It is suggested that a step wedge could be used to identify the correct emission spectrum and intensity for a given image.

C.5 References

Loomer, D., Xiang, Y., Al, T. Investigations of methods for quantifying the diffusion transport processes in sedimentary rock, NWMO-TR-2013-18. University of New Brunswick. Report prepared for the Nuclear Waste Management Organization NWMO. Report available online through http://www.nwmo.ca.

Nesse, W.D., 2012. Introduction to mineralogy.

Poludniowski, G., Landry, G., DeBlois, F., Evans, P.M., Verhaegen, F., 2009. SpekCalc: a program to calculate photon spectra from tungsten anode x-ray tubes. Phys. Med. Biol. 54, N433.

Randall, D., 2010. The Composition of Air. Carbon N. Y. 39, 1–28.

Appendix D: X-ray Radiography and Computed Tomography Data Processing

D.1 Radiograph data processing

Data processing was performed with use of the process developed of Cave et al. (2009) and modified to include a least square's fitting method (Xiang et al., 2013). Radiographs were processed by the following steps.

Step 1: Images where adjusted (registered) to correct for any stage movement between images. The position for each image was recorded and moved to match the reference image.

Step 2: following image registration, any differences in intensity of the source is accounted for by a normalization technique. A region of interest (ROI) within the ceramic screen was chosen as a "standard" and the average GSV of this ROI was measured for each image. From the measurements a normalization factor (N_f) can be calculated by:

$$N_f = \frac{\ln(gsv_{screen})_t}{\ln(gsv_{screen})_{ref}} \quad [D.1]$$

Where *t* represents a time series image and *ref* is the reference or tracer-free image. The GSVs for all pixels in the time-series image are then divided by the normalization factor.

Step 3: Identical ROIs in the samples were cropped for each of the time-series images and saved as text files (.txt). Each row of the text files was averaged creating a line profile for each radiograph. The GSVs were log transformed and multiplied by the normalization factor for each image to calculate a μ value for each point x along the profile:

$$\mu_x = \ln(gsv_x) * N_f \quad [D.2]$$

Step 4: $\Delta\mu$ was calculated by subtracting time-series μ profiles from the corresponding reference-image profile.

$$\Delta\mu_x = \mu_{x_{ref}} - \mu_{x_t} \quad [D.3]$$

.

Step 7: Two different techniques are used to determine the iodide concentration in the sample; a relative approach and a calibrated approach.

a) Relative approach: the $\Delta\mu$ profiles for time-series images are divided by the $\Delta\mu$ profile for the iodide-saturated profile creating a C/C_0 profile:

$$\left(\frac{C}{C_0}\right)_{x_t} = \frac{\Delta\mu_{x_t}}{\Delta\mu_{x_{sat}}} \quad [D.4]$$

The C/C_0 versus distance profiles can be fit to an analytical solution of Fick's second law Equation [1.4] in Chapter 1 to find D_P (we use a least square's fitting method). Data points from the first 2-3mm on each side of the sample are ignored in the fitting method due to geometric effects from the interaction of the conical beam with the end of the sample.

b) To quantify porosity and tracer concentrations in a sample, a calibrated technique is used (Cave et al., 2009). The concentrations and porosity distribution was determined directly from a multipoint calibration curve prepared from iodide standard solutions (Appendix B.3.).

D.2 Computed Tomography Data set processing

The acquired X-ray computed tomography data consist of series of 2-D 1024 x 1024 16-bit grayscale radiograph images called projections. Projection images are taken at different rotation angles over a time period and are prone to variations in intensity during a scan (Fig. D.1). To correct for variations in intensity during a scan an ImageJ macro was created to normalize projections with use of an internal standard (a fixed region of interest on the screen) (Appendix B.2). Complete X-ray CT data sets were then normalized to each other with use of Equation [D.1]. Projections were reconstructed using proprietary software (NRECON - version 1.6.x.x) from Bruker. The reconstruction yields a series of 2-D slices which were contiguously stacked together to represent the 3-D dataset.

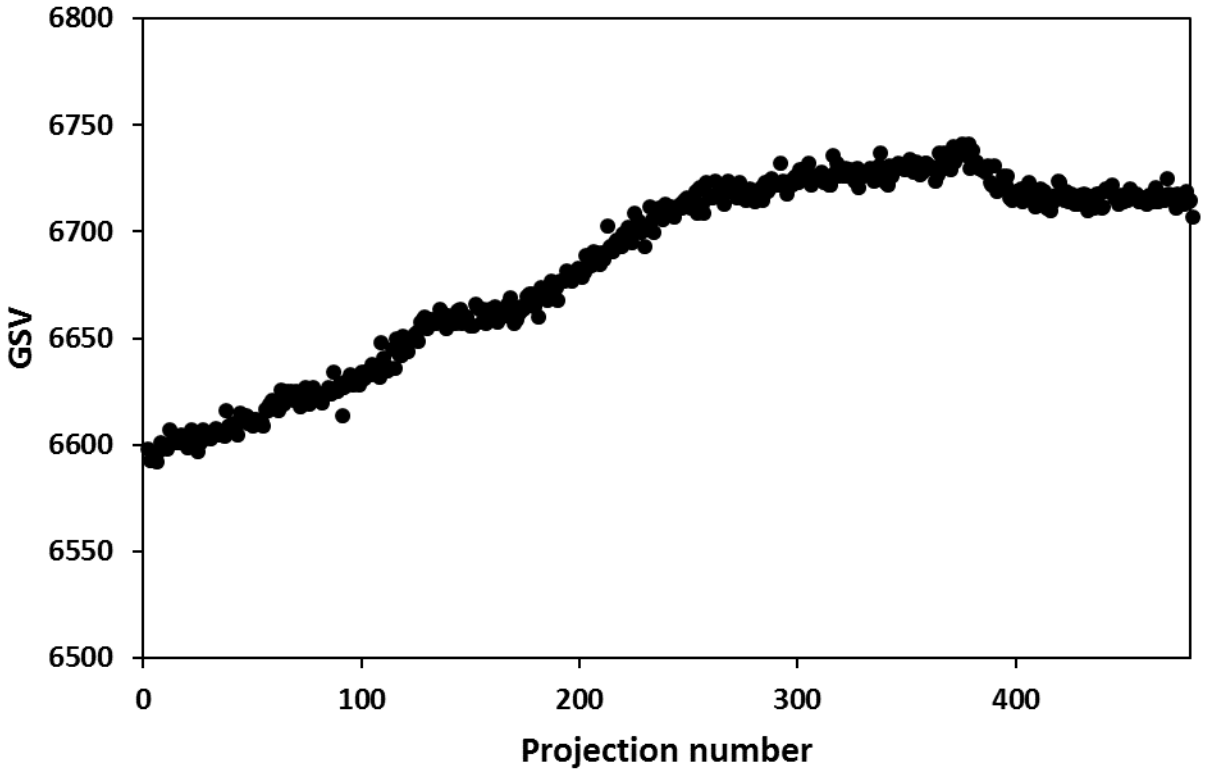

Fig. D. 1 *Variation in intensity for internal standard versus projection number (time) during an X-ray CT scan.*

Following reconstruction, the *Manual Seed Registration* code (Williamson, 2009) was employed to register the datasets in this work. This involved using the coordinate positions of the magnetite grains affixed during sample preparation as fiduciary points for digital image registration. The coordinates (x, y, and z) of these magnetite grains are manually determined for all the datasets and supplied as input into the *Manual Seed Registration* code. The code creates a region (mineral grain) around the fiduciary points based on relative grayscale values of surrounding voxels and computes the centroids of the mineral grains. The computed centroids are then used in a root mean square algorithm to re-reorient the time-series datasets to the orientation of the reference dataset using rigid body translations and rotations (Williamson, 2009).

Following registration, computed tomography data sets can be converted into spatially-resolved $\Delta\mu$ data sets by subtracting reference and tracer-saturated datasets:

$$\Delta\mu_{x,y,z} = \mu_{x,y,z_{ref}} - \mu_{x,y,z_t} \quad [D.5]$$

$\Delta\mu_{x,y,z}$ can be used for the determination of iodide-accessible porosity (ϕ_I) by the calibration approach found in Appendix D.4. Spatially resolved values for the gas-filled porosity (ϕ_{gas}) are obtained by subtracting the partially saturated $\phi_{I\text{-}pg}$ data set from the fully saturated $\phi_{I\text{-}sat}$ data set:

$$\phi_{gas} = \phi_{I-sat} - \phi_{I-pg} \quad [D.6]$$

The gas saturation (S_g) values can be calculated according to equation D.7:

$$S_g = \frac{\phi_{gas}}{\phi_{I-sat}} * 100\% \quad [D.7]$$

D.3 Radiography Calibration Curves

D.3.1 Introduction

Accurate measurement of ϕ_I with X-ray radiography depends on the ability to quantify the relationship between $\Delta\mu$ and iodide concentration along the photon path from the source to the detector. In previous work this relationship has been calibrated using glass vials filled with tracer solutions of known concentration (Cave et al., 2009a,b) or a modified approach using sandstone standards saturated with tracer solutions of known concentration (Loomer et al., 2013a,b). The glass vial calibration approach is prone to errors caused by beam hardening effects due to differences in attenuation properties between rock samples and the solutions. The sandstone approach involves calibrating with sandstone standards of known porosity and is thought to correct for beam hardening effects because of the close match between attenuation properties of the sandstone and the rock samples.

Goals of this study are to compare data between calibrations with solution-filled vials, solution-filled sandstones (Cave et al., 2009; Loomer et al., 2013), and a new modelling approach that involves calculating the photon attenuation due to transmission through a material (Appendix C).

D.3.2 Methods

D.3.2.1 Calibration with solution-filled vials

Calibration curves were conducted for Queenston Synthetic Porewater (Q-SPW; Table 2.2.) and Sandstone Synthetic Porewater (S-SPW; Table A.2.) with use of various tracer concentrations from 0-0.5 mol/kgw by substituting NaCl with NaI (Q-SPW) and KCl with KI (S-SPW). In place of the glass vials used by Cavé et al (2009a,b), the solutions were contained in an empty diffusion cell (2 cm diameter). Measurements were conducted with an X-ray CT system (Pinnacle X-ray Systems, Atlanta, Georgia) equipped with a Varian® NDI-160/22 source coupled to a Gulmay® CPL series (CP2-1402) 3000 W generator and a Varian PaxScan®1313DX amorphous-silicon flat-panel imaging detector. All data were collected as 16-bit tiff image files. $\Delta\mu$ values where calculated following the approach developed Cave et al. (2009) outlined in Appendix D.1.

D.3.2.2 Solution calibration with sandstone standards

Three sandstones were chosen as matrices based on their homogenous mineralogical and physical properties and measured porosities (water loss porosity); the Crab Orchard (5.4), Carbon Tan (12.8) and Berea (20.0) sandstones (Table C.2). Sandstone cores were prepared normal to bedding using a diamond coring bit (20-mm diameter and 20 to 23 mm length). Samples where initially flushed with CO_2 gas for 4 hours, followed by injection of S-SPW into and through the sample using a syringe. The samples where left immersed in S-SPW under vacuum for two weeks prior to the start of experiments to insure full saturation.

Samples were mounted in a diffusion cell (Fig. 2.1.) and X-ray radiography measurements were conducted with an X-ray CT system (Pinnacle X-ray Systems, Atlanta, Georgia) equipped with a Varian® NDI-160/22 source coupled to a Gulmay® CPL series (CP2-

1402) 3000 W generator and a Varian PaxScan®1313DX amorphous-silicon flat-panel imaging detector.

Initial measurements where conducted immediately after the S-SPW was replaced by S-SPW-T in both the upper and lower reservoirs (Table A.2). The samples were allowed to saturate with tracer solution by diffusion for 11 days in which reservoirs where replenished every 1-2 days, following which $\Delta\mu$ values where collected using the approach developed by Cave et al. (2009) outlined in Appendix D.1. This allowed for $\Delta\mu$ values to be assigned to the porosity of each sandstone unit. With varying waterloss porosity and $\Delta\mu$ (1 mol/kgw I^-) measured, the trend of all three sandstones can be used to create a sandstone matrix calibration function.

D.3.3 Results

D.3.3.1 Solution calibration and sandstone matrices calibration

Figures showing $\Delta\mu$ vs I^- concentration were prepared for data from solution-filled diffusion cells and the sandstone standards (Fig. D.2). At 50 kV, differences between the calibration curves generated by different methods are small compared to equivalent measurements at 60 kv (Fig. D.2). At 50 kV the calibration with sandstone is more sensitive to iodide than the calibration for the solution-filled cell, but the opposite trend is observed at 60 kV. As proposed by Loomer et al. (2013) the sandstone matrix approach likely better corrects for beam hardening effects.

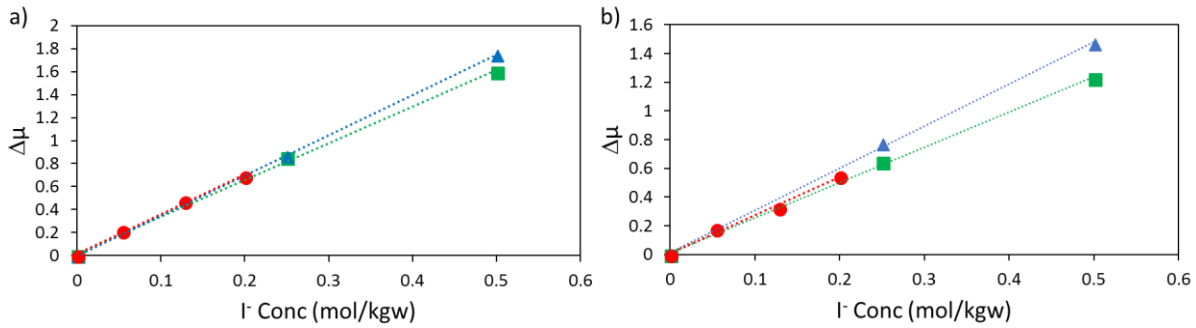

Fig. D. 2 *Measured calibration curves for Q-SPW-T (green) and S-SPW-T (Blue) in solution-filled cells, and S-SPW in a sandstone matrix (red) collected at a) 50 kV and b) 60 kV. Modelled data are indicated by the dashed lines.*

The results from these experimental measurements were compared against results from the modelling approach that is outlined in Appendix C for initial model verification. Model results were created for both the solution calibration curve and the calibration curve created using the three sandstone matrices (sandstone matrix curve). The experimental and modeled calibration curves are in good agreement with each other (Fig. D.2 and Table D.1).

Table D. 1 *Radiography calibration data.*

Calibration matrix	*50kV Equation*	*R*	*50kV (Modeled)*	*60kV Equation*	*R*	*60kV (Modeled)*
Solution-filled Cell Q-SPW-T	*Δμ=3.1907x (3.6)*	*0.999*	*Δμ=3.18x*	*Δμ=2.4545x*	*0.999*	*Δμ=2.4519x*
Solution-filled Cell S-SPW-T (Cave et al., 2009 approach)	*Δμ=3.4974x*	*0.999*	*Δμ=3.5261x*	*Δμ=2.9354x*	*0.999*	*Δμ=2.9311x*
Sandstone Matrix S-SPW-T (Loomer et al., 2013 approach)	*Δμ=3.5390x*	*0.959*	*Δμ=3.6408x*	*Δμ=2.6389x*	*0.993*	*Δμ=2.7572x*

D.3.3.2 Model Calibrated Porosity

Following good agreement between modeled and experimentally derived solution calibrations (Section D.3.3.1), individual calibration curves were calculated by the approach outlined in Appendix E for the Crab Orchard sandstone, Carbon Tan sandstone and Berea sandstone and Queenston shale with the chemical and mineralogical compositions provided in Table C.2. The porosity was varied for each of the models under the assumption that all the minerals varied equally with porosity to develop matrix specific calibration functions for samples (Table D.2). Modeled calibrations for sandstone at 50 kV display a higher sensitivity to iodide than calibrations conducted with solution-filled cells (Table D.1), but those for the Queenston shale indicate relatively low sensitivity to I^- concentration (Table D.2). The emission spectra modeled at the detector after its passed through the sample can be used to provide some insight into why the model predicts the Crab Orchard has a higher sensitivity to I^- then the S-SPW and Queenston shale (Fig. D.3). Disproportion absorption of lower energy X-rays (beam hardening) moves the peak of the emission spectrum to higher energies with higher attenuating samples, the sensitivity to iodide is highest when the spectrum is optimally centered over the K-edge of iodide (Fig. D.3.b). The model predicts that the with regard to the emission spectrum of S-SPW the large portion of X-ray energies below the K-edge range (>33keV) of iodide, leading to less sensitivity to I^- (Fig. D.3.a). On the other hand, for the Queenston shale the model predicts that many of the X-ray energies in the K-edge of Iodide are instead being by the sample, decreasing sensitivity (Fig. D.3.c).

Table D. 2 *Modeled calibration functions for various solid samples.*

Calibration matrix	*50kV Equation*	*60kV Equation*

Crab Orchard S-SPW	*Δμ=3.6393x*	*Δμ=2.7586x*
Carbon Tan S-SPW	*Δμ=3.6247x*	*Δμ=2.7469x*
Berea S-SPW	*Δμ=3.5931x*	*Δμ=2.7440x*
Queenston Q-SPW	*Δμ=2.9484x*	–

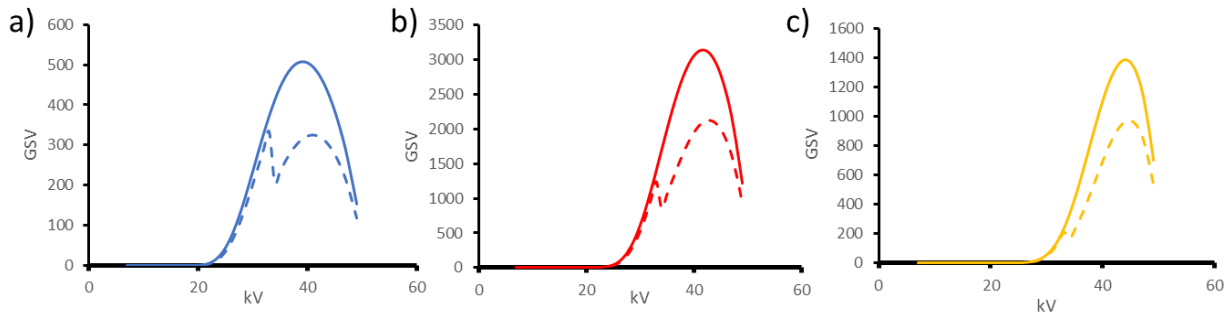

Fig. D. 3 *Modeled emission spectra generated with 0.0 mol/kgw I^- (solid) and 1 mol/kgw I^- (dashed) for the Q-SPW at 50 kV with 3.3mm Al filtration using 2 cm diameter samples a) solution-filled diffusion cell 0.1 mol/kgw I^- b) Crab Orchard sandstone 10% porosity and c) Queenston shale 10% porosity.*

D.3.4 Discussion

Porosity values calculated from the various experimental and modelled calibration functions are displayed in Table D.3. At 50 kV the differences between porosity values generated by the different techniques is minimal for the sandstone data, while the model approach results in slightly larger values for the Queenston shale (Table. D.3.). Comparisons of calculated porosity values are available for the sandstones at 60 kV and the data indicate a larger spread in predicted porosity values (Table D.3.), possibly a result of the lower sensitivity to I^- at 60 kV. At 60 kV the porosity measurements based on the solution-filled cells are consistently the lowest, those based on the model calibrations are intermediate and those based on the sandstone calibrations are highest.

Table D. 3 *Porosity measurements from various calibration functions.*

Sample	Reported by Kocurek	ϕ_w	ϕ_t from Solution-free Cell Calibration (Cave et al 2009)		ϕ_t from Sandstone Calibration (Loomer et al 2013)		ϕ_t from Model Calibration	
			50 kV	60 kV	50 kV	60 kV	50 kV	60 kV
Crab Orchard	0.066–0.087	[a]0.054 ± 0.002	0.061	0.055	0.060	0.062	0.058	0.059
Carbon Tan	0.122–0.177	[a]0.128 ± 0.002	0.135	0.121	0.133	0.136	0.131	0.130
Berea	0.190–0.200	[a]0.196 ± 0.002	0.190	0.172	0.188	0.192	0.185	0.184
DGR3-472.56-A	–	0.101–0.103	0.054	–	–	–	0.066	–
DGR3-472.56-B	–	0.101–0.103	0.059	–	–	–	0.072	–

[a]Loomer et al 2013

D.3.5 Conclusions.

When processing X-ray radiography data, the calibration procedure can significantly affect porosity results, especially at higher kV settings at which the variability of the X-ray spectrum is larger. At 50 kV all calibration produces similar results while at 60 kV the sandstone and model calibrations produce similar results because they account for beam hardening effects. The modeling is a useful alternative approach as it can be used to predict results for samples with varying chemical compositions and sample sizes without the time-consuming process of calibration experiments. Although future work in understanding differences between the actual and modelled emission spectra for the source and the validity of the modelling approach as a tool for quantification is suggested.

D.4 CT Calibration Curves

D.4.1 Introduction

As for radiography, quantification of porosity values in 3-D computed tomography data depends on knowledge of the relationship between $\Delta\mu$ and iodide concentration. The calibration approach detailed by Agbogun et al. (2013). Difference imaging removes the effects of beam hardening due to the sample matrix. However, beam hardening effects still cause spatial variations in iodide sensitivity that can significantly affect porosity distributions. A quantitative beam hardening correction function is needed to correct for spatial variations in iodide sensitivity. Agbogun et al. (2013) proposed a correction function that involves using areas expected to have 100% porosity in the sample to generate a calibration function, this approach works well in a sample that contains large pore space easily detectable in X-ray CT but not in sediments with smaller pores such as this study. Therefore, a quantitative modeling approach based on Beer Lambert's law (Appendix C) was used to generate a beam hardening correction function.

D.4.2 Methods

D.4.2.1 Calibration curves

Calibration curves were collected for Q-SPW and S-SPW using various tracer concentrations from 0 - 0.5 mol/kgw by substituting NaI for NaCl in Q-SPW, and KI for KCl in S-SPW in an empty diffusion cell (2 cm) following the approach detailed by Agbogun et al. (2013).

Computed tomography data sets were collected with an X-ray CT system (Pinnacle X-ray Systems, Atlanta, Georgia) equipped with a Hamamatsu L12161-07 X-ray source and a Varian PaxScan®1313DX amorphous-silicon flat-panel imaging detector. All data were collected as 16-bit tiff image files. Projection image sets were reconstructed with NRECON-v1.7.1.0 (Bruker

MicroCT). The reconstruction yielded series of 2-D slices which were stacked together to represent the 3-D dataset.

The calibrations and sample reconstructions were normalized to the $\Delta\mu$ predicted by the modeling approach (Appendix C) for a 1.0 mol/kgw I^- solution (2cm solution path length). Fig. D.4 presents $\Delta\mu$ vs I^- concentration for the solution-filled diffusion cell.

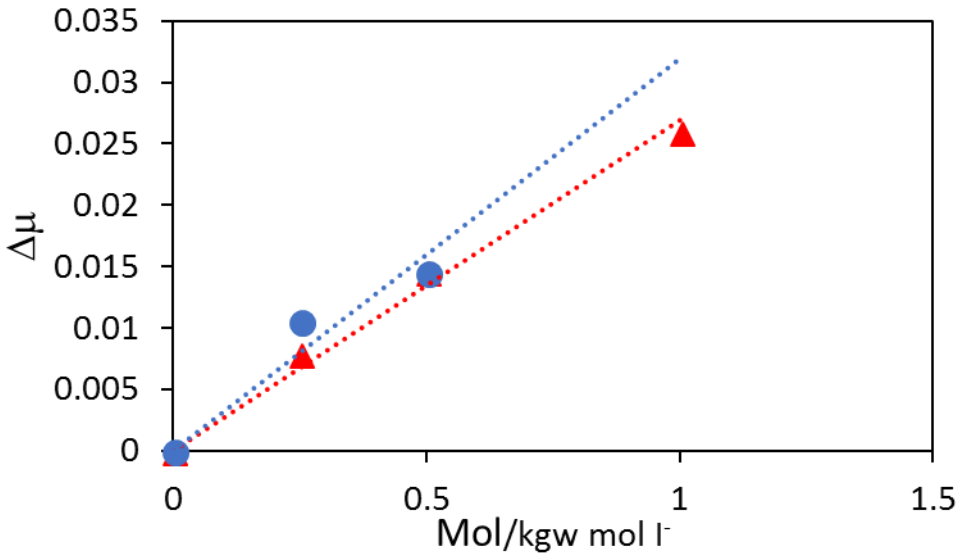

Fig. D. 4 *Calibration functions of attenuation vs iodide concentration for S-SPW-T (circles) and Q-SPW-T (triangles).*

D.4.2.2 Beam hardening correction function

3-D porosity images display significant beam hardening artifacts which affect the sensitivity and accuracy of the calibrated relationship between $\Delta\mu$ and I^- concentration. To estimate the magnitude of these effects for the Carbon Tan and Queenston shale, the sensitivity to I^- versus distance through the sample was calculated using the method outlined in Appendix C. The chemical composition for the Carbon Tan and Queenston shale used in

calculations can be found in Table C.2. The calculations were performed by varying the thickness of the sample (x_s) for solutions of 0.0 and 1.0 mol/kgw I^-.

The average $\Delta\mu$/mm with varying X-ray path length provides a quantitative analysis of the sensitivity to I^- for the Queenston shale and Carbon Tan sandstone (Fig D.5). The results can be used to consider beam hardening effects of a given sample on sensitivity of iodide with a changing X-ray path length (Fig. D.5). To properly use this approach the geometry of the sample needs to be considered and the average path length during a 3-D X-ray CT scan needs to be calculated (Fig D.6). The average path length of each point during a CT scan can be used along with the sensitivity analysis to create a beam hardening correction specific to the chemical composition of a sample.

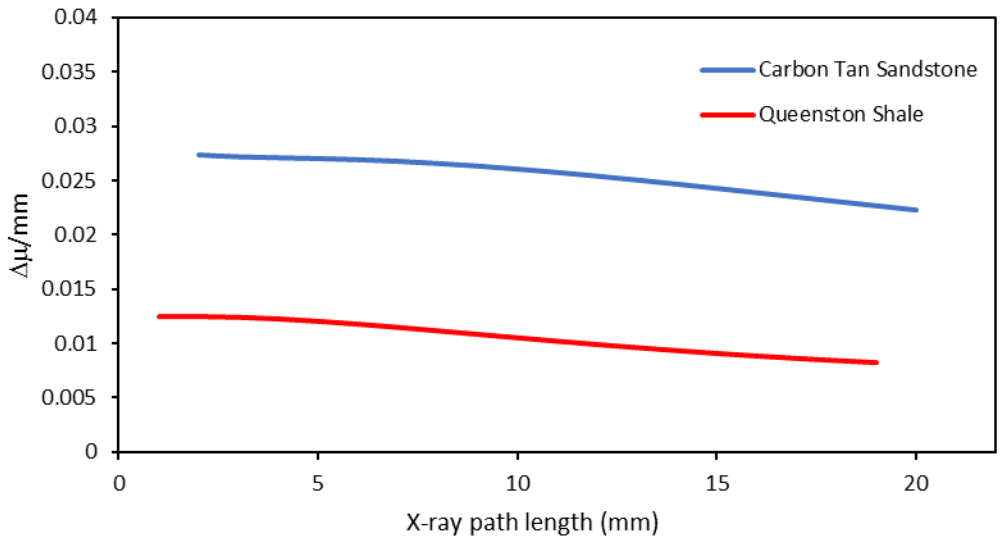

Fig. D. 5 *Calculated value $\Delta\mu$/mm with increasing X-ray path length. Demonstrating decreasing sensitivity to I^- with thicker samples.*

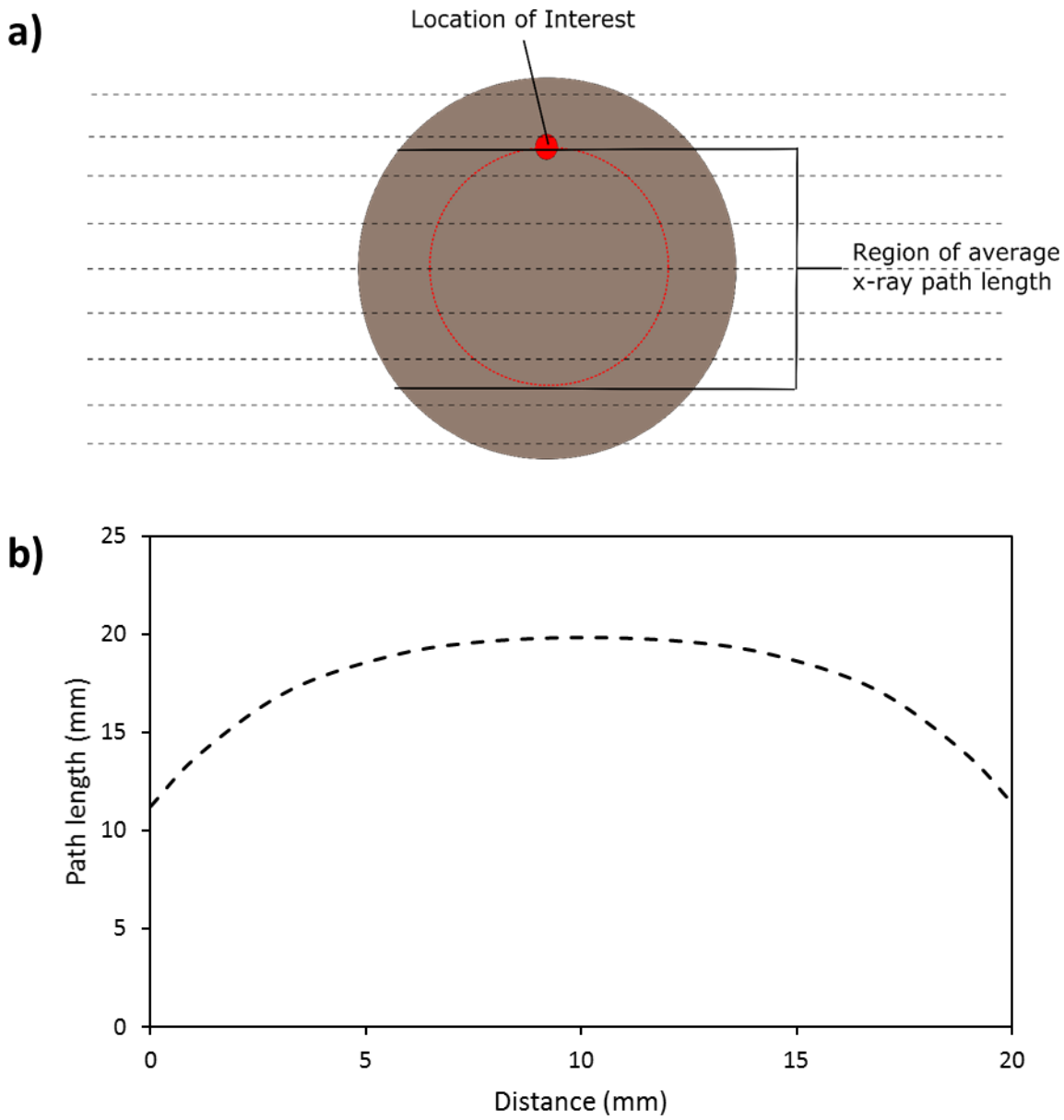

Fig. D. 6 *a) Conceptual diagram showing varying X-ray path length during a CT scan b) calculated X-ray path length across a 2cm cylindrical sample.*

D.4.3 Results

The beam hardening correction function significantly reduces the effect of variable $\Delta\mu$ response to I^- (Fig. D.7) Calibration curves derived from solution-filled cells underestimate the

porosity of the Queenston shale in 3-D computed tomography data sets while the results appear to be more accurate for sandstone samples.

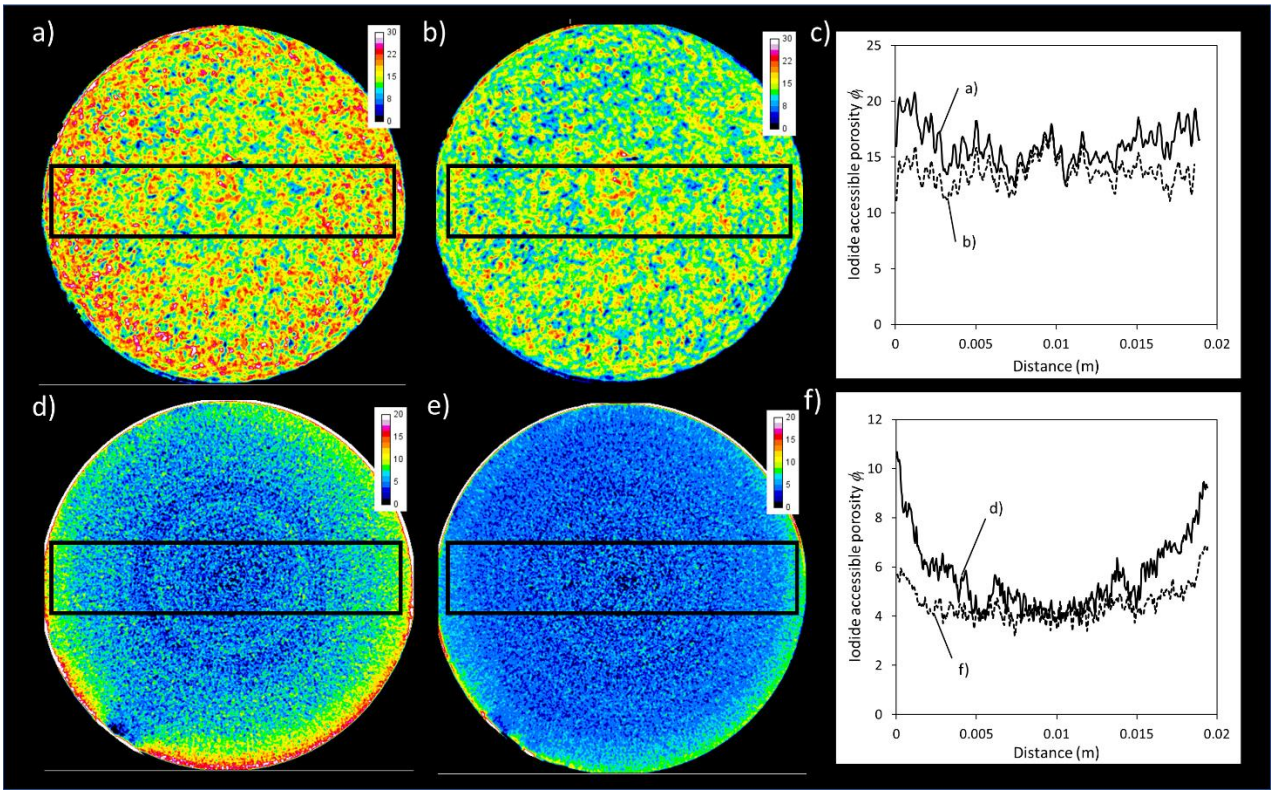

Fig. D. 7 *Slices showing effect of beam hardening on porosity measurements with and without correction. a) Carbon Tan without correction, b) Carbon Tan with correction, c) Carbon Tan cross section profiles from the rectangular region outlined in black, d) Queenston without correction, e) Queenston with correction and f) Queenston cross section profiles.*

D.4.4 Conclusions

In 3-D computed tomography, beam hardening can lead to variable sensitivity to iodide, especially with low X-ray energies and a polychromatic source. Porosity measurements based on experimental calibration curves are affected by beam hardening and, as a result, they display inaccuracy that increases with the attenuation properties of the samples. This modelling

approach indicates that beam hardening can be partially corrected by calculating the sensitivity to I^- for a specific sample as a function of distance and X-ray energy.

D.5 References

Agbogun, H.M.D., Al, T.A., Hussein, E.M.A., 2013a. Three dimensional imaging of porosity and tracer concentration distributions in a dolostone sample during diffusion experiments using X-ray micro-CT. J. Contam. Hydrol. 145, 44–53.

Agbogun, H.M.D., Hussein, E.M.A., Al, T.A., 2013b. Assessment of x-ray micro-CT measurements of porosity and solute concentration distributions during diffusion in porous geologic media. J. Porous Media 16, 683–694.

Cavé, L., Al, T., Xiang, Y., Vilks, P., 2009. A technique for estimating one-dimensional diffusion coefficients in low-permeability sedimentary rock using X-ray radiography: comparison with through-diffusion measurements. J. Contam. Hydrol. 103, 1–12.

Cavé, L., Al, T., Xiang, Y. X-ray radiography techniques for measuring diffusive properties of sedimentary rocks, NWMO-TR-2009-03. University of New Brunswick. Report prepared for the Nuclear Waste Management Organization NWMO. Report available online through http://www.nwmo.ca.

Loomer, D.B., Scott, L., Al, T.A., Mayer, K.U., Bea, S., 2013. Diffusion--reaction studies in low permeability shale using X-ray radiography with cesium. Appl. geochemistry 39, 49–58.

Loomer, D., Xiang, Y., Al, T. Investigations of methods for quantifying the diffusion transport processes in sedimentary rock, NWMO-TR-2013-18. University of New Brunswick. Report prepared for the Nuclear Waste Management Organization NWMO. Report available online through http://www.nwmo.ca.

Williamson, M.D., 2009. An efficient algorithm for 3D image registration. M.Sc. thesis. Department of Computer Science. University of New Brunswick.

Xiang, Y., Al, T., Scott, L., Loomer, D., 2013. Diffusive anisotropy in low-permeability Ordovician sedimentary rocks from the Michigan Basin in southwest Ontario. J. Contam. Hydrol. 155, 31–45.

Appendix E Image Processing Macros

E.1 CT data normalizing macro

The macro will normalize each projection to the first projection in the data set by using a ROI selected in an internal standard to account for variable intensity during a CT scan. This macro normalizes each CT projection to the first projection in the data set to account for variations in intensity during a CT scan. Initially the CT projections need to be imported into Imagej as a stack. A ROI of an internal standard needs to be selected first then run the macro. The new normalized data set can be saved by the user.

```
// Jacob Nunn  10/08/2017
// macros for normalizing CT data set to standard
//---------------------------------------------
// User selects a ROI in the background of a stack.
// This ROI is measured in each slice and the mean value of each slice is divided by first image in series to create normalization factor which is multiplied by each pixal in image
//  from the correct slice.  This corrects for variation in intensity over time.

macro "STD [F12]" {
currentTitle = getTitle();
currentID=getImageID();
run("Set Measurements...", "  mean standard redirect=None decimal=0");
selectImage(currentID);
if (nSlices>1){
// setSlice(0);
      run("Plot Z-axis Profile");    run("Close");
       for (i=1; i<=nSlices; i++){
       STDmean=getResult("Mean",(i-1));
            STDreference=getResult("Mean",(0));
            STDTotal=STDreference/STDmean;
            selectImage(currentID);
            run("Set Slice...", "slice="+i);
            run("Select All");
```

```
            run("Multiply...", "slice value="+STDTotal);}
            }
selectWindow("Results");
run("Close");
run("Set Measurements...", "  mean  redirect=None decimal=0");
run("Select None");
}
```

--end code—

Appendix F Manuscript accepted in Applied Geochemistry Journal 2018

See following page….

Investigation of partial saturation effects on diffusion in shale

Jacob A. Nunn[*,a], Yan Xiang[b] and Tom A. Al[*,a]

[a]Department of Earth and Environmental Science, University of Ottawa, 25 Templeton St., Ottawa, ON, Canada, K1N 6N5

[b]Department of Earth Sciences, University of New Brunswick, Fredericton, NB, Canada

*Corresponding authors

Abstract

A new method for testing the effect of partially saturated conditions on aqueous diffusion was developed using samples from the Upper Ordovician Queenston Formation shale from the Michigan Basin of southwest Ontario, Canada. Effective diffusion coefficients (D_e) were determined for iodide tracer on duplicate cm-scale samples from a core segment. Partially saturated conditions were created with a new gas-ingrowth method that takes advantage of the variability of N_2 solubility with pressure. The method is designed to create partially saturated pores, quantify the level of partial gas/brine saturation within the tracer-accessible pore space, and measure D_e under fully porewater-saturated and partially gas-saturated conditions for the same sample. X-ray radiography is used with an iodide tracer for quantifying the degree of partial saturation and measuring D_e. The saturated D_e values range from 2.8×10^{-12} to 3.1×10^{-12} m^2/s. Following generation of a gas phase in the pores (average gas saturations of 4 to 6.7 %), D_e values decrease by 20 to 22 % relative to the porewater-saturated condition, indicating that the tortuosity factor (ratio of constrictivity to tortuosity) is sensitive to saturation. The data suggest that a relatively small fraction of the pore space dominates the solute transport. The gas-ingrowth method was successful for generating partial gas saturation, but the distribution of the gas phase is non-uniform, with relatively high gas saturations near boundaries and lower saturations in the interior of the samples.

Keywords

diffusion; X-ray radiography; nuclear waste management; partial saturation; gas saturation; sedimentary rock; Archie's law; shale; low-permeability

1 Introduction

Low-permeability sedimentary rocks are of scientific interest because they present barriers to the migration of fluids and contaminants, which is important in CO_2 sequestration, shale gas exploitation, and nuclear waste management (Al et al., 2015; Benson and Cole, 2008; Javadpour et al., 2007; Leaung et al., 2014; Lindeberg and Bergmo, 2003; Mazurek et al., 2011; Russel and Gale, 1982). Diffusion is the dominant transport process in sedimentary formations when hydraulic conductivity (K) is less than about 10^{-10} m/s. The role of diffusive transport and its effect on barrier performance requires reliable measurements of effective diffusion coefficients (D_e) (Shackelford, 1991). Measurements of D_e have been conducted at the laboratory scale (cm) with several established techniques, including: through diffusion (Jacops et al., 2013; Rebour, 1997; Savoye et al., 2010; Van Loon et al., 2003; Xiang et al., 2016), in-diffusion (Cormenzana and Garcı, 2003), out-diffusion (Waber and Smellie, 2008), radial diffusion (Van der Kamp and Van Stempvoort, 1996; Van Loon et al., 2004), X-ray computed tomography (Agbogun et al., 2013a,b), and radiography (Cavé et al., 2009; Loomer et al., 2013; Tidwell et al., 2000; Xiang et al., 2013). Drilling and sample collection for laboratory-scale measurements may cause thermo-mechanical disruption of cores, resulting in altered physical properties such as porosity and tortuosity. Attempts have been made to reproduce in-situ temperature and pressure conditions in the laboratory in order to determine the magnitude of these effects on diffusive transport (Savoye et al., 2011; Van Loon et al., 2004; Van Loon et al., 2003; Wise and Houghton., 1966; Xiang et al., 2016). In efforts to understand diffusive transport at a larger scale (10's to 100's of m), numerous researchers have employed measurements of naturally-occurring tracer distributions in rock porewater which, combined with solute-transport modelling and knowledge of paleohydrology, allows for estimation of D_e

at the formation scale (Al et al., 2015; Bensenouci et al., 2011; Desaulniers et al., 1981; Gimmi et al., 2007; Hendry et al., 2004; Hendry et al., 2013; Hendry and Harrington, 2014; Mazurek et al., 2011; Patriarche et al., 2004a, 2004b; Remenda et al., 1994).

The majority of laboratory-scale investigations have been conducted on fully saturated samples, but under in-situ conditions, partial saturation is expected in some circumstances. Examples include organic-rich sedimentary rocks that contain $CH_{4(g)}$ at concentrations in excess of solubility, resulting in exsolution and displacement of porewater, as well as tunnelling excavations, which can lead to partially saturated conditions in the Excavation Damaged Zone (EDZ) (Matray et al., 2007; Nagra, 2008). Investigations by Savoye et al. (2010, 2012, 2014) provide the most comprehensive assessment of the effect of partial saturation on solute diffusion in clay-rich rocks. They measured D_e for various tracers in the Callovo-Oxfordian claystone under partially saturated conditions using the through diffusion method and demonstrated that partial gas saturation leads to a decrease in D_e for solutes in the aqueous phase. For iodide, the tracer which is used for the present study, they observed a decrease in the effective diffusion coefficient of Iodide (D_{e_I}) by a factor of 50 under conditions of 19% gas saturation. Additional examples of diffusion studies on partially saturated geologic materials include Badv and Faridfard (2005) Conca and Wright (1992), Hamamoto et al. (2009), Hamamoto et al. (2010), Mehta et al. (1995), Olesen et al. (2000), Porter et al. (1960) and Rowell et al. (1967).

The Upper Ordovician shales (Queenston, Georgian Bay and Blue Mountain formations) of the Michigan Basin in southwest Ontario, Canada, have been studied extensively at the Bruce nuclear site, where the 200-m thick, low-permeability shale sequence has the necessary

properties to act as natural geologic barrier for a proposed Deep Geological Repository (DGR) for low- and intermediate-level radioactive waste (CEAA, 2015).

Elevated $CH_{4(g)}$ concentrations have been measured in these shales (Clark et al., 2013), and it has been suggested that a gas phase of up to 10% may be present (Intera, 2011). The porewater in the shales has very high salinity, up to halite saturation (Al et al., 2015), and dewatering methods, such as that employed by Savoye et al. (2010, 2012, 2014), would lead to salt precipitation that could occlude pores and influence D_e. The objectives of this work were to 1) develop a novel gas-ingrowth method for generation of a gas phase by manipulating pressure to control $N_{2(g)}$ solubility; and 2) measure the degree of gas saturation in the pore space using a non-destructive X-ray radiography technique (Cavé et al., 2009); 3) quantify the change in D_e for I^- that results from the generation of partial gas saturation in samples of shale from the Michigan Basin.

2 Material and methods

2.1 Sample description

The samples used in this study are from the Ordovician Queenston Formation shale. The duplicate samples were collected from a 76-mm-diameter drill core segment at a depth of 472 m in borehole DGR-3 located at the Bruce nuclear site in southwest Ontario, Canada. Representative physical and mineralogical properties of the Queenston shale are provided in Table 1.

Table 1. *Representative physical properties of the Queenston Formation shale, including porosity, diffusivity, hydraulic conductivity and mineralogy***.**

Porosity, Diffusion and Hydraulic Conductivity

Water-accessible porosity ϕ_w[a]	Iodide-accessible porosity ϕ_I[a]	Effective-diffusion of HTO (perpendicular to bedding) $D_{e\text{-}HTO}$[a] m^2/s	Effective-Diffusion of Iodide (perpendicular to bedding) $D_{e\text{-}I}$[a] m^2/s	Hydraulic Conductivity K_h[b] m/s
0.058 – 0.11	0.044 – 0.094	4.8×10^{-12}	$1.20 \times 10^{-12} – 3.4 \times 10^{-12}$	3.0×10^{-14}

Mineralogy (wt %)

	DGR2[c]	DGR3[d]	DGR4[d]
Quartz	4.0-12.0	23.5-34.1	18.5
K-feldspar	<2	1.4-3.2	1.3
Plagioclase	<2	1.2-1.9	1.9
Calcite	8.0-57.0	6.1-14.6	31.6
Dolomite/ankerite	7.0-31.0	6.6-11.4	7.6
Clay minerals	29.0-53.0	41-45.2	36.6
Illite/mica [e]	-	58.2-60.9	60.1
Illite/smectite [e]	20-39	9.7	11.9
Chlorite [e]	9.0-14.0	29.1-39.1	24.5
Kaolinite [e]	<1	3	3.5
Pyrite	-	2.2	0.5
Hematite	-	0.12	2.1
Organic C	<0.1-0.3	-	0.13

[a] Xiang et al (2013); [b]Beauheim et al. (2014); [c] Koroleva et al. (2009); [d] Jackson et al. (2009); [e] Values are expressed as wt% of the clay fraction.

2.2 Measurement of diffusion coefficients and porosity

2.2.1 Sample preparation and apparatus

Samples for diffusion measurements were prepared in duplicate using a diamond coring bit to drill sample cores from the original 76-mm core sample. The samples (20-mm diameter and 20 to 23 mm length) were drilled normal to bedding, using air to cool the bit. Natural porewater in the Queenston shale is near saturation with respect to halite (Al et al., 2015; Clark et al., 2013) so any evaporation during sample preparation could result in halite precipitation and occlusion of the pores. In order to prevent this from affecting the porosity and diffusion measurements, a new approach was used whereby samples were initially resaturated in a

closed chamber containing an open vessel with deionized water. The water chemical potential gradient between the deionized water and the sample porewater causes water transfer to the rock porewater via the vapor phase. Resaturation is accomplished by vapor-phase diffusion, and at the point when water droplets began to accumulate on the surface of the rock, the samples were fully immersed in a synthetic pore water (SPW; Table 2) formulated for the Queenston shale using methods modified after the approach of Cavé et al. (2009) and Xiang et al. (2013). The samples were immersed in SPW under vacuum for four weeks prior to the start of experiments. Water-accessible porosity (ϕ_w) measurements were conducted on the rock material remaining after subcoring using the method described by Xiang et al. (2013). It is a gravimetric method that accounts for the porewater salinity and requires oven drying at 105 °C.

Table 2. *Composition of SPW and iodide tracer solution (SPW-T) used in diffusion experiments.*

	SPW	SPW-T
Density (kg/L)	1.22	1.32
Element	mol/kgw	mol/kgw
Na	2.61	2.61
K	0.11	0.11
Ca	1.91	1.91
Mg	0.27	0.27
Cl	7.05	6.05
Br	0.06	0.06
Sr	0.02	0.02
I	0.00	1.00

A diffusion cell (Fig. 1) was specially designed to prevent expansion of the sample under the increased pressures experienced during nucleation and expansion of a gas phase in the pores (see below). An initial confining pressure of 0.83 MPa was applied to the samples using a calibrated relationship between vertical load and torque on the threaded end caps of the

diffusion cell, similar to the approach employed by Van Loon et al. (2003). This confining pressure was intended to prevent expansion and damage to the sample during nucleation and growth of a gas phase, and it has no relationship to the confining pressure that affects the Queenston shale in natural subsurface conditions (12 MPa, Xiang et al. 2016). The cell was constructed with Delrin®, a form of polyoxymethylene thermoplastic, which was chosen for its rigidity and low X-ray attenuation and scattering properties. The silicone injection groves are created in a continuous spiral around the inner surface of the sleeve, allowing silicone to be injected in one of the ports and fill the annular space between the sample and the sleeve, forming an effective seal (Fig. 1).

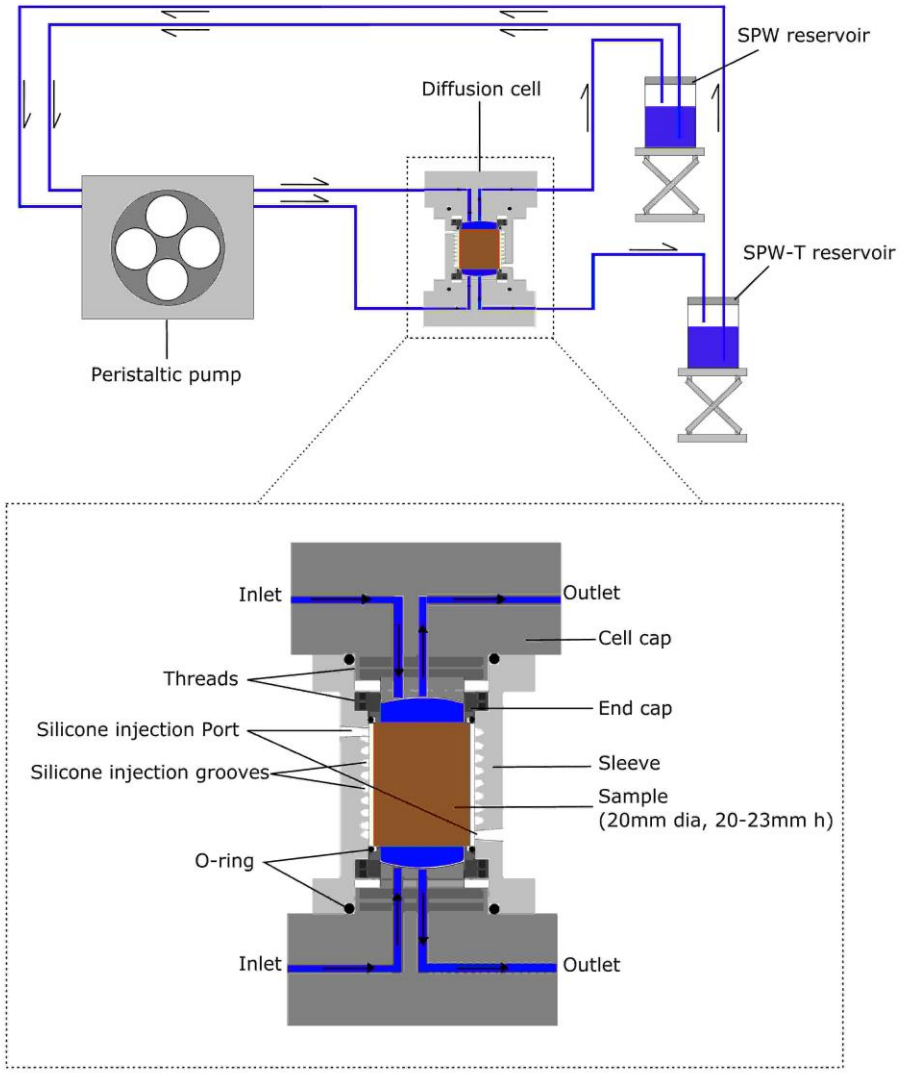

***Fig. 1**. Schematic diagram of the diffusion cell and experimental setup.*

2.2.2 Experimental procedures

Four sequential experimental procedures were performed on each of the duplicate samples (Fig. 2); first, samples were fully saturated with SPW, then in-diffusion experiments were conducted to establish diffusion coefficients for fully brine-saturated samples, the samples were then subjected to the gas generation procedure followed by measurement of the

gas-saturation profiles, and finally, out-diffusion experiments were conducted to measure diffusion coefficients with the gas phase present.

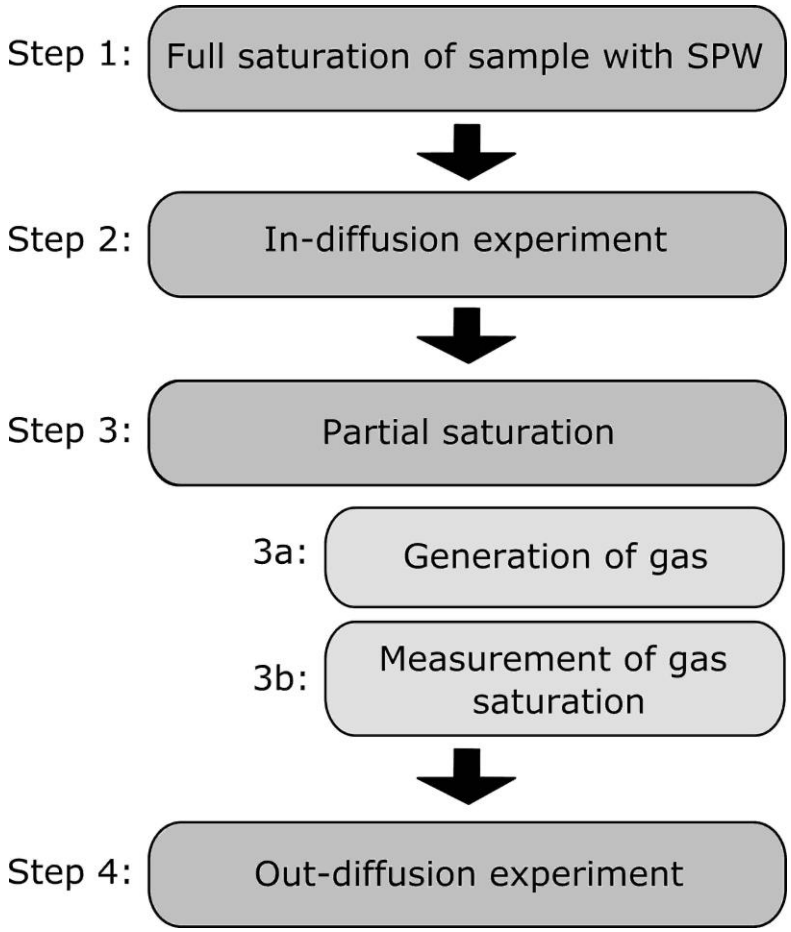

Fig. 2. *Experimental procedures undertaken for a given sample.*

Diffusion measurements were conducted using the X-ray radiography technique described by Cavé et al. (2009) based on X-ray absorption by an aqueous iodide tracer (I^-). The method can be used to spatially resolve tracer concentrations through time, allowing for determination of pore diffusion coefficients (D_p), and measurement of I^- accessible porosity (ϕ). Values of ϕ were determined for brine-saturated samples and for partially desaturated samples

($\phi_{l\text{-}g}$). A least squares regression analysis was used to obtain values for D_p by optimizing the fit between experimental data and the analytical solution to Fick's law (Crank et al., 1975):

$$C_i(x,t) = C_0 erfc \frac{x}{\sqrt[2]{D_p t}} \quad [1]$$

Were C_i is the concentration of tracer at distance x from the diffusion boundary at time (t) since the start of diffusion; C_0 is the concentration of tracer at the influx boundary, L is the maximum diffusion path length, equal to the sample thickness, and *erfc* is the complimentary error function. The following initial and bounding conditions apply (Crank, 1975; Shackelford, 1991):

$$C_{(x,t)} = 0 \Big|_{x > 0}^{t = 0}$$

$$C_{(x,t)} = C_0 \Big|_{x = 0}^{t \geq 0}$$

$$C_{(x,t)} = 0 \Big|_{x = L}^{t \geq 0}$$

Measurements were conducted with an X-ray CT system (Pinnacle X-ray Systems, Atlanta, Georgia) equipped with a Varian® NDI-160/22 source coupled to a Gulmay® CPL series (CP2-1402) 3000 W generator and a Varian PaxScan®1313DX amorphous-silicon flat-panel imaging detector. All data were collected as 16-bit tiff image files. Acquisition parameters were; 1 s exposure per frame, 32 frame averages per image, source voltage of 50 kV with 60 mA current, and source filtration with 3.3 mm aluminum. Prior to the start of diffusion experiments, the fluid reservoirs at the top and bottom of the diffusion cell (Fig. 1) were filled with SPW solution.

Experiments were initiated by replacing SPW in the lower reservoir with I^- tracer solution prepared from the SPW by substituting NaCl with NaI (Table 2). Reference images (radiographs) were collected immediately after tracer solution was injected and images were collected twice a day for the first two days, once a day for the following three days, and then the time interval increased to once every three-four days. All radiographs were collected with identical sample positioning and instrumental operating conditions. In all cases, pixel grey values from the radiograph images were converted to one-dimensional profiles that represent X-ray attenuation coefficients (μ) according to the method described by Cavé et al. (2009).

Diffusion was monitored in this way until tracer breakthrough occurred at the top boundary. The samples were then saturated with the I^- tracer solution by allowing in-diffusion from both ends. The influx of tracer was monitored by X-ray radiography over a period of eight to nine weeks until no further change in X-ray attenuation was observed. At this point, one-dimensional profiles of ϕ_I and C/C_0 were obtained following the method described by Cavé et al. (2009) and Agbogun et al. (2013). Relative concentration profiles allow for determinations of D_p by fitting experimental data to Equation 1, and when profiles are collected at different times the resulting D_p values can be averaged to find a representative value for the sample and the standard deviation provides an estimation of the variability associated with D_p. Repeat measurements were conducted on several samples to assess uncertainty in the C/C_0 profiles due to instrumental positioning and source/detector variability. The point-to-point uncertainty, expressed as a relative standard deviation (RSD), is 0.39% which translates to an uncertainty in iodide concentration of 0.004 mol/kgw.

2.3 Partial gas saturation

The fully tracer-saturated samples were subjected to partial gas generation with an approach that uses N_2 gas and takes advantage of the variability of N_2 solubility versus pressure as indicated by Henry's law (Equation 2):

$$S_i = K_{H_i} P_i \quad [2]$$

where S_i is the solubility of gas i (mol/L) in an aqueous solution; K_H is the Henry's constant ($mol \cdot L^{-1} \cdot atm^{-1}$ or M/atm); P_i is the partial pressure (atm). However, with increasing gas pressures the solubility-pressure relationship becomes non-linear and deviates from Henry's law. The solubility of N_2 in high ionic strength aqueous solutions (up to 7.7 mol/L) at 25°C can be calculated as a function of partial pressure, P_{N2}, using the model reported by Mao and Duan (2006). Calculations for the Queenston shale were conducted at the 7.7 mol/L ionic-strength limit of the model although the SPW was a Na-Ca-Cl solution with ionic strength of 9.2 mol/kgw. As a result, the N_2 solubility in SPW will be slightly overestimated by the model.

The method for generating partial saturation is based on the premise that changes in N_2 partial pressure from high (P_1) to low (P_2) causes the solubility of N_2 to decrease with the result that gas bubbles will form in the solution. For a brine solution occupying the pore spaces in a rock sample, gas bubbles should form in the pore spaces. If equilibrium is established at P_2, using the Henry's law approach, the moles of N_2 bubbles (n) can be calculated according to:

$$n_{bubble} = K_H V_p (P_1 - P_2) \quad [3]$$

where, V_p is the volume of the rock pores (L) initially occupied by brine. The volume of the gas bubbles (V_{bubble}; L) formed at P_2 can be calculated using the ideal gas law:

$$V_{bubble} = \frac{K_H V_p (P_1 - P_2) RT}{P_2} \quad [4]$$

If we assume that Henry's law and the ideal gas law are valid, the predicted volume occupied by gas (S_g) will be:

$$S_g = \left[\frac{K_H (P_1 - P_2) RT}{P_2}\right] * 100\% \quad [5]$$

As noted previously, Henry's law does not accurately represent the gas solubility at high ionic strengths and, more importantly, it is not expected that the ideal gas law, as presented in Equation 5, can accurately represent gas bubble formation in the confined pore space of clay-rich rocks. In order for gas bubbles to nucleate and grow, porewater must be expelled from the system, so the process is limited by the relative permeability for the aqueous phase, which decreases with time due to the formation of the gas phase. Also, during the time required to expel porewater, N_2 will be lost from the system by diffusion in both the aqueous phase and, increasingly, in the growing gas phase. For these reasons, it is expected that the volume of gas phase created in the pore spaces will be lower than that predicted by Equation 5. X-ray radiography was used to quantify the final degree of N_2 saturation, but the method is limited to measurements of gas saturation in the tracer-accessible pore space.

As a first step toward inducing partial gas saturation, the diffusion cells, with end caps removed, were immersed for 33 days in I^- tracer solution inside a pressure vessel with 68 atm $N_{2(g)}$ in the head space. The high N_2 gas pressure causes an increase in N_2 solubility, allowing for diffusion

of elevated aqueous N_2 concentrations throughout the pore space of the rock. Based on the D_p values determined for I^- by in-diffusion, the time period of 33 days was considered sufficient to achieve 90 – 100% of the fully-equilibrated N_2 distribution in the sample. In the second step, the $N_{2(g)}$ overpressure in the head space was decreased to 1 atm which initiates nucleation and growth of $N_{2(g)}$ bubbles in the pore spaces, forcing tracer solution out of the sample. The evolution of partial gas saturation was monitored by X-ray radiography, and five days were sufficient for equilibration of the gas and brine saturation states. After equilibration between the gas phase and the tracer-containing brine, one-dimensional profiles of μ were collected again and used to obtain 1-D profiles of the I^-- accessible porosity in the presence of the gas phase ($\phi_{I\text{-}g}$). The ratio between $\phi_{I\text{-}g}$ and ϕ_I was used to determine the fraction of gas saturation ($S_{g\text{-}I}$) in the I^--accessible pore fraction.

$$S_{g-I} = \left[1 - \left(\frac{\phi_{I-g}}{\phi_I}\right)\right] 100\% \qquad [6]$$

Anion exclusion in clay-rich rocks leads to a condition where $\phi_I < \phi_w$, so it's important to note that these reported values for $S_{g\text{-}I}$ represent fractions of ϕ_I, rather than ϕ_w. In order to represent the gas-saturation values as a fraction of ϕ_w, we multiply by the fraction of anion-accessible porosity (f_a):

$$S_{g-w} = f_a \cdot S_{g-I} \qquad \text{where: } f_a = \phi_I/\phi_w \qquad [7]$$

The use of this relationship assumes that gas-bubble nucleation and growth occurs in the largest connected pores, which are also the anion-accessible pores. This assumption is consistent with known relationships between capillary-pressure and saturation.

Out-diffusion experiments were initiated with the partially-saturated samples by introducing SPW (no tracer) into the reservoir that previously contained tracer for the in-diffusion experiments. In order to eliminate density effects, the cell was upended to maintain the higher-density solution (Table 2) at the bottom boundary. Radiographs were collected at different times using the same time increments as for the in-diffusion experiments.

3 Results and discussion

3.1 Porosity

Measurements of ϕ_w range from 0.101 to 0.103 (Table 3) and provide representative values at the sample scale, but they give no indication of smaller scale variability. Alternatively, X-ray radiography provides 1-D spatially-resolved measurements of ϕ_i (Cavé et al., 2009; Tidwell et al., 2000). These measurements indicate that there are mm-scale cyclical changes in porosity across the samples in the direction normal to bedding (Fig. 3). These features were initially thought to be due to bedding and grain-size controlled porosity variations, but petrographic examination by scanning electron microscopy (SEM) revealed that they reflect bedding-parallel dolomite-cemented lenses; the dolomite domains having lower porosity than the surrounding alumino-silicate (shale) domains (Fig. 4). There is a larger-scale variation in porosity evident in both samples, with the highest porosity (approximately 0.065 to 0.070) at the influx boundary, reaching a minima of approximately 0.055 at a distance of 0.014 m, and then increasing slightly with increasing distance (Fig. 3). Average ϕ_i values derived from the 1-D profiles for brine-saturated samples range between 0.054 and 0.059 and their standard deviations reflect the internal variability in each sample (Table 3). These measurements indicate that the fraction of anion-accessible porosity (*fa*), represented by ϕ_i/ϕ_w ranges from 0.53 to 0.58 (Table 3). This is

consistent with data reported by Xiang et al. (2013) and with previous research that indicates anion-accessible porosity in clay-rich rocks is lower than the total water-accessible porosity (Appelo et al., 2010; Bazer-Bachi et al., 2006; Descostes et al., 2008; García-Gutiérrez et al., 2006; Mazurek et al., 2015; Van Loon et al., 2003a, 2003b, 2007).

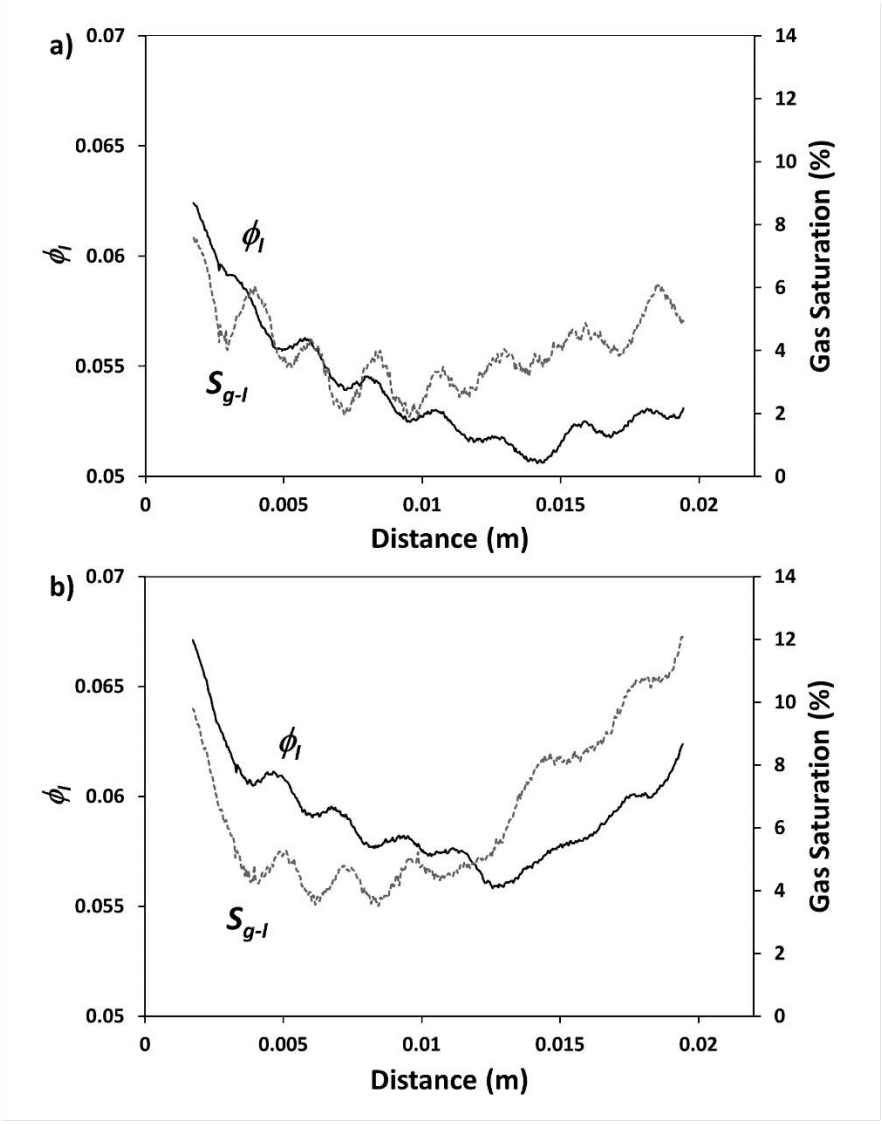

Fig. 3. *Profiles for the spatial distribution of ϕ_I and gas saturation (PG %) in samples a) DGR3-472-A, and b) DGR3-472-B. Note that PG % values are relative to the total iodide-accessible porosity. The combined geometry of the samples and the cone-shaped X-ray beam causes some minor blurring of the signal near the boundaries, resulting in loss of data over a small distance.*

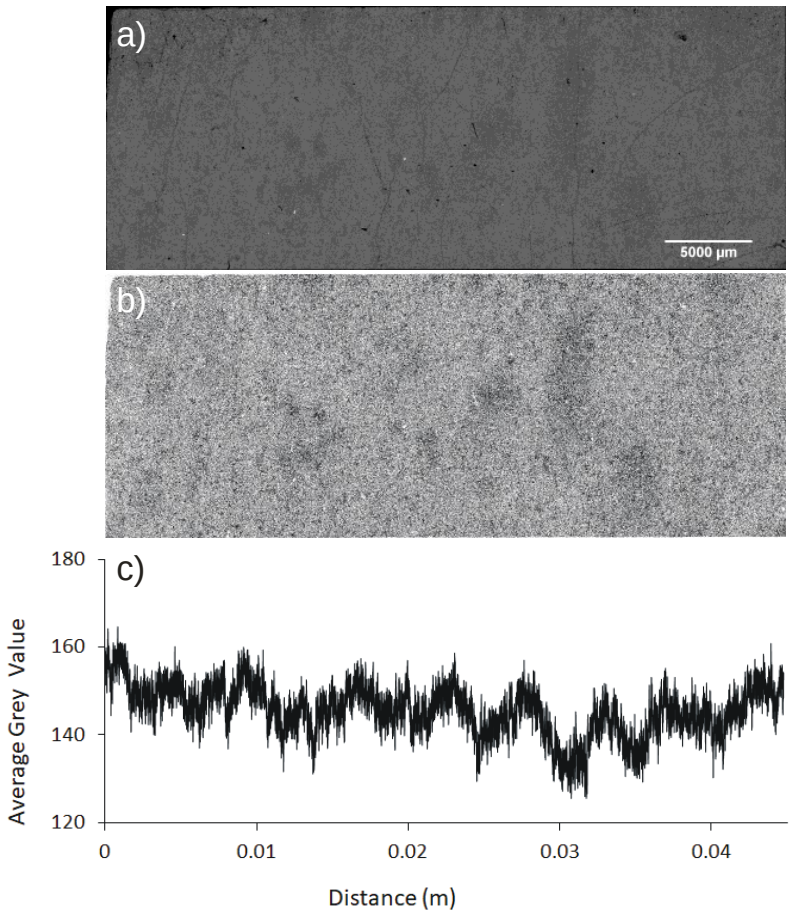

Fig. 4. *a) A back-scattered-electron image from a petrographic thin section prepared directly adjacent to the diffusion samples. The plane of the section is oriented normal to bedding. b) A binary image of the region shown in a), binarized using grey-scale thresholding to emphasize dolomite-rich regions (black). c) A profile generated from the binary image and displaying the average grey value for each column of pixels versus distance. The cyclical variability represents dolomite-cemented regions that have relatively low porosity.*

Table 3*. Comparison of results from in-diffusion measurements on fully saturated samples to out-diffusion measurements on partially saturated (PS) samples.*

Sample	DGR3 472.56-A	DGR3 472.56-A-PS	DGR3 472.56-B	DGR3 472.56-B-PS

Water accessible porosity (ϕ_w)	0.101–0.103			
Iodide accessible porosity (ϕ_I)	0.054± [0.0030]	0.052± [0.0026]	0.059± [0.0024]	0.055± [0.0024]
f_a[a]	0.53		0.58	
$S_{g\text{-}I}$ %[b]	0	4.0± [1.1]	0	6.7± [2.6]
D_p (m^2/s)	5.8×10^{-11}± 2.6×10^{-12}	4.8×10^{-11}± 1.5×10^{-12}	4.8×10^{-11}± 2.9×10^{-12}	4.2×10^{-11}± 3.1×10^{-12}
ΔD_p (%)	18.9		13.3	
D_e (m^2/s)	3.1×10^{-12}± [2.4×10^{-13}]	2.5×10^{-12}± [1.5×10^{-13}]	2.8×10^{-12}± [2.3×10^{-13}]	2.3×10^{-12}± [2.2×10^{-13}]
ΔD_e (%)	22.3		20.3	

[a] Values of f_a are calculated from ϕ_I and ϕ_w measurements on adjacent samples.

[b] Gas saturation values are relative to ϕ_I.

3.2 Diffusion in saturated shale

Profiles of relative tracer concentrations (C/C_0) collected at different times in the porewater-saturated samples are shown in Figure 5a, b. The $D_{p\text{-}I}$ values derived from fitting the experimental data to the analytical model (Equation 1) range from 4.8×10^{-11} to 5.8×10^{-11} m^2/s (Table 3). These values can be transformed to the more commonly reported effective diffusion coefficient (D_e):

$$D_e = D_p \phi_I = \frac{\delta}{\tau^2} D_0 \phi_I \quad [8]$$

where δ is the pore constrictivity, τ is the tortuosity and D_0 is the free-water diffusion coefficient. The constrictivity and the tortuosity cannot be measured independently and are often combined in one tortuosity factor τ_f:

$$\tau_f = \frac{\delta}{\tau^2} \quad [9]$$

This results in a range of D_e from 2.8 x 10^{-12} to 3.1 x 10^{-12} m^2/s which is consistent with values reported for the Queenston Formation by Xiang et al. (2013) (Table 1). By propagating the error from the averaged ϕ values, and from multiple D_p values determined from C/C_0 data, uncertainty bounds were calculated for D_e to reflect heterogeneity within a single sample. When expressed as the relative standard deviation, these are on the order of 7.7 to 8.2% (presented as 1 σ in Table 3). The variation in D_e between samples is similar (9.7%) indicating that adjacent samples have indistinguishable diffusion properties.

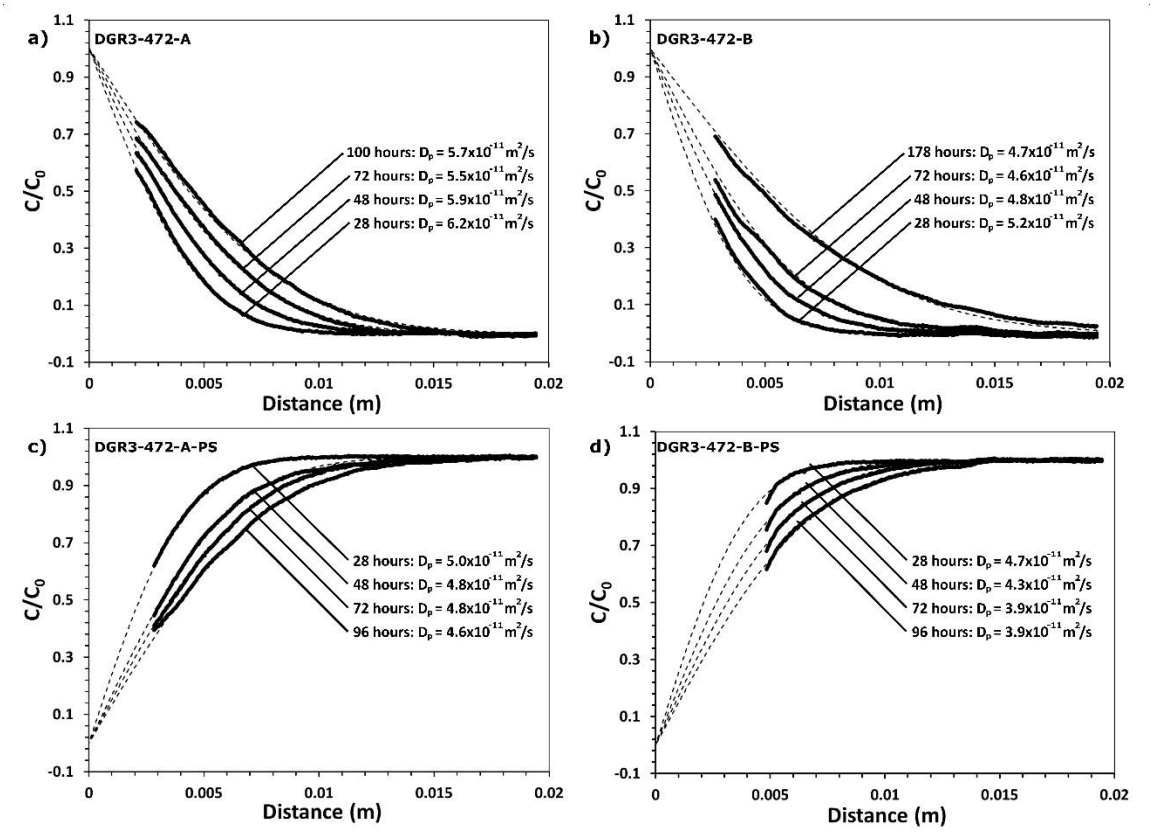

Fig. 5. *One-dimensional, profiles of relative iodide concentration (C/C_0) collected at different times: a) in-diffusion experiment with 0 % gas saturation (sample DGR-3-472.56-A), b) in-diffusion experiment with 0 % gas saturation (sample DGR-3-472.56-B) c) out-diffusion experiment with 4.0 % gas saturation (sample DGR-3-472.56-A), d) out-diffusion experiment with 6.7 % gas saturation (sample DGR-3-472.56-B). The combined geometry of the samples and the cone-shaped X-ray beam causes some minor blurring of the signal near the boundaries, resulting in loss of data over a small distance. However, the fitting procedure relies on the whole data profile and the imposed boundary condition, so the influence of this data gap near the boundary on the D_p determination should be negligible.*

3.3 Partial gas saturation

The radiographic measurements of gas saturation ($S_{g\text{-}I}$) represent the fraction of gas volume in the pore space relative to the total iodide-accessible pore volume (Equation 6). This paper is focused on iodide diffusion, so we use this approach consistently throughout.

As expected, gas saturation values are much lower than those predicted by Equation 5 which indicates values of approximately 28 % for P_1 = 68 atm. The profiles for gas saturation display cyclic variations that correlate with those observed in the profiles of ϕ (Fig. 3), with low and high points in the cycles reflecting the presence or absence, respectively, of secondary dolomite lenses (Fig. 4). The profiles are broadly U-shaped, with values at the influx and outflux boundaries ranging from 5 to 13%, and values midway along the length ranging from 2 to 5 % (Fig. 3). This observation is consistent with the expectation that gas bubbles will nucleate and grow faster near the boundaries because porewater can be expelled more rapidly due to a higher pressure gradient. The decreasing degree of gas saturation inward from the boundaries is also expected because, as the volume of gas increases near the boundaries, the relative permeability for the aqueous phase decreases (Van Genuchten, 1980), slowing the expulsion of porewater from the interior. This leads to a corresponding increase in the time available for N_2 loss by diffusion, and the rate of diffusive loss of N_2 will increase with time because the diffusion coefficient for N_2 will increase as the gas phase grows (Reardon and Moddle, 1985).

The foregoing discussion considers processes operative within a porous media with uniform porosity and pore-size distribution, but porosity in the Queenston Formation shale is not uniformly distributed (Fig. 3) and, in general, a uniform pore-size distribution is unlikely. In this case, during the initial stages of depressurization and gas exsolution, a random distribution of gas nucleation sites might be expected throughout the pore spaces (Du and Yostsos, 1999), but for nuclei to grow into bubbles, porewater must be forced out of the rock sample by advection. Consequently, gas bubbles will grow preferentially in connected regions of the rock with relatively high permeability, and when these preferential pathways are connected by a

continuous gas phase, a critical gas saturation will be reached, allowing flow of the gas phase (Firoozabadi et al., 1992). It is possible that critical gas saturation was reached near the boundaries of the samples, but almost certainly not in the interior regions of the samples.

The gas-ingrowth mechanism used for these experiments is similar to what might occur at a larger scale in a natural organic-rich shale when hydrocarbon gases build up and exceed solubility, causing partial gas saturation. It is different from the dewatering mechanism used by (Savoye et al., 2010, 2012, 2014), which may better reflect evaporative and drainage processes in wall rocks adjacent to underground excavations. Dewatering is similar to the gas-ingrowth mechanism in that it will begin with water loss in the largest pores, however with gas ingrowth, once critical gas saturation is reached, growth of the gas phase will diminish or cease (Due and Yostros., 1999). If dewatering is accomplished by outflow of water, then the limit to dewatering should be reached at the percolation threshold, but if the water is removed by evaporation, or if a chemical potential gradient is employed, as with the osmotic technique used by Savoye et al. (2010, 2012, 2014), then water loss can continue via vapour-phase transfer and result in dewatering beyond the percolation threshold. Consequently, dewatering methods can generate a higher degree of gas saturation than gas exsolution and ingrowth.

3.4 Diffusion in partially saturated shale

Profiles of relative tracer concentrations (C/C_0) collected at different times in the partially saturated samples are shown in Figure 5c,d. The consistent baseline for the profiles (baseline = 1) demonstrates that the gas-saturation profiles are stable through time. Ingrowth of 4 % gas in sample DGR3-472-A results in a decrease of D_e by 22.3 % from 3.1×10^{-12} to 2.5 x

10^{-12} m^2/s and 6.7 % gas saturation in sample DGR3-472-B causes D_e to decrease by 20.3 % from $2.8x10^{-12}$ to 2.3 x 10^{-12} m^2/s (Table 3). These data demonstrate that diffusive transport in these rocks is dominated by a small fraction of the pore space such that generation of a small amount of gas has a significant effect on diffusivity. The decrease in D_e is partially accounted for by the decrease in ϕ, but the dominant factor is a decrease in τ_f (decreased δ and/or increased τ).

Archie's 2nd law has commonly been used to describe diffusion and electrical conduction in variably saturated porous media (Archie, 1942; Hamamoto et al., 2009; Hamamoto et al., 2010; Marshall, 1959; Mualem and Friedmen, 1991; Savoye et al., 2010, 2012, 2014). According to Hamamoto et al. (2010), Archie's 2nd law can be described by Equations 10 and 11:

$$\frac{D_e}{D_0} = \phi_w^m \left[\frac{\phi}{\phi_w}\right]^n \quad [10]$$

$$\frac{D_e}{D_e^*} = \left[\frac{\phi}{\phi_w}\right]^n \quad [11]$$

where ϕ is the water-filled porosity under partially saturated conditions, D_e is the effective diffusion coefficient for iodide at a given saturation; D_e^* is the effective diffusion coefficient in the fully saturated sample, *m* is the cementation exponent and *n* is the saturation exponent. Archie's laws have been known to underestimate diffusivity and it has been suggested by many authors (Balberg et al., 1986; Hamamoto et al., 2010; Martys, 1999; Moldrup et al., 2007; Savoye et al., 2010) that there is a critical water saturation at which the water phase is no longer connected and transport through the porewater is no longer possible at a representative scale. Hamamoto et al. (2010) proposed a modified form of Archie's 2nd law to include a percolation threshold:

$$\frac{D_e}{D_0} = \left(\frac{\phi - \phi_{th}}{\phi_w - \phi_{th}}\right)^n * \left(\phi_w - \phi_{th}{}^*\right)^m \quad [12]$$

$$\frac{D_e}{D_e{}^*} = \left(\frac{\phi - \phi_{th}}{\phi_w - \phi_{th}}\right)^n \quad [13]$$

Where $\phi_{th}{}^*$ represents the fraction of the fluid phase that, under saturated conditions, does not participate in the solute-transport process, and ϕ_{th} represents the percolation threshold. In clay-rich rocks where diffusion is expected to be the dominant transport process, the assumption by Savoye et al. (2014) and Van Loon and Mibus (2015) that $\phi_{th}{}^*$ is equal to the fraction of the porewater that is inaccessible to anions is logical and seems reasonable. Furthermore, Hamamato et al. (2010) and Savoye et al. (2014) suggested it can be assumed that ϕ_{th} is equal to ϕ_{th}*.

Archie's laws are empirical relationships and there has been significant work directed at understanding the cementation exponent (*m)* in a variety of materials (Balberg, 1986; Boving and Grathwohl, 2001; Hunt, 2004; Revil and Cathles, 1999; Sen et al., 1981; Thompson et al., 1987; Van Loon and Mibus, 2015). In previous research on clay-rich rocks, *m* has been estimated to range from 2 to 3 (Descostes et al., 2008; Jacquier et al., 2013; Revil and Cathles, 1999; Savoye et al, 2010; Van Loon et al., 2003b; Van Loon and Mibus, 2015). Using Equation 12 and parameters presented in Table 3, we obtain values for *m* that fall in the same range (2.19 and 2.30 for DGR3-472-A and DGR3-472-B respectively; Table 4). There is a small number of published studies aimed toward understanding the values of the saturation exponent (*n*) for various materials. In soils and sands, values for both *m* and *n* roughly equal to 2 have been found to provide a good fit to many data sets (Archie, 1942; CRWMS M&O, 2000; Revil and

Jougnot, 2008; Hammanto et al., 2010; Thompson et al., 1987; Salem and Chilingarian, 1999). We are aware of only two studies (Savoye et al., 2010, 2014) that note values for n in clay rich rocks; they used a value of n = 2 but acknowledged that it was associated with significant uncertainty.

It is desirable to have a generalized empirical relationship such as Archie's 2nd law that could allow estimation of diffusion coefficients as a function of saturation. Based on Equation 13, this would require confidence in the determination of values for n and ϕ_{th}. As noted above, in clay-rich rocks where diffusion is the dominant transport process, it should be reasonable to assume that ϕ_{th}^* is equal to the anion inaccessible porosity, and this parameter can be measured for I^- using the X-ray radiography technique described herein and by Cavé et al. (2009). However, desaturation and anion diffusion are very different processes, so we are less confident in the assumption that $\phi_{th} = \phi_{th}^*$ as suggested by Hamamato et al. (2010) and Savoye et al. (2014). However, considering capillarity constraints on desaturation and anion-size constraints on diffusion, we expect that ϕ_{th}^* should represent the lower bound for ϕ_{th}; or $\phi_{th}^* \leq \phi_{th}$. With little known about the value of n in clay-rich rocks, it is difficult to constrain, but since n = 2 has been used in previous studies (Savoye et al., 2010, 2014), we used that value in Equation 13 to calculate ϕ_{th}. Alternatively, we used the assumptions noted above that the anion-inaccessible porosity is equal to ϕ_{th}^*, which in turn is equal to ϕ_{th}, to calculate n with Equation 13 ($\phi_{th}^* = \phi_w - fa \cdot \phi_w$). With this approach, we obtain values for n that range from 2.8 to 5.7, and values for ϕ_{th} that range from 0.059 to 0.082 (Table 4). The derived values for ϕ_{th} conform with our expectation that $\phi_{th}^* \leq \phi_{th}$, but in diffusion-dominated systems where ϕ_{th} is not known, but ϕ_{th}^*can be determined from f_a, the best approach to understand the n

exponent in Archie's 2nd law should be to assume $\phi_{th} = \phi_{th}^*$ and then calculate values for *n* with Equation 13. This method was used to generate the curves on Figure 6 where it is obvious that when the degree of water saturation is high, diffusion coefficients obtained from Equation 13 are not highly sensitive to variations in *n*. This paper is primarily intended to present a new method for diffusion measurements with partially-saturated systems and it is clear that additional data are required to further refine Archie's 2nd law for clay-rich rocks.

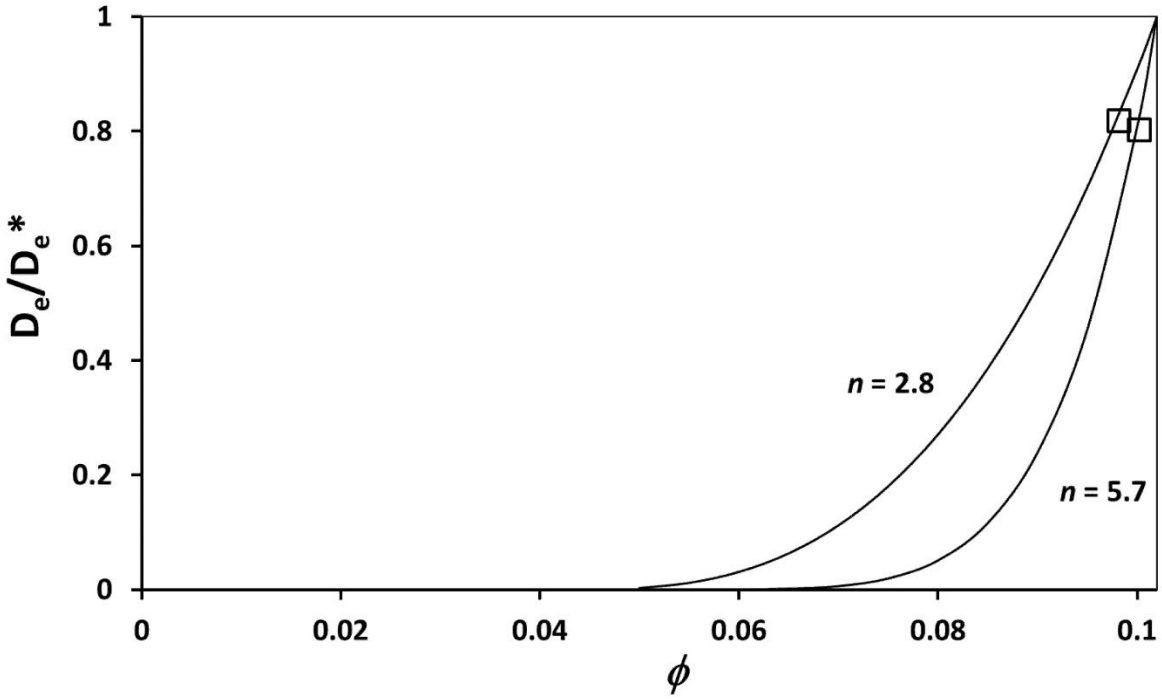

Fig. 6. *Illustration based on Equation 13 to show variation in the iodide effective diffusion coefficient as a function of the water-filled porosity. Parameters are from Table 4. The square symbols represent measurements conducted in this study.*

Table 4. *List of parameters used to estimate the range of values for n and ϕ_{th} with Equation 13.*

	Estimate Values for *n*	Estimate Values for ϕ_{th}

	DGR-3 472.56-A	DGR-3 472.56-B	DGR-3 472.56-A	DGR-3 472.56-B
Saturation exponent (*n*)	5.7	2.8	2	2
Percolation threshold (ϕ_{th})	0.048	0.043	0.082	0.059
Cementation exponent (*m*)	2.19	2.30	2.19	2.30
Inactive Fluid phase (ϕ_{th}*)	0.048	0.043	0.048	0.043
Water-accessible porosity (ϕ_w)	0.102	0.102	0.102	0.102

Conclusions

This study successfully demonstrated a method to generate partial gas saturation in low-permeability shale with hypersaline porewater. The data indicate that small-scale heterogeneity in the porosity leads to similar variations in partial gas saturation. X-ray radiography was used to measure the change in $S_{g\text{-}I}$ in the iodide-accessible pore fraction in low permeability shale. Results are consistent with the expectation that an increase in partial gas saturation causes a decrease in D_e for aqueous solutes. The results indicate that τ_f is sensitive to partial saturation. When evaluating results in terms of Archie's 2nd law, the data indicate values for the *n* exponent ranging from 2.8 to 5.7, but more data are required over a greater range of gas saturations in order to better understand the value of this empirical approach. The high salinity of the natural porewater precludes the use of dewatering techniques, and the gas-ingrowth method presented in this paper is limited by the low permeability of the rocks such that N_2 losses by diffusion are significant before bubble growth can expel pore fluid. The gas ingrowth method is therefore prone to higher degrees of gas saturation at the ends of the

sample. Future work will focus on samples with shorter length dimensions in an attempt to achieve higher, and more uniform gas distributions.

Acknowledgements

This work was supported by funding from the Nuclear Waste Management Organization (NWMO) and the Canadian Natural Science and Engineering Research Council (NSERC) (grant no. CRD 477852-14).

References

Agbogun, H.M.D., Al, T.A., Hussein, E.M.A., 2013a. Three dimensional imaging of porosity and tracer concentration distributions in a dolostone sample during diffusion experiments using X-ray micro-CT. J. Contam. Hydrol. 145, 44–53.

Agbogun, H.M.D., Hussein, E.M.A., Al, T.A., 2013b. Assessment of x-ray micro-CT measurements of porosity and solute concentration distributions during diffusion in porous geologic media. J. Porous Media 16, 683–694.

Al, T.A., Clark, I.D., Kennell, L., Jensen, M., Raven, K.G., 2015. Geochemical evolution and residence time of porewater in low-permeability rocks of the Michigan Basin, Southwest Ontario. Chem. Geol. 404, 1–17.

Appelo, C.A.J., Van Loon, L.R., Wersin, P., 2010. Multicomponent diffusion of a suite of tracers (HTO, Cl, Br, I, Na, Sr, Cs) in a single sample of Opalinus Clay. Geochim. Cosmochim. Acta 74, 1201–1219.

Archie, G.E., others, 1942. The electrical resistivity log as an aid in determining some reservoir characteristics. Trans. AIME 146, 54–62.

Badv, K., Faridfard, M.R., 2005. Laboratory determination of water retention and diffusion coefficient in unsaturated sand. Water, Air, Soil Pollut. 161, 25–38.

Balberg, I., 1986. Excluded-volume explanation of Archie's law. Phys. Rev. B 33, 3618.

Bazer-Bachi, F., Tevissen, E., Descostes, M., Grenut, B., Meier, P., Simonnot, M.-O., Sardin, M., 2006. Characterization of iodide retention on Callovo-Oxfordian argillites and its influence on iodide migration. Phys. Chem. Earth, Parts A/B/C 31, 517–522.

Beauheim, R.L., Roberts, R.M., Avis, J.D., 2014. Hydraulic testing of low-permeability Silurian and Ordovician strata, Michigan Basin, southwestern Ontario. J. Hydrol. 509, 163–178.

Bensenouci, F., Michelot, J.L., Matray, J.M., Savoye, S., Lavielle, B., Thomas, B., Dick, P., 2011. A profile of helium-4 concentration in pore-water for assessing the transport phenomena through an argillaceous formation (Tournemire, France). Phys. Chem. Earth, Parts A/B/C 36, 1521–1530.

Benson, S.M., Cole, D.R., 2008. CO 2 sequestration in deep sedimentary formations. Elements 4, 325–331.

Boving, T.B., Grathwohl, P., 2001. Tracer diffusion coefficients in sedimentary rocks: correlation to porosity and hydraulic conductivity. J. Contam. Hydrol. 53, 85–100.

Cavé, L., Al, T., Xiang, Y., Vilks, P., 2009. A technique for estimating one-dimensional diffusion coefficients in low-permeability sedimentary rock using X-ray radiography: comparison with through-diffusion measurements. J. Contam. Hydrol. 103, 1–12.

CEAA, 2015. Joint Review Panel Environmental Assessment Report: Deep Geologic Repository for Low to Intermediate Level Radioactive Waste Project. CEAA Reference No. 17520. Ottawa, Canada. Report available online through https://www.ceaa-acee.gc.ca.

Clark, I.D., Al, T., Jensen, M., Kennell, L., Mazurek, M., Mohapatra, R., Raven, K.G., 2013. Paleozoic-aged brine and authigenic helium preserved in an Ordovician shale aquiclude. Geology 41, 951–954.

Conca, J.L., Wright, J., 1992. Diffusion and flow in gravel, soil, and whole rock. Hydrogeol. J. 1, 5–24.

Cormenzana, J.L., García-Gutiérrez, M., Missana, T., Junghanns, Á., 2003. Simultaneous estimation of effective and apparent diffusion coefficients in compacted bentonite. J. Contam. Hydrol. 61, 63–72.

Crank, J., 1979. The mathematics of diffusion. Oxford university press.

CRWMS M&O, 2000. Total system performance assessment for the site recommendation, TDR-WIS-PA-000001 REV 00. Las Vegas, Nevada, United States of America.

Desaulniers, D.E., Cherry, J.A., Fritz, P., 1981. Origin, age and movement of pore water in argillaceous Quaternary deposits at four sites in southwestern Ontario. J. Hydrol. 50, 231–257.

Descostes, M., Blin, V., Bazer-Bachi, F., Meier, P., Grenut, B., Radwan, J., Schlegel, M.L., Buschaert, S., Coelho, D., Tevissen, E., 2008. Diffusion of anionic species in Callovo-Oxfordian argillites and Oxfordian limestones (Meuse/Haute--Marne, France). Appl. Geochemistry 23, 655–677.

Du, C., Yortsos, Y.C., 1999. A numerical study of the critical gas saturation in a porous medium. Transp. Porous Media 35, 205–225.

Firoozabadi, A., Ottesen, B., Mikklesen, M., others, 1992. Measurements of Supersaturation and Critical Gas Saturation (includes associated papers 27920 and 28669). SPE Form. Eval. 7, 337–344.

García-Gutiérrez, M., Cormenzana, J.L., Missana, T., Mingarro, M., Molinero, J., 2006. Overview of laboratory methods employed for obtaining diffusion coefficients in FEBEX compacted bentonite. J. Iber. Geol. 32, 37.

Gimmi, T., Waber, H.N., Gautschi, A., Rübel, A., 2007. Stable water isotopes in pore water of Jurassic argillaceous rocks as tracers for solute transport over large spatial and temporal scales. Water Resour. Res. 43.

Hamamoto, S., Perera, M.S.A., Resurreccion, A., Kawamoto, K., Hasegawa, S., Komatsu, T., Moldrup, P., 2009. The solute diffusion coefficient in variably compacted, unsaturated volcanic ash soils. Vadose Zo. J. 8, 942–952.

Hamamoto, S., Moldrup, P., Kawamoto, K., Komatsu, T., 2010. Excluded-volume expansion of Archie's law for gas and solute diffusivities and electrical and thermal conductivities in variably saturated porous media. Water Resour. Res. 46.

Hendry, M.J., Barbour, S.L., Novakowski, K., Wassenaar, L.I., 2013. Paleohydrogeology of the Cretaceous sediments of the Williston Basin using stable isotopes of water. Water Resour. Res. 49, 4580–4592.

Hendry, M.J., Harrington, G.A., 2014. Comparing vertical profiles of natural tracers in the Williston Basin to estimate the onset of deep aquifer activation. Water Resour. Res. 50, 6496–6506.

Hendry, M.J., Kelln, C.J., Wassenaar, L.I., Shaw, J., 2004. Characterizing the hydrogeology of a complex clay-rich aquitard system using detailed vertical profiles of the stable isotopes of water. J. Hydrol. 293, 47–56.

Hunt, A.G., 2004. Continuum percolation theory and Archie's law. Geophys. Res. Lett. 31.

Intera, 2011. Descriptive geosphere site model, Revision 0. DGR-TR-2011-24. Intera Engineering Ltd. Report prepared for the Nuclear Waste Management Organization NWMO. Report available online through http://www.nwmo.ca.

Jackson, R., 2009. Organic Geochemistry and Clay Mineralogy of DGR-3 and DGR-4 Core, Revision 0. TR-08-29. Report prepared for Intera Engineering Ltd., November, 2009. Report available online through http://www.nwmo.ca.

Jacops, E., Volckaert, G., Maes, N., Weetjens, E., Govaerts, J., 2013. Determination of gas diffusion coefficients in saturated porous media: He and CH 4 diffusion in Boom Clay. Appl. Clay Sci. 83, 217–223.

Jacquier, P., Hainos, D., Robinet, J.C., Herbette, M., Grenut, B., Bouchet, A., Ferry, C., 2013. The influence of mineral variability of Callovo-Oxfordian clay rocks on radionuclide transfer properties. Appl. Clay Sci. 83, 129–136.

Javadpour, F., Fisher, D., Unsworth, M., others, 2007. Nanoscale gas flow in shale gas sediments. J. Can. Pet. Technol. 46.

Koroleva, M., de Haller, A., Mader, U., Waber, H.N., Mazurek, M., 2009. Borehole DGR-2: Pore-Water Investigations, Revision 0. TR-08-06. Report prepared for Intera Engineering Ltd. (now Geofirma Engineering Ltd.), August, 2009. Report available online through http://www.nwmo.ca.

Leung, D.Y.C., Caramanna, G., Maroto-Valer, M.M., 2014. An overview of current status of carbon dioxide capture and storage technologies. Renew. Sustain. Energy Rev. 39, 426–443.

Lindeberg, E., Bergmo, P., 2003. The long-term fate of CO2 injected into an aquifer. Greenh. gas Control Technol. 1, 489–494.

Loomer, D.B., Scott, L., Al, T.A., Mayer, K.U., Bea, S., 2013. Diffusion--reaction studies in low permeability shale using X-ray radiography with cesium. Appl. geochemistry 39, 49–58.

Mao, S., Duan, Z., 2006. A thermodynamic model for calculating nitrogen solubility, gas phase composition and density of the N2--H2O--NaCl system. Fluid Phase Equilib. 248, 103–114.

Marshall, D.J., Madden, T.R., 1959. Induced polarization, a study of its causes. Geophysics 24, 790–816.

Matray, J.M., Savoye, S., Cabrera, J., 2007. Desaturation and structure relationships around drifts excavated in the well-compacted Tournemire's argillite (Aveyron, France). Eng. Geol. 90, 1–16.

Mazurek, M., Alt-Epping, P., Bath, A., Gimmi, T., Waber, H.N., Buschaert, S., De Cannière, P., De Craen, M., Gautschi, A., Savoye, S., others, 2011. Natural tracer profiles across argillaceous formations. Appl. Geochemistry 26, 1035–1064.

Mazurek, M., Oyama, T., Wersin, P., Alt-Epping, P., 2015. Pore-water squeezing from indurated shales. Chem. Geol. 400, 106–121.

Mehta, B.K., Shiozawa, S., Nakano, M., 1995. Measurement of molecular diffusion of salt in unsaturated soils. Soil Sci. 159, 115–121.

Nagra, 2008. Effects of Post-disposal Gas Generation in a Repository for Low- and Intermediate-level Waste Sited in the Opalinus Clay of Northern Switzerland. Nagra Technical Report NTB 08-07. Wettingen, Switzerland. Report available online through https://www.nagra.ch.

Mualem, Y., Friedman, S.P., 1991. Theoretical prediction of electrical conductivity in saturated and unsaturated soil. Water Resour. Res. 27, 2771–2777.

Olesen, T., Moldrup, P., Yamaguchi, T., Nissen, H.H., Rolston, D.E., 2000. Modified half-cell method for measuring the solute diffusion coefficient in undisturbed, unsaturated soil. Soil Sci. 165, 835–840.

Patriarche, D., Ledoux, E., Michelot, J.-L., Simon-Coinçon, R., Savoye, S., 2004a. Diffusion as the main process for mass transport in very low water content argillites: 2. Fluid flow and mass transport modeling. Water Resour. Res. 40.

Patriarche, D., Michelot, J.-L., Ledoux, E., Savoye, S., 2004b. Diffusion as the main process for mass transport in very low water content argillites: 1. Chloride as a natural tracer for mass transport—Diffusion coefficient and concentration measurements in interstitial water. Water Resour. Res. 40.

Porter, L.K., Kemper, W.D., Jackson, R.D., Stewart, B.A., 1960. Chloride diffusion in soils as influenced by moisture content. Soil Sci. Soc. Am. J. 24, 460–463.

Reardon, E.J., Moddle, P.M., 1985. Gas diffusion coefficient measurements on uranium mill tailings: implications to cover layer design. Uranium 2, 111–131.

Rebour, V., Billiotte, J., Deveughele, M., Jambon, A., Le Guen, C., 1997. Molecular diffusion in water-saturated rocks: A new experimental method. J. Contam. Hydrol. 28, 71–93.

Remenda, V.H., Cherry, J.A., Edwards, T.W.D., 1994. Isotopic composition of old ground water from Lake Agassiz: implications for late Pleistocene climate. Science (5193). 266, 1975.

Revil, A., Cathles, L.M., 1999. Permeability of shaly sands. Water Resour. Res. 35, 651–662.

Revil, A., Jougnot, D., 2008. Diffusion of ions in unsaturated porous materials. J. Colloid Interface Sci. 319, 226–235.

Rowell, D.L., Martin, M.W., Nye, P.H., 1967. The measurement and mechanism of ion diffusion in soils III. The effect of moisture content and soil-solution concentration on the self-diffusion of ions in soils. Eur. J. Soil Sci. 18, 204–221.

Russell, D.J., Gale, J.E., 1982. Radioactive waste disposal in the sedimentary rocks of southern Ontario. Geosci. Canada 9.

Salem, H.S., Chilingarian, G. V, 1999. The cementation factor of Archie's equation for shaly sandstone reservoirs. J. Pet. Sci. Eng. 23, 83–93.

Savoye, S., Beaucaire, C., Fayette, A., Herbette, M., Coelho, D., 2012. Mobility of cesium through the callovo-oxfordian claystones under partially saturated conditions. Environ. Sci. Technol. 46, 2633–2641.

Savoye, S., Goutelard, F., Beaucaire, C., Charles, Y., Fayette, A., Herbette, M., Larabi, Y., Coelho, D., 2011. Effect of temperature on the containment properties of argillaceous rocks: The case study of Callovo--Oxfordian claystones. J. Contam. Hydrol. 125, 102–112.

Savoye, S., Imbert, C., Fayette, A., Coelho, D., 2014. Experimental study on diffusion of tritiated water and anions under variable water-saturation and clay mineral content: comparison with the Callovo-Oxfordian claystones. Geol. Soc. London, Spec. Publ. 400, 579–588.

Savoye, S., Page, J., Puente, C., Imbert, C., Coelho, D., 2010. New experimental approach for studying diffusion through an intact and unsaturated medium: a case study with Callovo-Oxfordian argillite. Environ. Sci. Technol. 44, 3698–3704.

Sen, P.N., Scala, C., Cohen, M.H., 1981. A self-similar model for sedimentary rocks with application to the dielectric constant of fused glass beads. Geophysics 46, 781–795.

Shackelford, C.D., 1991. Laboratory diffusion testing for waste disposal—A review. J. Contam. Hydrol. 7, 177–217.

Thompson, A.H., Katz, A.J., Krohn, C.E., 1987. The microgeometry and transport properties of sedimentary rock. Adv. Phys. 36, 625–694.

Tidwell, V.C., Meigs, L.C., Christian-Frear, T., Boney, C.M., 2000. Effects of spatially heterogeneous porosity on matrix diffusion as investigated by X-ray absorption imaging. J. Contam. Hydrol. 42, 285–302.

Van der Kamp, G., Van Stempvoort, D.R., Wassenaar, L.I., 1996. Using intact cores to determine isotopic composition, chemistry and effective porosities for groundwater in aquitards. Water Resour. Res 32, 1815–1822.

Van Genuchten, M.T., 1980. A closed-form equation for predicting the hydraulic conductivity of unsaturated soils. Soil Sci. Soc. Am. J. 44, 892–898.

Van Loon, L.R., Glaus, M.A., Müller, W., 2007. Anion exclusion effects in compacted bentonites: towards a better understanding of anion diffusion. Appl. Geochemistry 22, 2536–2552.

Van Loon, L.R., Mibus, J., 2015. A modified version of Archie's law to estimate effective diffusion coefficients of radionuclides in argillaceous rocks and its application in safety analysis studies. Appl. Geochemistry 59, 85–94.

Van Loon, L.R., Soler, J.M., Bradbury, M.H., 2003a. Diffusion of HTO, 36 Cl- and 125 I- in Opalinus Clay samples from Mont Terri: effect of confining pressure. J. Contam. Hydrol. 61, 73–83.

Van Loon, L.R., Soler, J.M., Jakob, A., Bradbury, M.H., 2003b. Effect of confining pressure on the diffusion of HTO, 36 Cl- and 125 I- in a layered argillaceous rock (Opalinus Clay): diffusion perpendicular to the fabric. Appl. Geochemistry 18, 1653–1662.

Van Loon, L.R., Soler, J.M., Müller, W., Bradbury, M.H., 2004. Anisotropic diffusion in layered argillaceous rocks: a case study with Opalinus Clay. Environ. Sci. Technol. 38, 5721–5728.

Waber, H.N., Smellie, J.A.T., 2008. Characterisation of pore water in crystalline rocks. Appl. Geochemistry 23, 1834–1861.

Wise, D.L., Houghton, G., 1966. The diffusion coefficients of ten slightly soluble gases in water at 10--60 C. Chem. Eng. Sci. 21, 999–1010.

Xiang, Y., Al, T., Scott, L., Loomer, D., 2013. Diffusive anisotropy in low-permeability Ordovician sedimentary rocks from the Michigan Basin in southwest Ontario. J. Contam. Hydrol. 155, 31–45.

Xiang, Y., Al, T., Mazurek, M., 2016. Effect of confining pressure on diffusion coefficients in clay-rich, low-permeability sedimentary rocks. J. Contam. Hydrol. 195, 1–10.